Thesis for the degree of Doctor of Philosophy

Tilted Foils Nuclear Spin Polarization at REX-ISOLDE

Hans T. Törnqvist

Department of Fundamental Physics
Chalmers University of Technology
Göteborg, Sweden 2013

Tilted Foils Nuclear Spin Polarization at REX-ISOLDE
Hans T. Törnqvist
ISBN 978-91-7385-860-1

Doktorsavhandlingar vid Chalmers tekniska högskola
Ny serie Nr 3541
ISSN 0346-718X

Department of Fundamental Physics
Chalmers University of Technology
SE-412 96 Göteborg
SWEDEN
Telephone: +46 (0)31-772 1000

Cover:
Top-bottom: Visualization of spin polarization transfer, the β-NMR setup used in the ^{8}Li experiment, the foil folder for the ^{21}Ne experiment, and the β-NMR signal obtained in the project.

Chalmers Reproservice
Göteborg, Sweden 2013

Tilted Foils Nuclear Spin Polarization at REX-ISOLDE

Hans T. Törnqvist
Department of Fundamental Physics
Chalmers University of Technology

Abstract

This thesis will explain and summarize my work and involvement in experiments aimed at producing nuclear spin polarization of post-accelerated beams of ions with the tilted-foils technique at the REX-ISOLDE linear accelerator at CERN. Polarizing the nuclear spin of radioactive beams in particular may provide access to observables which may be difficult to obtain otherwise. Currently, the techniques commonly employed for nuclear spin polarization are restricted to specific nuclides and experimental measurement techniques. Tilted foils polarization may provide a new tool to extend the range of nuclides that can be polarized and the types of experiments that can be performed.

The experiments rely not only on the production but also on the method to measure the degree of attained polarization. Two methods will be treated, based on particle scattering in Coulomb excitation that may be utilized for stable beams, and the β-NMR that requires β-decaying nuclei. The experimental setups and measurements will be described with interpretation of collected data and final results.

Experiments have already been proposed utilizing the setup developed for this project. Furthermore, since the tilted foils polarization technique may be a tool to produce a new range of polarized beams at the upcoming HIE-ISOLDE facility, and is most efficient with low energy beams, post-acceleration of the beam is of major interest. Reaching the intermediary energy range after post-acceleration may allow Coulomb excitation and transfer experiments to use polarized beams of exotic isotopes. The thesis will conclude with initial studies for post-acceleration at the HIE-ISOLDE linac.

Keywords: nuclear spin polarization, tilted foils, particle scattering, β-NMR, ISOLDE, REX-ISOLDE, HIE-ISOLDE, post-acceleration

Dedicated to my family,

who always supported

and believed in me.

Contents

Publications pertinent to the work in this thesis

During my time at ISOLDE, I participated in several experiments, both within and beyond the tilted-foils polarization project. The following articles, all directly related to the project or its scientific goals, have been produced in relation to my work and have been published, accepted or are currently under review by scientific journals.

Implementation and evaluation of tilted foils polarization at REX-ISOLDE

H. Törnqvist[1,2], C. Sotty[3], G. Georgiev[3], M. Hass[4], A. Herlert[1,6], M. Kowalska[1], T. Nilsson[2], J. Pakarinen[1] and F. Wenander[5]

[1] Physics Department, CERN, CH-1211 Genève 23, Switzerland

[2] Department of Fundamental Physics, Chalmers University of Technology, SE-412 96 Göteborg, Sweden

[3] CSNSM, University Paris-Sud, Bâtiment 108, F-91405 Orsay, France

[4] Department of Particle Physics, Weizmann Institute, 76100 Rehovot, Israel

[5] Beams Department, CERN, CH-1211 Genève 23, Switzerland

[6] Present address: School of Physics and Astronomy, University of Manchester, Oxford Road, Manchester, M13 9PL, UK.

Reference: H Törnqvist et al 2012 Phys. Scr. 2012 014040.

Tilted Foils Polarization at REX-ISOLDE

H. Törnqvist[1,2], C. Sotty[3], B. Balabanski[4], D. Dhal[5], G. Georgiev[3], M. Hass[5], A. Heinz[2], Y. Hirayama[6], N. Imai[6], H. Johansson[2], M. Kowalska[1], A. Kusoglu[7], T. Nilsson[2], A. Stuchbery[8] F. Wenander[1] and D. T. Yordanov[9]

[1] CERN, Geneva, Switzerland

[2] Fund. Phys., Chalmers, Gothenberg, Sweden

[3] CSNSM, Orsay, France

[4] INRNE, BAS, Sofia, Bulgaria

[5] Dept. of Part. Phys., Weizmann Institute, Rehovot, Israel

[6] Inst. of Part. and Nucl. Stud., High Energy Acc. Res. Org., KEK, Ibaraki, Japan

[7] Dept. of Phys., Istanbul University, Istanbul, Turkey

[8] Dept. of Nucl. Phys., ANU, Canberra, Australia

[9] Max Planck Inst. for Nucl. Phys., Heidelberg, Germany

Accepted for publication in *Nuclear Instrumentation and Methods in Physics Research B.*

Study of the deformation-driving $\nu d_{5/2}$ orbital in $^{67}_{28}Ni_{39}$ using one-neutron transfer reactions

J. Diriken[1,2], N. Patronis[1,3], A. Andreyev[4], A. Antalic[5], V. Bildstein[6], A. Blazhev[7], I. G Darby[1], H. De Witte[1], J. Eberth[7], J. Elseviers[1], V. N Fedosseev[8], F. Flavigny[1], G. Georgiev[9], R. Gernhäuser[6], M. Huyse[1], J. Jolie[7], T. Kröll[6], R. Krücken[6], R. Lutter[10], B. A March[8], T. Mertzimekis[11], D. Mücher [6], R. Orlandi[4], A. Pakou[3], R. Raabe[1], G. Randisi[1], P. Reiter[7], T. Roger[1], M. Seidlitz[7], M. Seliverstov[1,8], C. Sotty[9], H. Törnqvist[12], J. Van De Walle[12], P. Van Duppen[1], D. Voulot[8], N. Warr [7], F. Wenander[8], and K. Wimmer[6]

[1] Instituut voor Kern- en Stralingsfysica, KU Leuven - University of Leuven, Celestijnenlann 200D, B-3001 Leuven, Belgium

[2] Belgian Nuclear Research Centre SCK• CEN, Boeretang 200, B-2400 Mol, Belgium

[3] Department of Physics and HIMP, The University of Ioannina, 45110 Ioannina, Greece

[4] School of Engineering, University of the West of Scotland, Paisley, PA1 2BE, United Kingdom, and the Scottish Universities Physics Alliance (SUPA)

[5] Department of Nuclear Physics and Biophysics, Comenius University, 84248 Bratislava, Slovakia

[6] Physik Department E12, Technische Universität München, D-85748 Garching, Germany

[7] IKP, University of Cologne, D-50937 Cologne, Germany

[8] AB Department, CERN 1211, Geneva 23, Switzerland

[9] CSNSM, CNRS/IN2P3, Universite Paris-Sud 11, UMR8609, F-91405 ORSAY-Campus, France

[10] Fakultät für Physik, Ludwig-Maximilians-Universität München, D-85748 Garching, Germany

[11] INP, NCSR "Demokritos", GR-15310, Ag. Paraskevi/Athens, Greece

[12] PH Department, CERN 1211, Geneva 23, Switzerland

Under review for publication in *Physical Review Letters.*

Study of Bound States in ^{12}Be through Low-Energy ^{11}Be(d,p)-Transfer Reactions

J. G. Johansen[1,2], V. Bildstein[3], M. J. G. Borge[4,5], M. Cubero[5], J. Diriken[6], P. Van Duppen[6], J. Elsevier[6],

L. M. Fraile[7], H. O. U. Fynbo[1], L. P. Gaffney[8], R. Gernhäuser[9], B. Jonson[10], G. T. Koldste[1], T. Kröll[2], D. Mücher[9], T. Nilsson[10], K. Nowak[9], J. Pakarinen[4], V. Pesudo[5], R. Raabe[6], K. Riisager[1], O. Tengblad[5], H. Törnqvist[4,10], D. Voulot[4], N. Warr[11], F. Wenander[4], K. Wimmer[12]

[1] Department of Physics and Astronomy, Aarhus University, DK-8000 Aarhus C, Denmark

[2] Institut für Kernphysik, Technische Universität Darmstadt, D-64289 Darmstadt, Germany

[3] Department of Physics, University of Guelph, Guelph, Ontario, Canada N1G2W1

[4] CERN, CH-1211 Genève, Switzerland

[5] Instituto de Estructura de la Materia, CSIC, E-28006 Madrid, Spain

[6] Instituut voor Kern- en Stralingsfysica, KU Leuven, 3001 Leuven, Belgium

[7] Grupo de Fisica Nuclear, Universidad Complutense, CEI Moncloa, E-28040 Madrid, Spain

[8] Oliver Lodge Laboratory, University of Liverpool, L69 7ZE, England, UK

[9] Physik Department E12, Technische Universität München, 85748 Garching, Germany

[10] Fundamental Fysik, Chalmers Tekniska Högskola, S-41296 Göteborg, Sweden

[11] Institut für Kernphysik, Universität zu Köln, D-50937 Köln, Germany and

[12] National Superconducting Cyclotron Laboratory, East Lansing, Michigan 48824-1321, USA

To be submitted to *Physical Review C.*

Chapter 1

Introduction

The nuclear chart may look like a well detailed map with occasional major updates mainly close to the neutron-rich drip-line and among the heavy isotopes. Still, there are many question marks scattered all over the chart. If resolved, they could provide data to better understand the structure as well as internal and external interactions of the nucleus. There are numerous isotopes which have no assigned ground-state spin and parity and no level schemes for example, even in close proximity to phenomenologically interesting areas, e.g. among the odd-even indium isotopes in the vicinity of the doubly magic ^{132}Sn. Some of the isotopes may be difficult to produce, and some may be difficult to probe with currently available experimental techniques.

Spin is one of the most fundamental and peculiar characteristics of particles and nuclei, an intrinsic angular momentum with no equivalent in classical physics. The concept was introduced and developed during the first half of the 20th century in order to explain certain fine structures in emission spectra and the Stern-Gerlach experiment. The Stern-Gerlach experiment clearly showed quantum properties beyond classical physics, such as how the act of measuring can affect the state of a quantum system and how electron spin is quantized. It turned out that every nucleon in an atomic nucleus possesses a spin and they all add up to a total angular momentum, sometimes referred to as *nuclear angular momentum* or *nuclear spin*. Controlling spin would reduce the degrees of freedom in experiments and more information may be extracted from collected data.

The production of exotic radioactive beams is a violent process and the extracted and separated species of interest require non-trivial manipulation. The typical radioactive beam carries nuclei with equilibrated features with little information content that could be increased by polarization. For certain experiments, it has been possible to repeatedly produce spin-polarized

beams to characterize otherwise inaccessible observables. Examples include determining g-factors of nuclear ground states and long-lived isomeric states, studying nuclear quadrupole moments, and investigating parity violation in weak interaction-processes. Nuclear spin polarized beams are available at many nuclear research facilities today, but generally for isotopes with certain characteristics or in rather narrow energy regimes.

My work has consisted of further developing and evaluating the *tilted foils polarization* technique, to polarize the nuclear spin for use at beam energies usable especially for Coulomb excitation and transfer reactions. The main motivation for this work was that other techniques have a very low efficiency in this energy domain. Tilted foils polarization is based on a beam traversing a set of thin tilted foils made of inert materials, and can be used for a beam of short-lived isotopes. This technique could help to fill in some of the missing data in the present nuclear chart.

Producing nuclear spin polarization with the tilted foils method is technically not very demanding; precise and efficient measurement of the obtained polarization turns out to be more difficult. In fact, two different methods were used to measure the polarization. The first was performed using Coulomb excitation of a beam of stable ^{21}Ne. This method is of interest because of the intermediate energy γ-spectroscopy experimental setups that are available at several nuclear experimental facilities, and the fact that it relies solely on particle scattering kinematics. The downside is that Coulomb excitation reactions exhibit low cross-sections and low signal-to-noise ratio.

The second experiment was based on the β-NMR (Nuclear Magnetic Resonance) technique with β-emitting ^{8}Li nuclei. This is a well-tested approach with high efficiency and provides a clear signal already at low implantation count rates. There was however no β-NMR setup installed at REX-ISOLDE at the start of this project, and part of my thesis work was to design and assemble a β-NMR spectrometer behind the REX accelerator.

Once the tilted foils technique can be reliably used at REX-ISOLDE, the dedicated measuring setup may receive beams other than ^{8}Li, or the foils device may be moved to another experimental setup. One of the major advantages with the tilted foils technique is that the beam energy can be adjusted to a region that cannot be covered by other techniques with high efficiency. Since the beam traverses a stack of foils in-flight, it is possible to post-accelerate it after the polarization has been attained. This thesis will be concluded with information collected from simulations with the upcoming HIE-ISOLDE linac (linear accelerator) using a beam that has been subject to tilted foils polarization.

Chapter 2

Theory and techniques

2.1 Atomic and nuclear orientation

The concept of oriented quantum states was developed in the 1940s, following the development and understanding of the results obtained from ferromagnetic resonance (FMR) [1], electron paramagnetic resonance (EPR) [2] and nuclear magnetic resonance (NMR) [3] experiments. All three techniques are based on the absorption of RF power at specific frequencies in a sample placed inside a strong magnetic field. This is due to resonance with the precessing magnetization vector of the sample, the energy difference of the two spin states of unpaired electrons, and the precessing nuclear angular momentum, for the three techniques respectively. To fully explain these observations, a formalism for *atomic and nuclear orientation* and matter interaction with polarized electromagnetic waves was developed.

Atomic and nuclear orientation describes the distribution of quantum states with respect to a chosen spatial vector. The three simplest types of distributions are uniform, vector-polarized and aligned, which have been depicted in Fig. 2.1. This project is concerned mainly with contributions from the lowest rank tensors, since higher ranks complicate experimental matters rapidly as can be seen in the introductory theory sections later. Any further mention of polarized states will thus be assumed to be vectorial, unless stated otherwise.

Since this project focused on evaluating the application of a technique to polarize the nuclear angular momentum I, the quantum number of interest is m_I with respect to a fixed vector in the laboratory frame. The definition for the degree of nuclear spin polarization used in this thesis is

$$p_I = \frac{1}{\sqrt{I(I+1)}} \sum_i m_i \, \rho(m_i), \tag{2.1}$$

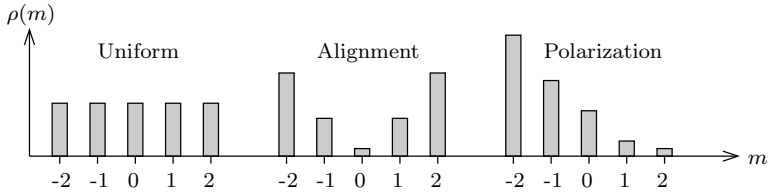

Figure 2.1: The population density $\rho(m_I)$ for three types of state distributions of the m_I quantum number for a group of nuclei with $I = 2$.

where $m_i = m_{I,i}$ are the possible magnetic quantum numbers for m_I-states under the condition $-I < m_I < +I$, and $\rho(m_i)$ is the population density of the given quantum number. The inability to attain 100 % polarization is of course due to the uncertainty principle. Note that some texts express this measure in terms of the limit I rather than the vector length $\sqrt{I(I+1)}$ in which case a value of 100 % can be achieved.

For isolated free quantum systems at room temperature, a near uniform distribution of the quantum states is expected. This follows from the Boltzmann population distribution function

$$\rho(m_i) \propto \exp\left[-\frac{E(m_i)}{k_B T}\right], \tag{2.2}$$

where k_B is Boltzmann's constant, $E(m_i)$ is the energy of the state m_i, and $k_B T \gg hE(m_i)$ at room temperature. Strongly aligned and polarized quantum states are more interesting however, since for example γ- and β-decay are sensitive to the distribution of the nuclear m_I quantum number, which makes them more easily observed. In order to create strongly non-uniform states, the conditions given above must be broken. Before such techniques are explained however, certain aspects of the atom and nucleus shall be covered.

2.1.1 Angular distribution of γ-radiation

The angular distribution of γ-radiation follows $P_{2L}(\cos\theta)$ where P_i is the Legendre polynomials of order i, and θ is the angle of γ-ray emission to a defined spatial axis z. In the case of $I = 1 \to 0$, decays with $m = 0, \pm 1$ are possible. For $m = 0$, the angular distribution is $\propto \sin^2\theta$, and for $m = \pm 1$, it is $\frac{1}{2}(1 + \cos^2\theta)$. The transition probabilities for higher order multipole transitions are relatively small and will not be discussed further here (the theoretical Weisskopf estimates can be found in e.g. [4]). Generally, the observed angular distribution of γ-rays emitted by a decaying nucleus with a known projection axis follows a sum of even-order Legendre polynomials, due

to the parity-conserving nature of γ-decay. This sum is thus an even function around the plane perpendicular to the z axis. Therefore γ-spectroscopy alone can be used to probe aligned and polarized states to some extent, but not to distinguish between the two. The polarization of a single nucleus decaying in a γ cascade can be extracted by observing the angular distribution of consecutive decays, but we are interested in the polarization of an ensemble of nuclei. Proved and proposed methods based on β-decay and particle scattering with γ-tagging of events will be described in detail later.

2.1.2 Hyperfine interaction and polarization transfer

The *fine structure* in atomic spectra is a small separation of the primary energy levels that are characterized by the atomic quantum number n. One effect contributing to this separation is an interaction between the spins of the atomic electrons and their orbital angular momenta, called spin-orbit coupling. There is also an interaction between the atomic electron spins and the nuclear spin which gives rise to an even weaker separation of the energy levels, named the *hyperfine interaction*. The hyperfine interaction was introduced to explain very small energy separations in atomic emission spectra, for example the famous 21 cm-line emitted by neutral hydrogen in space.

The interaction occurs because of the magnetic field that the nucleus experiences, generated by the magnetic moment of electrons bound in an atom. This coupling between the electrons and the nucleus is described as $\boldsymbol{F} = \boldsymbol{J} + \boldsymbol{I}$, where $\boldsymbol{F}$ is the total atomic angular momentum of the atom, $\boldsymbol{J}$ is the electronic angular momentum and $\boldsymbol{I}$ is the nuclear angular momentum. The hyperfine energy-splitting is defined by the relative orientation of $\boldsymbol{J}$ and $\boldsymbol{I}$. Each configuration consists of energetically degenerate sub-levels characterized by m_F, much like the m_J and m_I quantum numbers.

Non-zero electronic nuclear and angular momenta are not conserved in free atoms. They do however couple to and continuously precess around the conserved total atomic angular momentum $\boldsymbol{F}$. Since $\boldsymbol{I}$ and $\boldsymbol{J}$ are coupled, any polarization of either angular momentum will be transferred to the other. For example, as can be seen in Fig. 2.2, polarizing only the electronic angular momentum will cause both $\boldsymbol{I}$ and $\boldsymbol{J}$ to precess around the slightly polarized $\boldsymbol{F}$. The time-average of $\boldsymbol{I}$ will therefore be polarized. Successive polarization of the electronic angular momentum will give an increasing degree of polarization of the nuclear angular momentum.

Assume that the atomic angular momenta in an ensemble of atoms in vacuum are polarized and that the degree of polarization of either can be measured at any given time after polarization. Due to the precessing motion

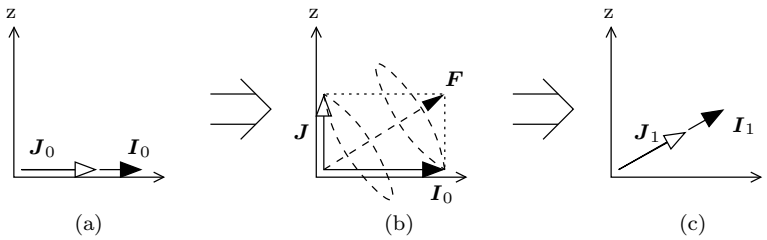

Figure 2.2: Classical view of the transfer of atomic spin polarization to nuclear spin polarization. (a) Angular momenta $\boldsymbol{I}_0$ and $\boldsymbol{J}_0$ uniformly distributed with $\underline{z}$ component zero on average. (b) $\boldsymbol{J}$ polarized will cause both angular momenta to precess around $\boldsymbol{F} = \boldsymbol{I}_0 + \boldsymbol{J}$. (c) On average, both $\boldsymbol{I}_1$ and $\boldsymbol{J}_1$ are polarized.

of $\boldsymbol{I}$ and $\boldsymbol{J}$, the measurement will give a result as a function of time after the initial polarization. This phenomenon is referred to as the hyperfine *quantum beats* [5]. Results from an experiment investigating this effect is shown in Fig. 2.3. Observation of these beats gave inspiration for transferring non-uniform state-distributions of J to I with beam-foil techniques.

The Zeeman effect

Consider a free isolated atom, in which the hyperfine sub-levels defined by m_F are degenerate. If an external magnetic field is applied to the atom, the level energies split according to the linear function

$$\Delta E = m_F \mu_B B, \quad \mu_B = e\hbar/2m_e, \tag{2.3}$$

where ΔE is the energy difference to the level energy in zero magnetic field, B is the magnetic field strength, μ_B is the Bohr magneton and m_e is the rest mass of the electron. As long as the magnetic field is weak, the hyperfine coupling between I and J is strong and the splitting of the m_F states is in large part linear with respect to the available F states. This is the *Zeeman effect*, or weak-field Zeeman effect. As the magnetic field strength increases, the hyperfine coupling diminishes in strength and eventually the electronic and nuclear angular momenta can be considered to be uncoupled. In this case, m_F is no longer a good quantum number. Also, because the electron magnetic moment is larger than the nuclear magnetic moment by a factor 2000, the energy splitting will occur with respect to the m_J quantum number rather than F. This is the *Paschen-Back* effect. The transition between the two effects is smooth but can give a complex re-ordering of levels when many quantum states are involved. The broken degeneracy in the Zeeman effect and the redistribution of the energy levels for the Paschen-Back effect in an

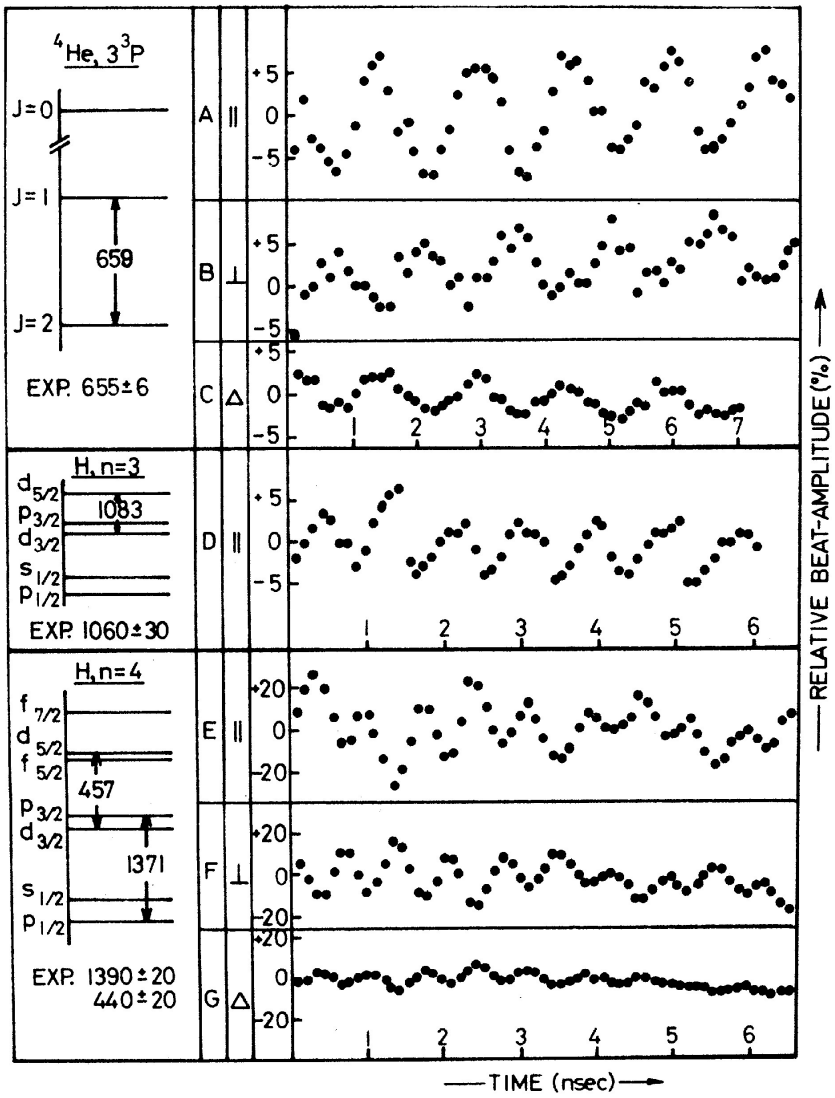

Figure 2.3: Quantum beats as observed by Andrä [5], following a beam-foil interaction. The phenomenon occurs because an observable mostly coupled to only one of the non-conserved precessing spins $\boldsymbol{J}$ and $\boldsymbol{I}$ around the total spin $\boldsymbol{F}$ is measured. $\parallel$ indicates that polarization was measured parallel and $\perp$ perpendicular to the beam axis. $\triangle$ indicates no polarizing filter was applied, interference therefore lowered the beating amplitude. Picture from cited paper.

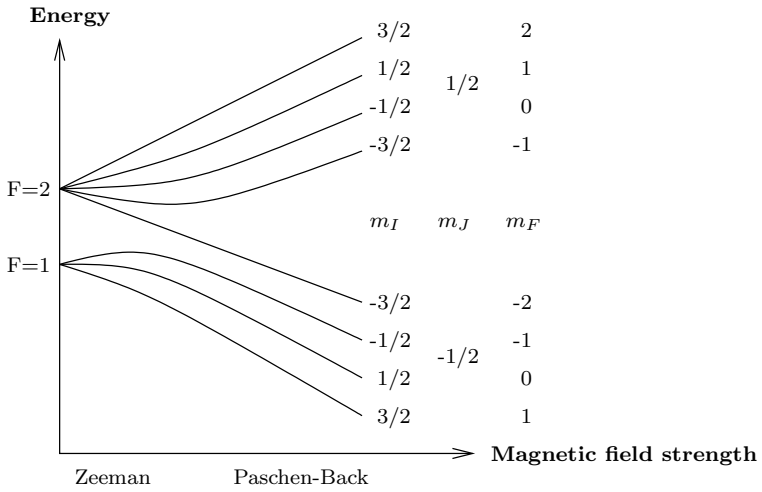

Figure 2.4: Depiction of the weak-field Zeeman and the Paschen-Back effects for a nucleus with nuclear spin $I = 3/2$ and atomic spin $J = 1/2$. The Zeeman effect gives linear splitting of the states from F with I and J coupled. The Paschen-Back effect emphasizes the splitting of J states owing to the reduced coupling strength between I and J at high external magnetic field strengths and due to the strong magnetic moment of electrons. The Breit-Rabi formula is a quantum-mechanical description of the intermediary regime for a system with $J = 1/2$.

isotope with electron spin $J = 1/2$ and nuclear spin $I = 3/2$ is depicted in Fig. 2.4.

This effect must be recognized when strong magnetic fields are introduced in an experiment, since the turn-over field strength for decoupling of I and J is in the order of hundreds to thousands of Gauss. An approximation for this turn-over point will be covered next.

The Breit-Rabi formula

A full model for the line splitting in the intermediate magnetic field strength regime between the Zeeman and Paschen-Back effect is not trivial to determine. The solution for the special case $J = 1/2$ and $I \geq 1/2$ is called the

Breit-Rabi formula [6]

$$\Delta E_{F=I\pm1/2} = -\frac{\delta W}{2(2I+1)} + m_F g_I' \mu_B B_0 \pm \frac{\delta W}{2}\sqrt{1+\frac{4m_F}{2I+1}x+x^2}, \quad (2.4)$$

$$m_F = I \pm 1/2, \quad (2.5)$$

$$g_I' = \frac{m_e}{m_p} g_I \ll g_J, \quad (2.6)$$

$$x = \frac{g_J - g_I'}{\delta W}\mu_B B_0, \quad (2.7)$$

$$\delta W = A\left(I+\frac{1}{2}\right),\ A = \frac{\mu_B \overline{B(0)}}{IJ}, \quad (2.8)$$

where $\Delta E_{F=I\pm1/2}$ is the energy splitting of the two hyperfine levels due to $J = 1/2$, δW is the energy splitting between two hyperfine levels in zero magnetic-field, B_0 is the strength of an external magnetic field, and $\overline{B(0)}$ is the magnetic field strength at the nucleus generated by the atomic electrons. The parameter x is related to weak and strong fields by $x^2 \ll 1$ and $x^2 \gg 1$, respectively. To obtain an approximation for the break-even point for the coupling between I and J, let $x = 1$ and rewrite Eq. 2.7 to

$$B_{\text{coupl}} \approx \frac{A\left(I+\frac{1}{2}\right)}{g_J \mu_B} \quad (2.9)$$

This expression may be used to evaluate the degree of coupling between I and J in external magnetic fields. If external magnetic fields are of the order of B_{coupl}, polarization transfer between I and J may be adversely affected.

2.1.3 Common polarization techniques

Polarization techniques have been developed for some classes of experiments with different experimental configurations and conditions. This section covers briefly a selection of techniques that have been used consistently and successfully for many experiments, and describes how they relate to the requirements for the type of experiments that can be performed at REX-ISOLDE.

Optical pumping

Properly selected, circularly polarized photons from a laser can induce resonant excitation of certain atomic transitions. If the subsequent spontaneous decay to the electronic ground state is combined with repeated excitation,

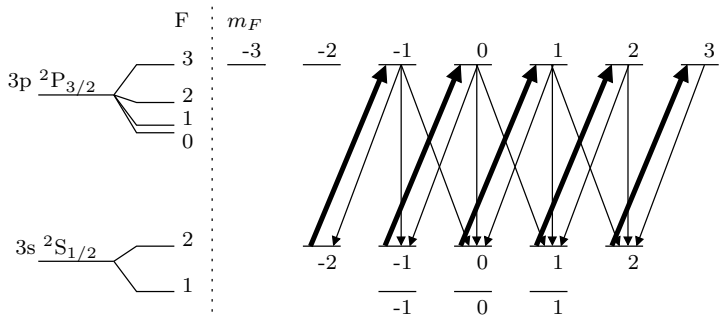

Figure 2.5: The process of optical pumping an atom with $I = 3/2$ with circularly polarized photons (σ^+), showing the expected transitions of an ensemble of nuclei. Circularly polarized photons provide $\Delta l = +1$ and $\Delta m = \pm 1$ transitions when absorbed, where the sign of Δm depends on the photon polarization state. Since at emission $E[\Delta m] = 0$, repeated excitations will "pump" the $\underline{m}$ state to the maximum or minimum in the ground state.

it is possible to populate a specific electronic ground-state quantum state [7]. The m_F quantum number in the ground-state is typically maximized or minimized.

A photon carries an energy $E = h\nu$ and the angular momentum $l_z = \hbar\left(\langle\psi_R\rangle^2 - \langle\psi_L\rangle^2\right)$, with the subscripts R and L denoting right- and left-circular polarization with respect to the direction of propagation. By matching the energy to an atomic transition and selecting polarized photons, it is possible to continuously supply transitions with $\Delta m = +1$ for right-circular polarization (for left-circular polarization, $\Delta m = -1$). The decay can proceed via the three equally probable transitions $\Delta m_F = 0, \pm 1$, so when this process is repeated, the mean change will be $\Delta m_F = +1$ (-1). Given a sufficient number of excitations and decays, the m_F quantum number is thus maximized (minimized) in the ground state. This process is depicted in Fig. 2.5.

The atomic spin polarization is then transferred to the nuclear spin via the hyperfine interaction, which was briefly discussed earlier. If all transitions accessible via the ground-state of an atom are induced, it is possible to reach nuclear spin polarization of up to 80 % [8]. Certain complications make it principally impossible to reach 100 % polariation [9].

Optical pumping has been used successfully for many experiments at COLLAPS, ISOLDE [9, 10, 11] and at OSAKA, TRIUMF [12]. Nuclear polarization as large as 80 % has been achieved at TRIUMF. There are however a few drawbacks for implementing optical pumping with REX-ISOLDE; introducing a collinear laser into the REX linac is a considerable intervention, the direction of polarization needs to be rotated by a guiding field before

entering the bending magnets, and it only functions for atoms with suitable atomic level schemes.

Low-temperature nuclear orientation

As was explained for atomic and nuclear orientation, the Boltzmann distribution describes the population ratios for states with given relative energy levels. By cooling the nuclei of interest to very low temperatures, typically below 0.01 K, and immersing them into a very strong magnetic field of at least several Tesla, the m_I quantum levels are sufficiently split such that the Boltzmann distribution results in a sizable nuclear polarization. The relaxation times to obtain polarized nuclei range from seconds up to several hours [13].

This technique was notably used in 1960 [14] to show that β-decay violates parity conservation, as suggested to solve the so-called $\tau - \theta$ puzzle [15]. Parity conserving emission, such as γ-radiation, follows an angular distribution of even Legendre polynomials that is insensitive to odd nuclear orientation distributions as was discussed earlier. The observation of an asymmetric angular distribution of β-decay therefore showed that an extra odd term is needed and this term violates parity conservation.

The technique has also been used at ISOLDE in the low-energy experimental setup NICOLE to accurately measure g-factors and quadrupole moments of many isotopes [16, 17]. The two drawbacks in implementing this technique at REX-ISOLDE are the long relaxation times to achieve polarization, and the very low temperatures required for ample separation of the quantum states. Both issues will demand trapping or catching the isotopes of interest, rendering this technique practically unusable for post-acceleration of short-lived radioactive nuclei.

Projectile fragmentation

The transverse momentum distribution in the bending plane of the fragments after a projectile fragmentation reaction has been related to the nuclear polarization of the fragments [18] at energies of at least 40 MeV/u. The polarization vectors are aligned with moment vectors that the fragments attain after the reaction, which depend on the momentum differences of the fragments, see Fig. 2.6. With this technique, degrees of polarization of the nuclear spin in the range 5 % to 20 % have been observed [19]. Since the degree of polarization in projectile fragmentation is based on angular momentum transfer, the only restrictions are the availability of pure high-energy beams of the nuclei of interest. The main drawbacks to this approach are the large angu-

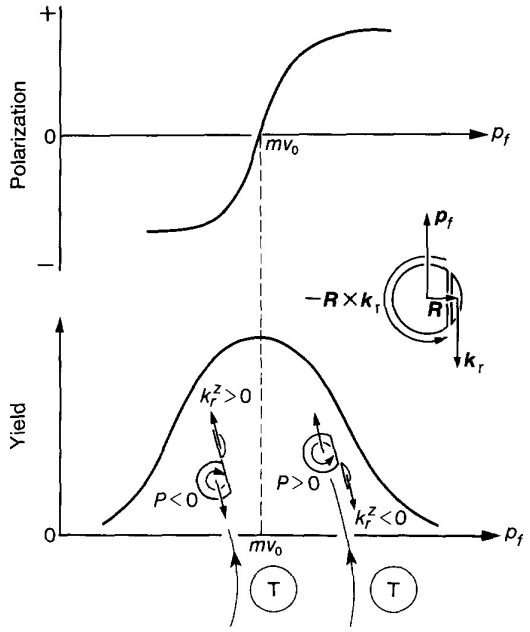

Figure 2.6: Illustration from [19] of the projectile fragmentation polarization technique, showing the process of angular momentum transfer. On either side of the nominal momentum mv_0 after fragmentation, the two nuclear fragments travel at different speeds with momenta p_f and k_r and conservation produces torques that polarize the angular momenta of the fragments. The direction of the polarization vector $\boldsymbol{P}$ is flipped on either side of mv_0.

lar spread, or narrow angular selection, of the polarized beam, and the need for high-energy beams in order to perform projectile fragmentation, which is outside the scope of the current and planned experimental program at ISOLDE.

2.2 Beam-foil interaction

Thin foils of carbon were introduced in beam lines in the 1960s, mainly as stripping foils and to obtain nuclei with excited states induced at precise and determinate times and positions. Observations of nuclei that had passed perpendicularly through a foil at varying distances after the foil has provided life-time measurements of individual nuclear states [20]. It was also discovered that the nuclear states were aligned after the passage, which was shown from the polarization of the emitted γ-radiation. Two independent studies [21, 22] provided theoretical descriptions of the effect, but also suggested that a cylindrically asymmetric interaction could polarize the atomic mag-

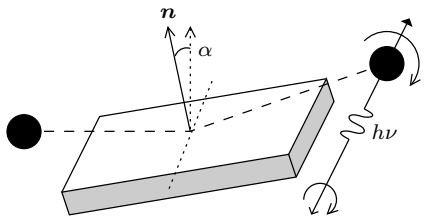

Figure 2.7: Grazing incidence on a copper plate to induce atomic polarization. The tilting angle $\underline{\alpha}$ can be as small as 0.4° which requires very clean conditions and ultra high vacuum. Circular polarization of emitted photons has been observed with a quarter wave plate and a linear polarizer (see [24]).

netic states. Experiments [20] observed the emitted light from nuclei that had traversed a foil tilted at an oblique angle against the beam axis. It was found that the light was indeed circularly polarized, hinting that the atomic state was polarized.

Quantum beats were discovered in early experiments with foil transmission [5]. The experiments recorded the degree of circular polarization of emitted γ-radiation at varying distances after the foil interaction, equivalent to different travel times, see Fig. 2.3. The effect was attributed to the coupling of the atomic and nuclear spins J and I, see Sec. 2.1.2.

2.2.1 Grazing incidence reflection

High degrees of polarization have been obtained in experiments based on grazing incidence reflection against very clean surfaces. With this technique, the nuclear spin of ^{14}N with an incidence angle of 89.6° against the surface normal and a beam energy of 20 keV/u was polarized to 23 % [23], see Fig. 2.7 for a simple illustration of the experiment. Reflection at such angles is challenging due to the geometrical sensitivity, ranging from large scale beam alignment down to the atomic scale conditions on the reflection surface. Vacuum pressures of at least 10^{-8} mbar have been recommended to ensure acceptably low levels of adsorption of contaminants on the reflection surface. Furthermore, a beam diameter of 3 mm, which is a good case beam at REX-ISOLDE, would require a pure reflection surface over 40 cm long. Another possibility is to install strict collimators for a smaller reflection area, but beam transmission yields would suffer. Due to numerous technical demands and complications which are not immediately compatible with the operation of REX-ISOLDE, this technique was not considered for the project.

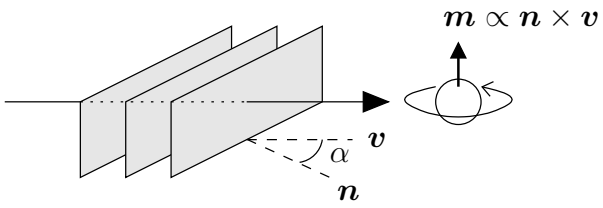

Figure 2.8: The direction of polarization coincides with a torque from the electric interaction between the positive projectiles and the electrons in the foil. The exact mechanisms have not been verified, but the torque model does explain the experimental results. Note that the proportionality constant is positive, so the direction of polarization is identical for all ions.

2.2.2 Tilted foils transmission

Because the introduction of foils in a beam line is relatively non-destructive, this technique could be appropriate for post-acceleration up to energies of several MeV/u. In principle, the only restrictions are non-zero atomic and nuclear spins of the beam ions. Experimental considerations, such as foil thickness and prevention of strong external magnetic fields from interfering with the hyperfine interaction still apply, but are not immediately related to the type of isotopes that can be polarized. The mechanisms for producing nuclear spin polarized atoms will be covered in steps in the following sections.

Atomic and nuclear polarization

The exact process of atomic spin polarization via transmission through a foil is not known, but experiments allow for reliable descriptions of the mechanisms involved [25, 26]. Based on the theory of the asymmetric interaction surface around the beam axis and results from early experiments, it has been suggested that the atomic spin projection is modified by a torque produced between the positively charged projectile ions and the negatively charged atomic electrons in the foil [27]. This view of the process, pictured in Fig. 2.8 and Fig. 2.9, agrees with the polarization direction that has been observed repeatedly in experiments.

When a projectile enters a foil, the atomic spin polarization of the projectile is quickly destroyed by the symmetric distribution of charges inside the foil and also by electron captures and losses. The duration that a polarized ion spends inside of the bulk matter of a thin foil is shorter than the time required for polarization transfer. At the exit surface, the ion is subject to an asymmetric charge distribution and then traverses into vacuum, experiencing no external forces. The larger the foil tilt angle, the larger the degree of

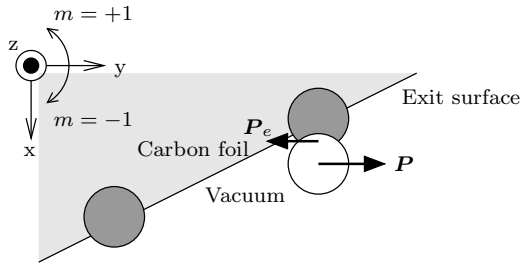

Figure 2.9: Depiction of the interaction between the exit surface of a foil and a traveling ion (white), showing the momentum transfer $\boldsymbol{P}_e$ to the ion with momentum $\boldsymbol{P}$.

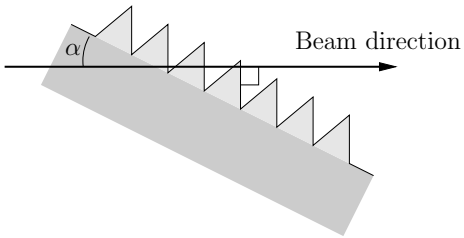

Figure 2.10: The worst case scenario of micro-structures at a foil surface tilted at an angle α to the beam direction, where projectiles exiting the foil would locally be subject to a symmetric surface. There would still be a small net gain of electron pickup on one side which diminishes for larger scale features.

polarization obtained. Assuming that the nucleus of the projectile is mostly shielded by the atomic electrons, the transmission only induces polarization of the electron angular momentum with little interaction with the nucleus.

It is not known exactly how the surface roughness of foils impacts the efficiency of polarization. Grazing incidence experiments have shown that even a small amount of contamination on the reflection surface reduces the attained polarization considerably, but foil transmission seems less sensitive. Reoccurring spatial structures, such as in Fig. 2.10, with large deviations in surface normals could give many exit surface normals almost parallel with the beam trajectory and would effectively reduce the local asymmetry experienced by the exiting beam. However, the long range of the Coulomb interaction must be taken into account with arbitrary surface micro-structures, which makes this a non-trivial problem.

Multi-foil polarization

If the foils are so thin that $\omega_L \tau \ll 1$, where ω_L is the *Larmor precession angular frequency* of $\boldsymbol{I}$ in the intrinsic magnetic fields of the ion, and τ is the

traversal time, there is negligible time for interaction between the electron and nuclear angular momenta. Assuming then that

- the nuclear spin polarization is unaffected by traversing the foil bulk matter,
- the exit surface of a foil provides atomic polarization,
- contributions from orientations with tensor rank > 2 are negligible, and
- $\omega_L \tau \gg 1$ after exit from a foil to allow relaxation of $\boldsymbol{F}$,

the nuclear spin polarization is conserved during passage through a foil but increases in vacuum between successive foils due to the electron spin being polarized at the exit surface of each foil. If $J > I$, then the amount of nuclear spin polarization p_I is saturated at low values with only a few foils, because of the relatively large precession of $\boldsymbol{I}$. However, for $I > J$, p_I can be larger than the electron spin polarization p_J when instead $\boldsymbol{J}$ is subject to the large precession. Ignoring beam speed dependencies and angular and energetic straggling in the foils, the resulting nuclear polarization $p_I(N)$ after N foils can be described with the set of general expressions [28]

$$p_I(N) = p_I(\infty) \left\{ 1 - \left[1 - \frac{p_I(1)}{p_I(\infty)} \right]^N \right\}, \tag{2.10}$$

$$p_I(\infty) = \frac{p_J}{p_J + (1 - p_J)\frac{J}{I}}, \tag{2.11}$$

$$p_I(1) = p_J P(I, J), \tag{2.12}$$

$$P(I, J) = \frac{\langle I_z \rangle_{\phi\theta}}{I} = \frac{1}{4\lambda^2} \left\{ 2\lambda + (\lambda^2 - 1) \ln \left(\frac{1 + \lambda}{1 - \lambda} \right) \right\}, \tag{2.13}$$

$$\lambda = \frac{2IJ}{I^2 + J^2}, \tag{2.14}$$

An illustration of the increase in nuclear spin polarization by multiple foils can be seen in Fig. 2.11, and calculations based on the multi-foil theory for a selection of parameters are presented in Fig. 2.12.

The beam energy plays an important role in the obtained degree of polarization, as clearly shown in [29]. Low beam energies, in the order of 100 keV/u, are generally favored also for heavier beams (e.g. [30]). For a large number of foils, the above energy-independent expressions may therefore break down when directly comparing theoretical curves to experimental data, but could provide some insight in comparisons between similar experiments.

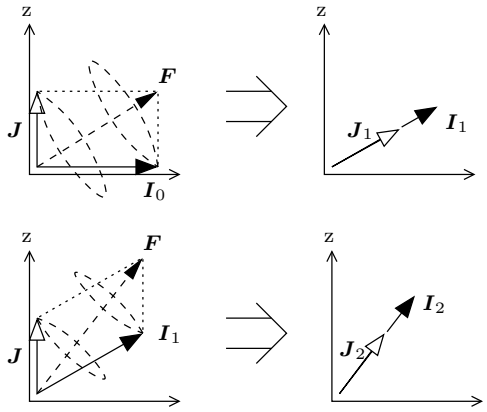

Figure 2.11: Illustration of multi-foil transfer of polarization from the electron spin to the nuclear angular momentum, in a classical view. Top row: repeat of Fig. 2.2; a polarized electron angular momentum causes a polarized nuclear angular momentum. Bottom row: a second polarization of J increases the polarization of I even further.

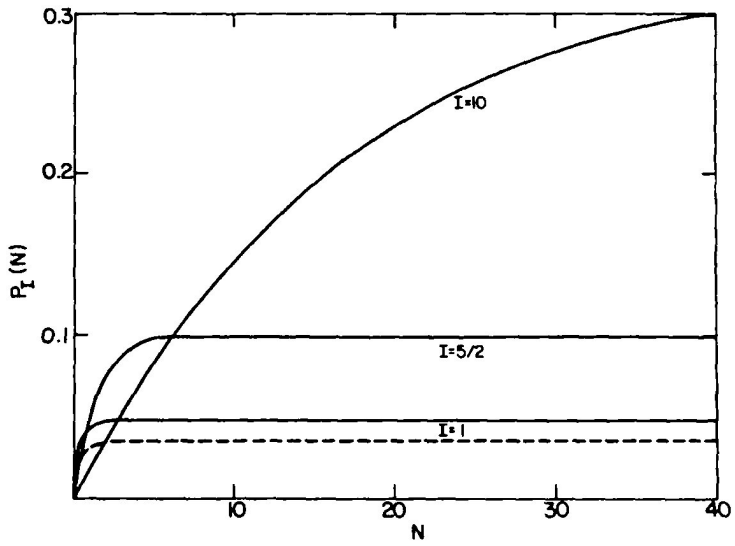

Figure 2.12: The degree of polarization in the multi-foil theory versus the number of foils and nuclear spin of the beam for $J = 5/2$ and $p_J = 0.1$ after passage through each foil. Notice how low-spin nuclei reach polarization saturation after only a few foils and additional foils would only cause stronger energy loss and angular straggling. From [28].

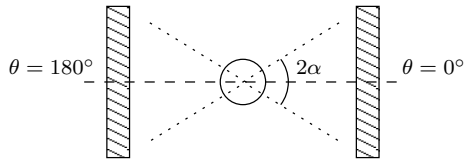

Figure 2.13: Illustration of two particle detectors on either side of an ensemble nuclei that undergo β-decay, in order to measure the counting asymmetry $\varepsilon = (R-L)/(R+L)$, where R and L are the counts from each particle detector. This asymmetry is related to the nuclear polarization along the axis between the two detectors.

2.3 β-decay asymmetry

The parity violation in β-decay, as discussed in Sec. 2.1.3, gives rise to an angular asymmetry of the β-particles and can provide a sensitive probe of polarization. Neglecting external influences, the unperturbed angular distribution of β-decay particles can be written as [31]

$$W(\theta) = \sum_k A_k B_k(I) P_k(\cos\theta), \tag{2.15}$$

where A_k are the asymmetry parameters which depend on the type of decay [32], B_k are the orientation parameters for the nuclear spin, $P_k(\cos\theta)$ are the Legendre polynomials, and θ is the angle between the directions of observation and orientation of the nuclear spin. Parity conserving radiation will only allow even terms in the sum, but since β-decay violates parity, the first odd term must be non-zero as

$$W(\theta) = 1 + A_1 \beta p_I \cos\theta + \text{H.O.T.}, \tag{2.16}$$

where $\beta = v/c$ is the relativistic speed of the emitted β particle which can be derived from the kinetic energy of the particle. Terms of higher order $k > 1$ will be neglected, since we are interested only in vector-polarization, and the higher order terms tend to be comparatively small. For completeness, it should be noted that the approximation is valid for first-allowed β-decay. Integrating over the solid angle of two detectors, each around the two poles $\theta = \{0, \pi\}$ with an opening angle 2α (as depicted in figure Fig. 2.13), gives

$$\begin{aligned} N_{R,L} &= \int_0^{2\pi} \int_0^{\alpha} (1 \pm A_1 \beta p_I \cos\theta) \sin\theta d\,\theta d\,\varphi \\ &= 2\pi \left[1 - \cos\alpha \pm \frac{A_1 \beta p_I}{2} (1 - \cos^2\alpha) \right], \end{aligned} \tag{2.17}$$

where R and L correspond to the plus and minus sign, respectively, and $N_{R,L}$ is the number of counts in the right or left detector. In order to solve for the polarization of the nuclear spin, form an expression for the relative difference in counts, also referred to as the counting asymmetry ε given by

$$\varepsilon = \frac{R - L}{R + L} = \frac{A_1 \beta p_I (1 - \cos^2 \alpha)}{2(1 - \cos \alpha)}, \tag{2.18}$$

$$p_I = \frac{2(1 - \cos \alpha)}{A_1 \beta (1 - \cos^2 \alpha)} \, \varepsilon. \tag{2.19}$$

This expression provides a lower limit for the degree of polarization, since background events and noise tend to be uniformly introduced on R and L. Some issues, such as the destruction of polarization in the target environment until β-decay occurs, and detection efficiency factors moving the symmetry baseline from zero, will be treated after the concept of β-NMR has been covered.

2.3.1 β-NMR

Nuclear magnetic resonance (NMR) [3] is based on the stimulation and observation of nuclear magnetic moments as they interact with their local surroundings in an external magnetic field. The interactions can be probed by observing changes to the magnetic moments, such as precession and relaxation rates. There are many variations on the exact application of this technique for different purposes. For example, the external magnetic field is homogeneous, especially for measuring features of an ensemble of constituent matter, but it can be made a function of position to measure instead the spatial structure of a sample. The classical application of NMR relies on polarizing nuclei in a sample by using a strong magnetic field, whereas for β-NMR, polarized β-active nuclei are implanted into the sample. For the purposes of this project, the β-NMR with a static homogeneous holding field is the most suitable.

Experimental procedure

β-active ions with polarized nuclear spin can be delivered as a continuous or pulsed beam depending on the experiment. The ions are implanted into a target, typically a crystal with symmetric electric field gradients. The ionic electrons lose their polarization in the target, but provide shielding for the nucleus. At room temperature, the relaxation rate of the nuclear spin polarization can be up to several seconds. The ions decay in the target crystal and create an asymmetric distribution of β particles. Measuring the

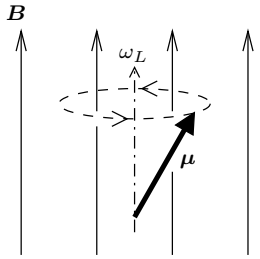

Figure 2.14: Larmor precession of a non-zero spin particle in a homogeneous magnetic field, which is directly proportional to the total spin and the magnetic field strength, see Eq. 2.21.

distribution, with two detectors as described earlier for example, can give clues to the implanted ions, the structure of the target or the interaction between the two. For this project, any cubic target which gives a relaxation time for the polarization longer than the life-time of the beam nuclei would be a good choice.

Mechanisms of β-NMR

The magnetic moment of a non-zero spin nucleus is

$$\boldsymbol{\mu}_N = \gamma_N \boldsymbol{I}, \quad \gamma_N = \frac{g_N \mu_N}{\hbar}, \quad \mu_N = \frac{e\hbar}{2m_p}, \tag{2.20}$$

where g_N is the g-factor of the nucleus, μ_N is the nuclear magneton, γ_N is the gyromagnetic ratio, e is the elementary charge and m_p is the rest mass of the proton. The g-factor is a dimensionless quantity that relates an appropriate unit of magnetic moment (in this case the nuclear magneton) with the gyromagnetic ratio and is characteristic for particles or nuclei. The interaction between any magnetic moment and an external magnetic field gives rise to *Larmor precession*, a circular precessing motion around the magnetic field lines, see Fig. 2.14. The precessing motion can be described with

$$\boldsymbol{\tau}_L = \boldsymbol{\mu} \times \boldsymbol{B}, \quad \omega_L = -\gamma B, \tag{2.21}$$

where $B = |\boldsymbol{B}|$ is the strength of the external magnetic field. The negative sign indicates the direction of the precessing motion in a right-handed coordinate system and will be important later.

An RF field can be applied to interact with the magnetic moments and changes can be observed. In its simplest application, the RF can be used to disturb the precession of the magnetic moments around the holding field to

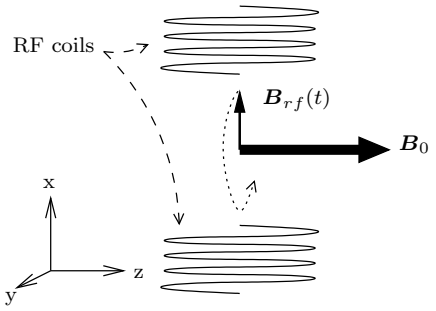

Figure 2.15: Illustration of the magnetic fields in the β-NMR. $\boldsymbol{B}_0$ represents the static holding field from the β-NMR magnet and $\boldsymbol{B}_{\rm rf}$ is the harmonic linearly polarized field produced by the RF coils. When the rotation rate of $\boldsymbol{B}_{\rm rf}$ matches the Larmor frequency of a spin system, the precession angle is disrupted and the spatial orientation of the spin system is lost (see Eq. 2.34).

create a uniform angular distribution. This is of use to isolate effects that can be observed with β-NMR from errors introduced by the experiment. Following the derivations in Ref. [31], one can consider the precessing motion for a particle with magnetic moment $\boldsymbol{\mu}$ in a magnetic field $\boldsymbol{B}$. The Hamiltonian for this system can be written as

$$\mathcal{H} = -\boldsymbol{\mu} \cdot \boldsymbol{B}. \tag{2.22}$$

The contribution to the magnetic field from a static holding field in the z axis can be written $\hat{\boldsymbol{z}}B_0$. The applied RF can be represented by a time-dependent magnetic field. An idealized view of the full field from the RF coils is a linearly polarized field that oscillates in a plane perpendicular to the z axis, refer to Fig. 2.15. However, linear polarization can be described as the sum of left and a right circular polarization, which is interesting for reasons that will be clear soon. Therefore, the Hamiltonian with both the holding field and the RF field rotating with frequency $\omega_{\rm rf}$ is

$$\begin{aligned}\mathcal{H} &= -\boldsymbol{\mu} \cdot \{\hat{\boldsymbol{z}}B_0 + [\hat{\boldsymbol{x}}\cos(\omega_{\rm rf}t + \Delta) + \hat{\boldsymbol{y}}\sin(\omega_{\rm rf}t + \Delta)]\, B_{\rm rf}\} \\ &= -\gamma\,\{I_z B_0 + [I_x\cos(\omega_{\rm rf}t + \Delta) + I_y\sin(\omega_{\rm rf}t + \Delta)]\, B_{\rm rf}\}\end{aligned} \tag{2.23}$$

where Δ is an initial phase shift for generality. The general expression for a rotation by a finite angle ϕ in operator-form is

$$\hat{D}(\hat{\boldsymbol{n}}, \phi) = \exp\left(-i\phi\frac{\hat{\boldsymbol{n}} \cdot \boldsymbol{J}}{\hbar}\right) \tag{2.24}$$

where $\boldsymbol{J}$ is the angular momentum operator. This can be used to replace the

contribution from the RF with

$$\hat{D}_z(\theta) = \exp\left(-i\frac{\theta I_z}{\hbar}\right), \tag{2.25}$$

$$I_x\cos(\theta) + I_y\sin(\theta) = \hat{D}_z(\theta) I_x \hat{D}_z^\dagger(\theta), \tag{2.26}$$

so the Hamiltonian can be written as

$$\mathcal{H} = -\gamma\left[I_z B_0 + \hat{D}_z(\omega_{\mathrm{rf}}t + \Delta) I_x \hat{D}_z^\dagger(\omega_{\mathrm{rf}}t + \Delta) B_{\mathrm{rf}}\right]. \tag{2.27}$$

In order to eliminate the time-dependency, we can introduce a rotating frame. The effect of a rotating frame on a Hamiltonian in quantum mechanics will be covered next.

Assume first that the Hamiltonian is suitable for use with the Schrödinger equation, i.e. for some wave-function Ψ

$$i\hbar\frac{\partial}{\partial t}\Psi = \mathcal{H}\Psi. \tag{2.28}$$

Transform the wave-function Ψ in the lab frame to $\tilde{\Psi}$ in a new frame by the general unitary transformation $\hat{U}(t)$ with

$$\tilde{\Psi} = \hat{U}^\dagger(t)\Psi. \tag{2.29}$$

Apply Eq. 2.28 to $\tilde{\Psi}$ to get

$$\begin{aligned} i\hbar\frac{\partial[\hat{U}^\dagger(t)\Psi]}{\partial t} &= i\hbar\left[\frac{\partial\hat{U}^\dagger(t)}{\partial t}\Psi + \hat{U}^\dagger(t)\frac{\partial\Psi}{\partial t}\right] \\ &= i\hbar\left[\frac{\partial\hat{U}^\dagger(t)}{\partial t} + \hat{U}^\dagger(t)\frac{\mathcal{H}}{i\hbar}\right]\Psi \\ &= \left[\hat{U}^\dagger(t)\mathcal{H}\hat{U}(t) + i\hbar\frac{\partial\hat{U}^\dagger(t)}{\partial t}\hat{U}(t)\right]\hat{U}^\dagger(t)\Psi. \end{aligned} \tag{2.30}$$

In this case, letting the transformation be a rotation according to Eq. 2.25, but with a time-dependency and an initial phase shift, gives

$$\hat{U}(t) = \exp\left[-i\frac{I_z(\omega t + \Delta)}{\hbar}\right] \tag{2.31}$$

where ω is the rotational speed of the rotating frame. With this transformation, the Hamiltonian in the rotated frame is

$$\tilde{\mathcal{H}} = \hat{U}^\dagger(t)\mathcal{H}\hat{U}(t) - I_z\omega. \tag{2.32}$$

where ω is the rotational speed. This extra term to the transformed Hamiltonian in the rotating frame is generally compared to the Coriolis effect in classical mechanics. The classical force-term is $\propto \boldsymbol{\Omega} \times \boldsymbol{v}$, and in this case z components commute with the Coriolis term.

Applying Eq. 2.32 to Eq. 2.27 gives

$$\tilde{\mathcal{H}} = -\gamma \left[I_{\tilde{z}} B_0 + I_{\tilde{x}} B_{\mathrm{rf}} \right] - I_{\tilde{z}} \omega_{\mathrm{rf}}. \tag{2.33}$$

The first term is the Larmor precession in a static magnetic field $\boldsymbol{B}_0$ with the precession rate $-\omega_0$, so we can match axial components to obtain

$$\tilde{\mathcal{H}} = -\gamma \left[I_{\tilde{z}} \left(1 - \frac{\omega_{\mathrm{rf}}}{\omega_0} \right) B_0 + I_{\tilde{x}} B_{\mathrm{rf}} \right]. \tag{2.34}$$

At resonance, $\omega_{\mathrm{rf}} = \omega_0$, and regardless of the strength of the RF field in principle, the rotation is independent of $I_z = I_{\tilde{z}}$. The rotation takes place instead around the rotating $\tilde{x}$ axis. The nuclear angular momentum will therefore point in any direction in the $x - y$ plane on average, and any time-averaged polarization with respect to the z axis is gone. This effect can be used to identify whether a potential signal for polarization comes from an oriented nuclear spin or experimental errors.

Efficiency factors and the double ratio

Experimental errors due to efficiency factors can give an offset in the counting asymmetry, but this artifact can be reduced by taking several experimental configurations into account

$$\varepsilon = \frac{R - L}{R + L} = \frac{1 - L/R}{1 + L/R} = \frac{1 - \rho}{1 + \rho}, \tag{2.35}$$

$$\rho = f(L_1, R_1, L_2, R_2, ...), \tag{2.36}$$

where the function f calculates the ratio L_i/R_i via the geometric mean with equivalent experimental configurations denoted i. The two possibilities that were evaluated for this project are

$$\rho_{\mathrm{tilt}} = \sqrt{\frac{L_{+\theta}}{R_{+\theta}} \frac{R_{-\theta}}{L_{-\theta}}}, \tag{2.37}$$

$$\rho_{\mathrm{rf}} = \frac{L_{\mathrm{on}}}{R_{\mathrm{on}}} \frac{R_{\mathrm{off}}}{L_{\mathrm{off}}}. \tag{2.38}$$

Note that the counting ratio with respect to the tilt angle is a geometric mean, but for the RF the counting ratio with RF on is expected to be unity. The first alternative neglects new efficiency factors that are introduced when the foil angle changes the geometrical configuration of the experiment. For this project, only the second alternative with RF was used for the β-NMR.

Spin-lattice relaxation

The electromagnetic interaction between implanted spin polarized nuclei and an implantation target will equilibrate the spin states in time and the implanted nuclei will carry increasingly uniform states. In order to cancel this inherent decrease in measured nuclear spin polarization, two effects need to be take into consideration: the relaxation ratio

$$f_r(t) = e^{-t\frac{\ln 2}{\tau_r}}, \tag{2.39}$$

and the decay curve

$$N(t)/N(t=0) = e^{-t\frac{\ln 2}{\tau_{1/2}}}, \tag{2.40}$$

where time t is $t = 0$ at implantation for a nucleus, τ_r is the relaxation time and $\tau_{1/2}$ is the half-life. The average relaxation factor r is the combination of the decay rate $f_d(t)$ and relaxation ratio $f_r(t)$ at corresponding times and is

$$f_d(t) = -\frac{d}{dt}\left[N(t)/N(t=0)\right] = \frac{\ln 2}{\tau_{1/2}}\, e^{-t\frac{\ln 2}{\tau_{1/2}}}, \tag{2.41}$$

$$\frac{1}{\tau} = \frac{1}{\tau_{1/2}} + \frac{1}{\tau_r}, \tag{2.42}$$

$$\begin{aligned} r &= \int_0^\infty f_d(t)\, f_r(t)\, dt \\ &= -\frac{\tau}{\tau_{1/2}}\left[e^{-t\frac{\ln 2}{\tau}}\right]_0^\infty = \frac{\tau}{\tau_{1/2}}. \end{aligned} \tag{2.43}$$

The final expression to obtain the polarization from the experimental detector counts, taking into account detection efficiencies and relaxation, is

$$p_I = \frac{2(1-\cos\alpha)}{A_1\beta(1-\cos^2\alpha)}\frac{\tau_{1/2}}{\tau}\frac{1-\rho_{\mathrm{rf}}}{1+\rho_{\mathrm{rf}}}. \tag{2.44}$$

with ρ_{rf} from Eq. 2.38. There are more factors which may reduce the counting asymmetry, e.g. electron back-scattering and implantation in places other than the target crystal. Compared to the effects treated in this section, any remaining effects should be comparatively small, but the polarization values presented in the results section should still be considered to be lower estimates.

2.4 Particle scattering and Coulomb excitation

The electromagnetic potential between two ideal point charges can reach arbitrary strengths in collisions, due to the inverse dependence on distance. Because the electromagnetic force is well known, it can be a dependable tool to probe related observables in nuclei. Given a sufficiently small impact parameter (the distance far away from the target nucleus between the projectile trajectory and a parallel head-on trajectory) in a collision between a projectile and a target nucleus, the electromagnetic potential in the collision may exceed the energy levels of excited states in the nuclei. The collisional energy can then excite either nucleus or both nuclei. There is however also a lower limit on the impact parameter, since the more complicated strong nuclear interaction may take precedence beyond the Coulomb barrier in high-energy collisions. This is a very simple description of *Coulomb excitation*, an inelastic type of purely electromagnetic particle scattering [33].

This section will not delve deeply into Coulomb excitation, because there is ample literature on the subject, e.g. [33]. The general treatment is not immediately applicable for polarization analysis, however. Most of the literature concentrates mainly on resolving nuclear levels, the characteristics of emitted γ-radiation and their relationships. The γ-ray angular distribution can not be used to correctly classify nuclear spin polarization, and the trajectory due to the in-elastic collision is typically approximated by elastic Rutherford scattering which is symmetric around the beam axis. Therefore, a full treatment of particle scattering with nuclear orientation will be shown in the next section.

One important aspect of Coulomb excitation is the so-called *safe energy*. This signifies the energy threshold where, in a collision with a zero impact parameter, the strength of the nuclear force can become significant in the collision. However, to maximize the Coulomb excitation cross section to populate the first excited state, the energy should be as high as possible. In order to ensure a high rate of purely electromagnetic collisions, the energy of the beam must be close to but still below the safe energy. A classical approximation of the safe energy for medium to heavy nuclei is [34]

$$E_{max} = 1.44\,\frac{A_1 + A_2}{A_2} \cdot \frac{Z_1 Z_2}{r_0(A_1^{1/3} + A_2^{1/3}) + d_s}. \tag{2.45}$$

where subscript 1 indicates the projectile and 2 the target, r_0 is the charge radius coefficient in the expression $R = r_0 A^{1/3}$, and d_s is the distance between the nuclear surfaces. This approximation is based on classical mechanics with

the criterion of a minimum separation distance, which at $d_s = 5\,\mathrm{fm}$ gives a contribution from nuclear forces of less than 0.1 %. This was determined based on empirical behavior of reorientation effects of the target nuclear symmetry axis in nuclear collisions, which are characteristic of electromagnetic and nuclear forces.

2.4.1 Polarization analysis

The derivations in this section are based on [35, 36], which provide further details and more possibilities for using scattering kinematics to analyze polarization.

Under rotation around the z axis, the total spin of a fully polarized ensemble of nuclei should be invariant. In terms of the density matrix ρ over spin states, letting

$$\rho = D_z \, \rho \, D_z^\dagger, \tag{2.46}$$

where D_z is a rotation operator for a rotation around the z axis, it can be shown that ρ must be diagonal. In the field of nuclear orientation, the density matrix formalism is readily replaced by irreducible statistical tensors, which can be directly related to the density matrix

$$t_{kq} = \hat{s} \sum_{\mu\mu'} (-1)^{s-\mu} \langle ss; \mu' - \mu | kq \rangle \rho_{\mu\mu'}, \tag{2.47}$$

$$\rho_{\mu\mu'} = \frac{1}{\hat{s}} \sum_{kq} (-1)^{s-\mu} \langle ss; \mu' - \mu | kq \rangle t_{kq}, \tag{2.48}$$

where s is the spin of the particle under consideration, $\hat{s} = \sqrt{2s+1}$, k $(0 \leq k \leq 2s)$ is called the *rank* of the statistical tensor and q $(-k \leq q \leq k)$ covers the possible components within the rank. The factors $\langle ss; \mu' - \mu | kq \rangle$ are the Clebsch-Gordan coefficients (CGC). The main motivation for introducing the irreducible statistical tensors is the simpler transformation properties compared to the density matrix. For example, choosing an integer or half-integer spin s, the set of tensors $t_{(k=s)q}$ is rotationally independent from $t_{(k\neq s)q}$, whereas the diagonal terms in the density matrix formalism are mixed under rotation. Also, the expression of t_{00} simplifies to the expectation value of the unit operator, thus $t_{00} = 1$ for normalized states, which makes some expressions very clear.

The Wigner 3j-symbol is a common alternative to express statistical tensors. The relationship between CGCs and the Wigner 3j-symbol is

$$\langle j_1 j_2; m_1 m_2 | j_1 j_2; jm \rangle = (-1)^{j_1 - j_2 + m} \sqrt{2j+1} \begin{pmatrix} j_1 & j_2 & j \\ m_1 & m_2 & -m \end{pmatrix}, \tag{2.49}$$

so that the irreducible statistical tensors, as written in this report, take the form

$$t_{kq} = \hat{s} \sum_{\mu\mu'} (-1)^{s-\mu+q} \sqrt{2k+1} \begin{pmatrix} s & s & k \\ \mu' & -\mu & -q \end{pmatrix} \rho_{\mu\mu'}. \tag{2.50}$$

For brevity, the rest of this section will use t_{kq} with an implicit density matrix.

In terms of the irreducible statistical tensors, the polarization can be described by inserting Eq. 2.48 to Eq. 2.46. Because the density matrix must be diagonal, any CGCs for $\mu \neq \mu'$ must be zeroed by t_{kq}. Following the notation in Eq. 2.47, CGCs are in general non-zero only for $q = \mu - \mu'$, and thus

$$t_{kq} = 0 \text{ for } q \neq 0. \tag{2.51}$$

In a scattering reaction with conserved parity, there will be a symmetry plane coplanar to the trajectory of the scattered particle. Let the normal of this plane be y, let z be parallel with the momentum of the incoming particle prior to the reaction and let x be perpendicular to both y and z, all three forming an orthogonal right-handed coordinate system. This coordinate system is normally referred to as the *helicity frame*. A reflection can be performed by a full parity operation and a rotation by π around y which is parallel with the normal of the reflection plane. The CGCs are invariant under the parity operation, and the rotation operator for an angle π around the y axis for CGCs can be written as

$$d^k_{mm'}(\theta = \pi) = (-1)^{k-m} \, \delta_{m-m'}. \tag{2.52}$$

The parity and rotation operations together give a second constraint on the statistical tensors for a polarized spin system in a scattering reaction with conserved parity

$$t_{kq} = (-1)^{k+q} \, t_{k-q}. \tag{2.53}$$

The final detection in an experiment does not only depend on the particles under observation but also on the detection system. The efficiency of the detectors can be expressed by the statistical tensor T_{kq} and is referred to as the *analyzing power*. Given the counting rates $w = w(t_{kq})$ in an experiment, the analyzing power is defined as

$$w(t_{kq}) = N \sum_{kq} t_{kq} T^*_{kq}, \tag{2.54}$$

where N is a normalization coefficient, or in terms of the reaction cross section

$$\left(\frac{d\sigma}{d\Omega}\right)_{\text{pol}} = \left(\frac{d\sigma}{d\Omega}\right)_0 \sum_{kq} t_{kq} T^*_{kq}, \tag{2.55}$$

where $\left(\frac{d\sigma}{d\Omega}\right)_{\text{pol}}$ and $\left(\frac{d\sigma}{d\Omega}\right)_0$ are the cross sections for a polarized and an unpolarized incoming particle, respectively. Because the cross section must be real and scalar under rotations of t_{kq}, the analyzing powers must obey the same two rules Eq. 2.51 and Eq. 2.53 as t_{kq}.

High-spin systems are more complex, so the simplest $s = 1/2$ will be shown first as an example. In this case, it is generally easier to rewrite the spherical tensors in terms of Cartesian tensors, which in the helicity frame are

$$\mathbf{p} = \frac{1}{s}\text{Tr}(\mathbf{s}\rho), \tag{2.56}$$

$$p_z = t_{10}, \tag{2.57}$$

$$p_x = \frac{1}{\sqrt{2}}\left(t_{1-1} - t_{11}\right), \tag{2.58}$$

$$p_y = \frac{i}{\sqrt{2}}\left(t_{1-1} + t_{11}\right), \tag{2.59}$$

and similarly for the analyzing power $\mathbf{A} = (A_x, A_y, A_z)$ based on T_{kq}. From Eq. 2.53, $p_x = p_z = A_x = A_z = 0$, yielding that the polarization is directly related only to p_y in such reactions. Inserting the Cartesian tensors in Eq. 2.55 gives

$$\left(\frac{d\sigma}{d\Omega}\right)_{\text{pol}} = \left(\frac{d\sigma}{d\Omega}\right)_0 (1 + \mathbf{p}\cdot\mathbf{A} + ...) = \left(\frac{d\sigma}{d\Omega}\right)_0 (1 + p_y A_y + ...), \tag{2.60}$$

where the omitted terms denote higher order tensor contributions from spin systems with spin higher than 1/2, and can be left out for this case. Assuming that a detector is placed to the "left" in the scattering plane, for example along the positive x axis in the helicity frame with y pointing up, the count rate of detections can be written

$$L = N(1 + p_y A_y). \tag{2.61}$$

Similarly, for the "right" side, following a rotation of the analyzing power by the angle π around the beam axis z

$$A'_y = e^{i\pi k} A_y = -A_y, \tag{2.62}$$

$$R = N(1 - p_y A_y). \tag{2.63}$$

Canceling out the detection count N, the following accessible expression is obtained

$$\frac{L-R}{L+R} = p_y A_y, \tag{2.64}$$

which shows that for a spin-1/2 particle the observed experimental scattering asymmetry is directly proportional to the nuclear polarization, with the analyzing power of the detector as a proportionality factor. The analyzing power needs to be determined from an experiment with a known non-zero p_y, preferably using a beam of particles with large expected polarization. Note that the efficiency factor reduction as performed for the β polarization analysis applies to the final evaluation of this asymmetry as well.

To conclude this section, let us consider the nucleus of ^{21}Ne with nuclear spin $I = 3/2^+$; a scattering experiment with this nucleus will be covered in Chap. 3. The high-rank tensors will introduce many terms in Cartesian tensor form, but again Eq. 2.53 can be used to cancel out most terms which gives

$$\begin{aligned} d_{z^2} &= t_{20}, \\ d_{xz} &= 0, \\ d_{yz} &= 0, \\ d_{xy} &= 0, \\ d_{x^2-y^2} &= \sqrt{1/2}\,(t_{2-2} + t_{22}), \end{aligned} \tag{2.65}$$

$$\begin{aligned} f_{z^3} &= 0, \\ f_{xz^2} &= 0, \\ f_{yz^2} &= i\sqrt{1/2}\,(t_{3-1} + t_{31}), \\ f_{z(x^2-y^2)} &= 0, \\ f_{xyz} &= 0, \\ f_{x(x^2-3y^2)} &= 0, \\ f_{y(3x^2-y^2)} &= i\sqrt{1/2}\,(t_{3-3} + t_{33}), \end{aligned} \tag{2.66}$$

and similarly for the analyzing powers. Eq. 2.55 becomes

$$\begin{aligned} \left(\frac{d\sigma}{d\Omega}\right)_{\text{pol}} = \left(\frac{d\sigma}{d\Omega}\right)_0 (1 + p_y A_y + \\ d_{z^2} D_{z^2} + d_{x^2-y^2} D_{x^2-y^2} + \\ f_{y(3x^2-y^2)} F_{y(3x^2-y^2)} + f_{yz^2} F_{yz^2}). \end{aligned} \tag{2.67}$$

Even if we are only interested in the first rank tensor p_y (following our definition of polarization from Eq. 2.1), the higher order tensors will influence the polarization cross section and must be removed. Again, by rotating the tensors around the beam axis, it is possible to extract the interesting terms from several measured detection asymmetries, although note that the sign of the quadripolar tensors will not change. One approach to cover all terms is to provide many experimental configurations, e.g. by changing detector

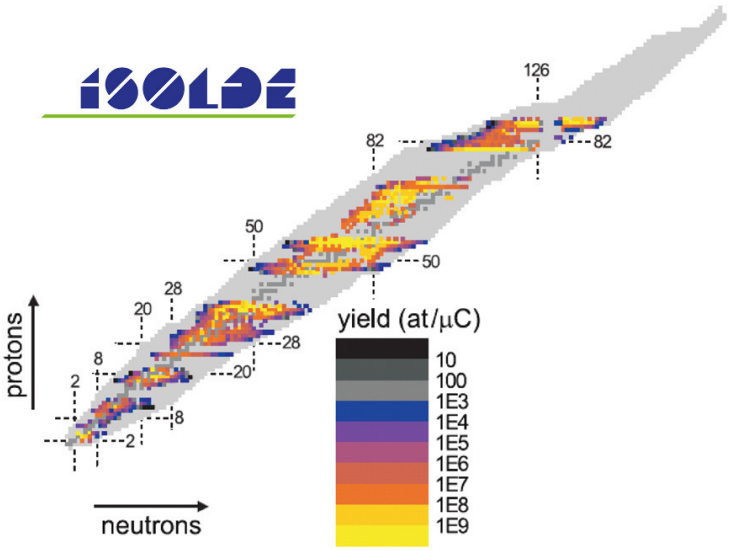

Figure 2.16: Yields of isotopes successfully produced and extracted at the ISOLDE facility for low-energy 60 keV *beams by 2010. Picture from [39].*

angles, in order to create a complete set of equations such that every tensor rank can be solved for. Similarly to the problem of flipping the foil angle mentioned in Sec. 2.3, measuring with several experimental configurations may alter the efficiency factors, or in this case the analyzing powers, so this method should be used with care.

2.5 ISOLDE

The ISOLDE [37] facility at CERN is at the forefront of ISotope OnLine (ISOL) separator facilities. Since the start of operation in 1967, pure beams of more than 700 isotopes from over 70 of the chemical elements have been produced [38]. The beams have been delivered with currents up to 10^{10} ions/s accelerated with a static electric potential of up to 60 kV. The available isotopes and yields over the nuclear chart can be seen in Fig. 2.16. The flexible design of the facility allows for a wide range of beam energies and experiments, from eV for decay studies, mass spectrometry, laser spectroscopy, solid-state- and bio-physics, up to MeV/u for Coulomb excitation and nucleon transfer experiments. A simple layout of the facility is shown in Fig. 2.17.

At ISOL facilities, exotic nuclei with life-times down to around 10 ms can be produced and delivered to experiments. The primary nuclei are produced from spallation, fission or fragmentation reactions in a thick target bom-

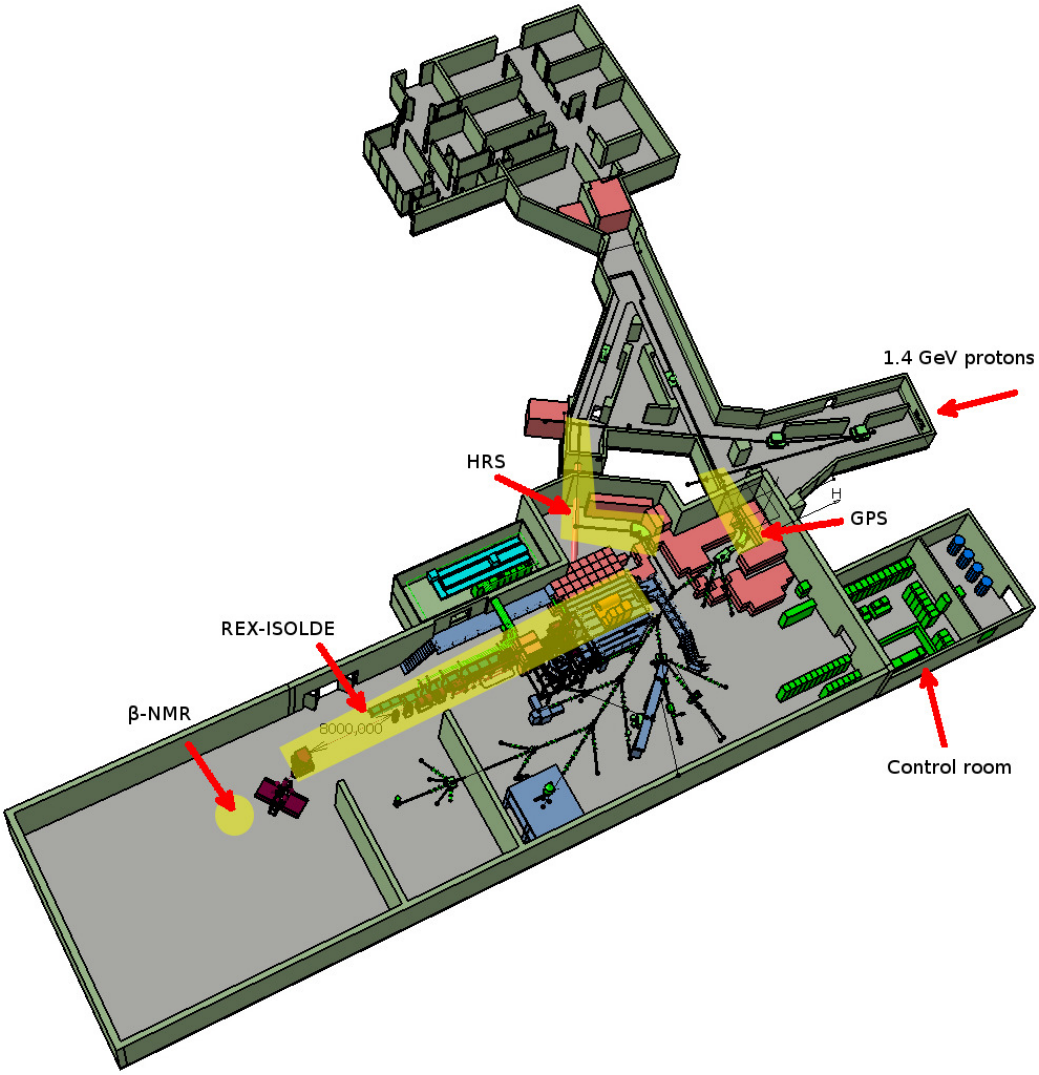

Figure 2.17: Schematic overview of the ISOLDE hall. High-energy beams are available only after the REX-ISOLDE linac, the remaining space is devoted to low-energy beams. From [39].

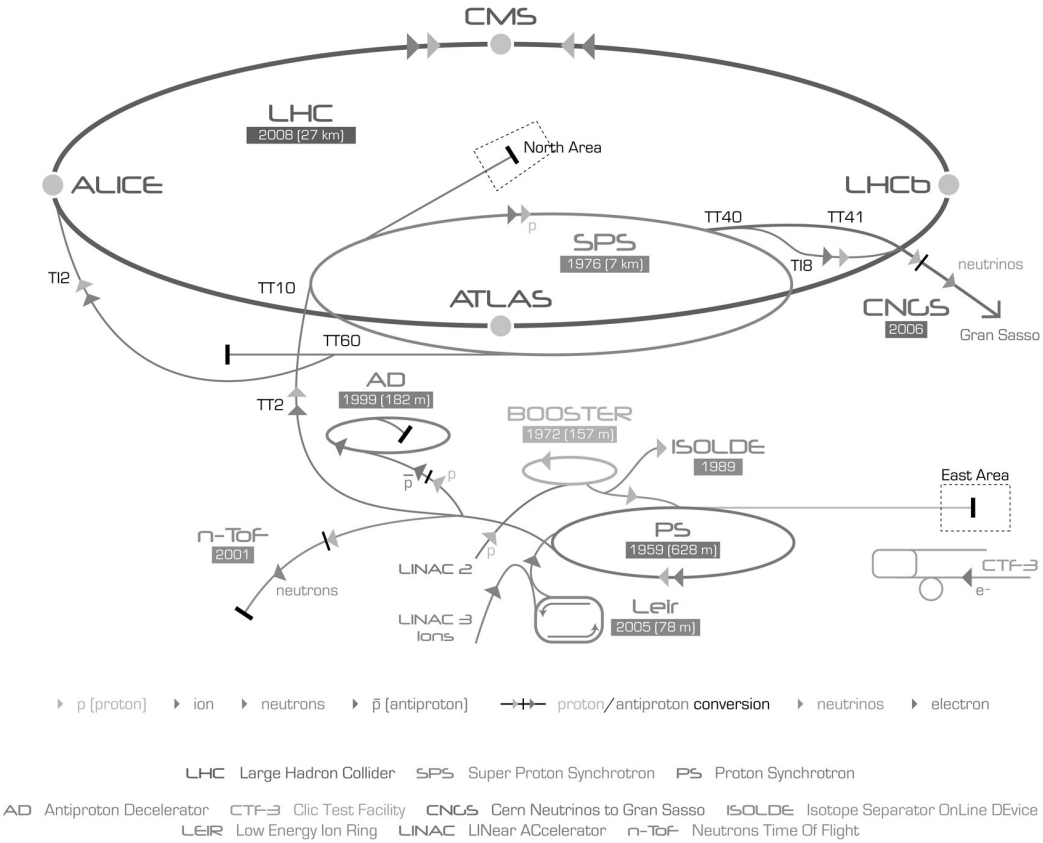

Figure 2.18: The CERN accelerator complex. Note that ISOLDE has been upgraded several times and the picture denotes the year when ISOLDE was relocated to a new experimental hall and fed by protons from the PS Booster. Picture from [40].

barded with high-intensity beams of high-energy light particles. In the case of ISOLDE, the light particles are protons provided by the *PS Booster*, the first circular accelerator of the proton infrastructure at CERN, see Fig. 2.18. The protons are injected from *LINAC2* at an energy of 50 MeV and accelerated in the PS Booster up to an energy of 1.4 GeV and are ejected in pulses of up to 3×10^{13} protons every 1.2 s. Each pulse can be directed to one of several experimental sites or consecutive accelerators at CERN in a periodic pattern called the *super-cycle*. At full intensity, the ISOLDE target receives a current of approximately 2 µA of protons during one super-cycle.

The protons impinge on one of two targets at ISOLDE. One of the targets is followed up by the *GPS* (General Purpose Separator) and the other by the *HRS* (High Resolution Separator) dual mass separator magnets. To ensure fast extraction of the produced radioactive isotopes, the targets are generally porous and heated electrically to between approximately 2000 and 2500 K for

fast diffusion. The atoms effuse towards a transfer line, often heated, and are ionized with one of three techniques. In *surface ionization*, the transfer line is heated to up to 2400 K and atoms with a low ionization potential, typically less than 6.5 eV [41], are ionized on contact. In the *FEBIAD* (Forced Electron Beam Induced Arc Discharge) source types [42, 43], the atoms enter a contained plasma, created by electrons accelerated by a voltage of 150 V, and the atoms are ionized be several processes including collisions with the electrons and surface ionization. In *laser ionization*, provided by the *RILIS* (Resonance Ionization Laser Ion Source) setup, the atoms are ionized by two- or three-step excitation with a laser from a laser beam overlapping the flow of atoms out from the target. With this method, the ionization is specific to the atom of interest and acts as an additional filter to the mass separator.

Next, the ions are accelerated by an electrostatic field of 30-60 kV and enter magnetic dipole mass separators. Charged particles in dipole magnetic fields follow circular trajectories determined by the A/q ratio so that contamination can be filtered out by blocking undesired trajectories with mass slits in the focal plane. As the resolution is not sufficient to resolve nuclides within an isobar, some isobaric contamination may overlap the beam of interest in certain cases. At this stage, the beam consists mainly of singly-ionized ions from one isobar that can be distributed to several places in the ISOLDE experimental hall.

2.5.1 REX-ISOLDE

Experiments in the low-energy domain were the focus of ISOLDE operation for approximately 30 years and is still crucial. In 1994, the linear accelerator REX-ISOLDE was proposed for post-acceleration of ISOLDE beams and it became operational in 2001. The accelerating cavities occupy a length of 10 m and have successfully accelerated more than 100 radioactive isotopes up to energies of 3.0 MeV/u with good experimental yields [39]. The following sections treat the major components involved in preparing singly ionized low-energy radioactive beams for post-acceleration to intermediate energies for experiments, a stage illustrated in Fig. 2.19.

Cooling and bunching in REXTRAP

Following single ionization and extraction from the online ion source, the beam has a high emittance and a cw beam structure, which makes injection into a charge breeder inefficient. Therefore, the beam is cooled in the REX-TRAP Penning trap [45]. A pulsed electrostatic potential combined with a static magnetic solenoid field are used to confine the trapped ions, while

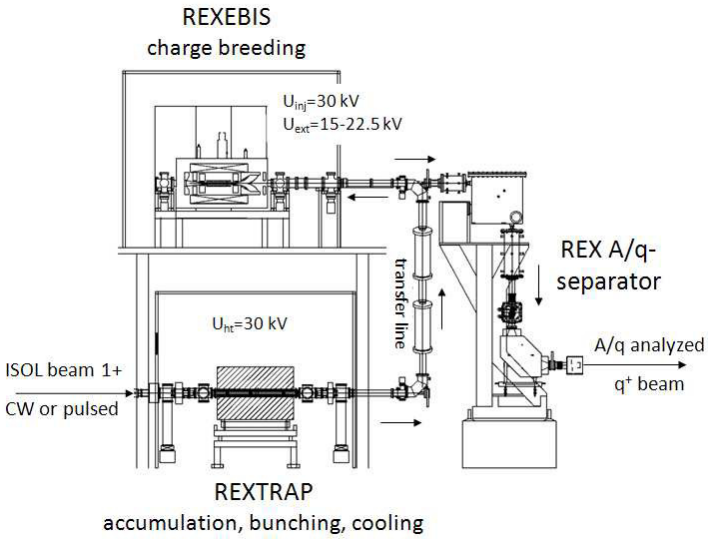

Figure 2.19: Schematic drawing of the REX-ISOLDE ion preparation stage with REXTRAP and REXEBIS. REXTRAP cools and bunches the beam from the ISOLDE ion sources before injection into REXEBIS which strips atomic electrons away with a high-energy electron beam to a mass-to-charge ratio of $2.5 < A/q < 4.5$. *The charge bred ions are then separated and injected into the post-accelerating linac. Picture from [44].*

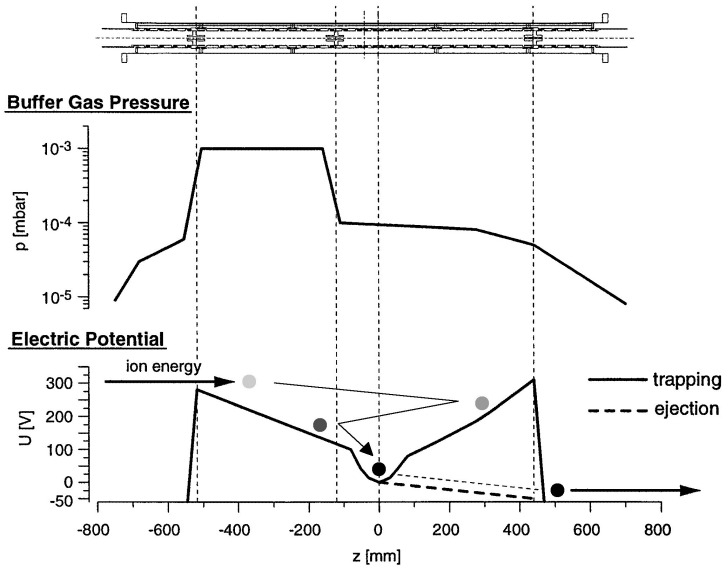

Figure 2.20: Illustration of the buffer gas pressure and electric trapping potential in REXTRAP. In the electric potential diagram, the solid line describes the trapping potential and the dashed line the potential at ejection of the cooled ions. No change to the electric potential is necessary during injection, since the buffer gas will immediately cool the ions to energies below the entry potential. The magnetic trapping field surrounds the cylindrically cavity. Modified from [45].

an inert buffer gas cools the ions. The electrical confinement field and the buffer gas are schematically illustrated in Fig. 2.20. The electric potential decelerates the ions into a trapping region with an axially quadratic potential well, whereas the static magnetic field constrains the radial movement of the ions. The inert buffer gas, Ar or Ne, cools down the ions via energy dissipation from collisions. After some 20 ms, or longer if the breeding time so requires, the stopping electric field at the exit side of the trap is rapidly lowered. The ions can therefore escape the trap in a bunch, with a temporal width of one bunch being approximately 10 µs to 50 µs. At the exit, the ions are re-accelerated to 30 keV and travel to REXEBIS for charge breeding.

Charge breeding in REXEBIS

The accelerating cavities in the linac increase the beam energy by employing radio frequency (RF) fields interacting with the charge of the ions. Singly charged ions present a large mass-to-charge ratio (A/q) which requires a high accelerating voltage, resulting in a long accelerator for adequate acceleration. To avoid this, the solution implemented at REX-ISOLDE is to decrease the

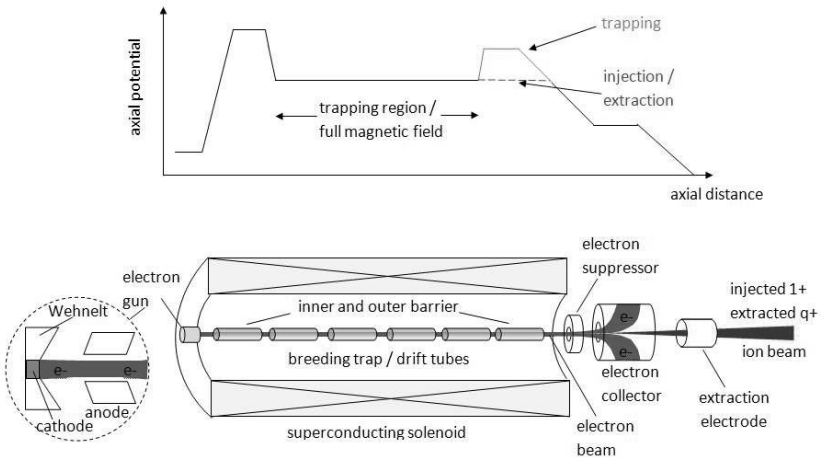

Figure 2.21: Illustration of key components inside REXEBIS, such as the trapping magnetic field and the electron beam. The solid line in the electric potential diagram shows the trapping operation, the dashed line shows the profile during injection and extraction. From [44].

A/q by charge breeding before the acceleration stages. REXEBIS [44] has successfully produced many beams with A/q between 2.5 and 4.5. Internally, REXEBIS has a design similar to REXTRAP, but the buffer gas is replaced with an electron beam operating in an Ultra High Vacuum (UHV) of at least 10^{-11} mbar, see Fig. 2.21. The electron gun shoots a high intensity beam of highly energetic electrons onto the trapped ions which strips away atomic electrons from the trapped ions. After charge-breeding, the ions are ejected by lowering the trapping field. The time for breeding varies from a few ms for light elements up to several 100 ms for heavy ions. The extraction ions then enter a mass separator which selects the desired A/q, and are transported to the linac cavity and beam focusing elements.

It should be noted that REXEBIS may run in offline mode without beams delivered by the ISOLDE separators by injecting gas directly into REXEBIS and therein producing the highly charged ions. This is especially useful for stable isotopes in order to provide an easily controllable high intensity beam.

Accelerating cavities and beam focusing

The REX-ISOLDE accelerating cavities [46] operate with RF fields. The acceleration is performed step-wise by six separate devices: the RFQ (Radio-Frequency Quadrupole), IHS (Interdigital H-type Structure), three so-called 7-gap and one 9-gap resonator. The RFQ is a 4-rod rf-cavity quadrupole designed specifically to bunch, accelerate and focus low-energy beams. This

device is used in many other RIB facilities as an early acceleration stage. The IHS is a simpler device and only performs acceleration via RF fields parallel and anti-parallel to the beam axis. The 7-gap and 9-gap cavities are IH structures and work similarly to the IHS.

The acceleration energy of this linac cannot be configured with continuous resolution over the full energy range, but a fixed set of energies can be attained by enabling selected cavities. The lowest and highest possible beam energies are currently 298 keV/u and 3.0 MeV/u, respectively. During transport between the cavities and up to experimental setups, pairs or triplets of quadrupole magnets in alternating focusing and defocusing orientation around the beam provide a total focusing of the accelerated ions.

Chapter 3

^{21}Ne particle-scattering experiment

Before the lengthy assembly of the β-NMR setup at REX-ISOLDE had been completed, alternative polarization measurement experiments were considered. The particle scattering technique could be realized with the Miniball γ-spectrometer [47], a resident experimental setup in the ISOLDE hall aimed mainly at Coulomb excitation and transfer experiments. This approach was evaluated using an off-line beam of stable ^{21}Ne ($I = 3/2^+$) impinging on ^{120}Sn ($I = 0$) at an energy of 2.85 MeV/u. A small foil tilting device was installed in a diagnostics box approximately 1 m upstreams of the Miniball beam-line. The experimental setup and results are presented in this chapter.

3.1 ISOLDE and REX-ISOLDE setup

The experiment aimed at evaluating the degree of nuclear spin polarization by measuring the asymmetry in the angular distribution of scattered particles which undergo Coulomb excitation. The major components of the experiment were REX-ISOLDE which delivered the accelerated particles, the tilted foils device for creating the polarization and the Miniball γ-spectrometer with the T-REX particle detector setup [47] for measurement. The full setup is schematically illustrated in Fig. 3.1.

Because this experiment was designed exclusively for measuring nuclear spin polarization, stable ^{21}Ne was chosen to obtain an intense beam with constant intensity. This was needed to satisfy the statistics requirement for this counting experiment, taking into account the relatively low cross-section for Coulomb excitation in the order of 1 mb. Since ^{21}Ne is a stable isotope, it was injected directly into the EBIS from a gas bottle, rather than

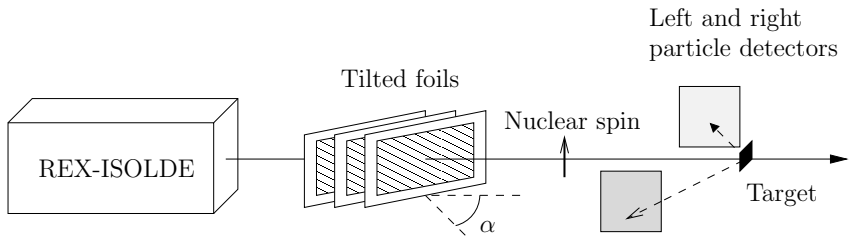

Figure 3.1: Overview of the ^{21}Ne experiment. Two foil stacks were prepared with two and three foils each with variable tilting angle, but only the three-foil stack was used because of the low event rate. The particle detectors were positioned to detect backwards scattering due to the lower cross-section for elastic scattering in this angular range.

being produced online by ISOLDE. This provided an easily adjustable and reliable beam current of approximately 200 e pA which is at least an order of magnitude higher than the nominal radioactive beam current [48]. Also, this isotope has a relatively high ground-state spin of $3/2^+$ compared to other stable light nuclei which makes it suitable to achieve high degrees of nuclear polarization as explained in Sec. 2.2.2. The first few excited states and transitions are listed in Tab. 3.1. Note the wide energy gaps between observable high-intensity transitions, which simplifies detection and analysis of γ-radiation. The charge state selection in the REX linac was set to $q = +5$ corresponding to an $A/q = 4.2$ which separates the beam from most common contaminants of REX. The beam energy was set to 2.85 MeV/u to achieve a high Coulomb excitation cross section and good beam transmission. This is in conflict with the low velocity beams normally favored for tilted foils polarization, but Coulomb excitation cross sections decrease rapidly with energy and statistics would have suffered significantly.

At $q = +5$, the electron configuration of ^{21}Ne is $1s^2 2s^2 2p^1$, with $^2P_{1/2}$ configuration and the atomic spin $J = 1/2$. If this was the charge state at foil exit, $I > J$ and any spin polarization of the nucleus can be expected to be able to attain values larger than that of the atomic spin.

The Coulomb excitation target was ^{120}Sn, which has a first excited state at a higher energy than that of ^{21}Ne (refer to Tab. 3.1 and Tab. 3.2). It is also an even-even nucleus which simplifies the effect of polarization in the observed reaction channels as covered in Sec. 2.4.1. Results show that the amount of de-excitation from the target is negligible compared to the amount of de-excitation from the projectiles. Therefore, all observed Coulomb excitation reactions can be assumed to leave the target nuclei in the 0^+ ground state.

Table 3.1: First excited states and intense transitions of ^{21}Ne. From [49].

E (keV)	J^π	$\tau_{1/2}$
0	$3/2^+$	stable
350.727(8)	$5/2^+$	7.13(14)ps
1745.911(18)	$7/2^+$	52(3)fs

ΔE (keV)	Mult.	B(E2) (W.u)
350.7	M1+E2	0.0716(15), 24(3)
1395.1	M1+E2	0.145(9), 11(4)

Table 3.2: First excited states and intense transitions of ^{120}Sn. From [49].

E (keV)	J^π	$\tau_{1/2}$
0	0^+	stable
1171.265(15)	2^+	0.640(12)ps
1875.108(25)	0^+	7.4(10)fs

ΔE (keV)	Mult.	B(E2) (W.u)
703.84(2)	E2	12.6(17)
1171.25(2)	E2	11.41(22)

3.2 Tilted-foils device

To reduce the effects of the tilted foils on the beam, the foils were kept as thin as possible. For this experiment, self-supporting pure diamond-like carbon (DLC) foils with a thickness of $4\,\mu g/cm^2$ and a surface area of approximately $5\,cm^2$ were used.

The setup holding the thin tilted foils was designed and manufactured as a general purpose device and was easily integrated into the beam-line approximately 1 m upstream of the Coulomb excitation setup [50], see Fig. 3.2. A stepper motor allowed to control the tilting angle of the foils remotely during the experiment, although care should be taken for the different geometric configurations created for different foil angles.

The holder was designed with three windows in order to allow switching between three foil configurations without the need to break the beam-line vacuum. This was useful to monitor potential scattering on frames without foils and to shoot the beam through different numbers of foils. For this experiment, an empty frame was installed in the top window for reference measurements, one foil in the middle window and three foils in the bottom window. Fig. 3.3 shows the loaded foil holder prior to the experimental

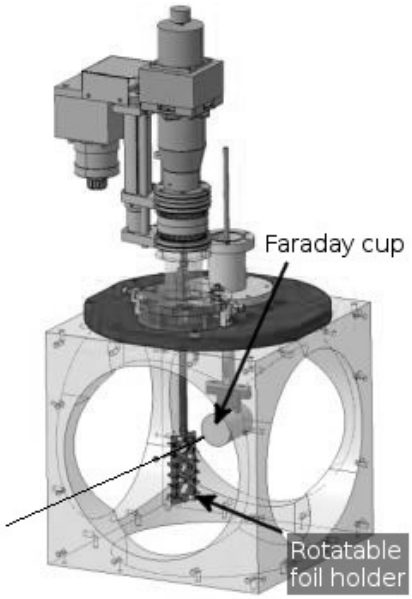

Figure 3.2: Schematic view of the foil holder and tilting mechanism, installed 1 m *upstream of the target chamber in the Miniball experimental setup. The line entering the diagnostics box represents the beam passing through the foils. From [50].*

run. The distance between the three foils in the bottom window was 1 mm, which with a tilting angle of 70° which corresponds to almost 3 mm effective spacing.

The programming interface for changing the foil angle consisted of a custom high-level scripting language designed specifically for the stepper driver. It was sufficiently versatile to allow for fine tuning of motor speed and acceleration to reduce mechanical vibrations that may put mechanical stresses on the fragile foils. To further reduce the vibrations, the current in the stepper driver was reduced via DIP (Dual In-line Package) switches inside the driver from 1 A to the lowest possible 0.5 A. The actual program can be found in [50] and it performed the following sequence repeatedly:

- Orient foils at $-70°$ and wait for 3 min.
- Orient foils perpendicularly to the beam and wait for 30 s.
- Orient foils at $+70°$ and wait for 3 min.

The actual reorientation from 0° to $\pm 70°$ took around 10 s.

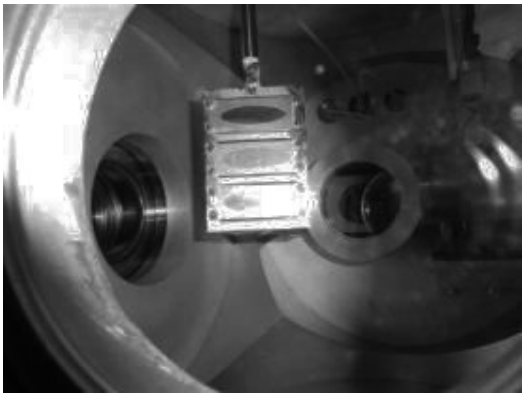

Figure 3.3: Foil holder loaded with foils. The top window contains an empty frame for beam diagnostics purposes, the middle window one foil and the bottom window three foils. From [50].

3.3 Miniball

Miniball [47], schematically depicted in Fig. 3.4, is a γ-spectrometer located behind REX-ISOLDE. Due to the expected low beam intensities from ISOLDE leading to a small number of reactions of interest, high detection efficiency was emphasized. High angular resolution is also important to obtain accurate angular correlations between particles and γ-rays in order to reduce artifacts such as Doppler shift in γ-spectra.

There are eight triplet clusters of HPGe (High Purity Germanium) crystals in the Miniball setup. Every triplet is cooled with cold fingers at liquid nitrogen temperature, and each crystal is segmented into six symmetric parts, making for a total of $8 \times 3 \times 6 = 144$ active segments for high angular resolution. It is also possible to perform pulse-shape analysis to find the position inside the crystals to increase the angular resolution by a factor three [51]. This requires additional analysis and is typically only used for experiments which demand the utmost possible precision of γ-ray angular distributions. The clusters are mounted on a flexible armature with three rotational degrees of freedom which allows the detectors to be positioned as close as 12 cm from the target and with good angular coverage. When all clusters are installed, the coverage is approximately 60% of the full 4π solid angle. The intrinsic energy resolution of the crystals was 2.3 keV and the intrinsic efficiency was approximately 7 % at $E_\gamma = 1.3$ MeV.

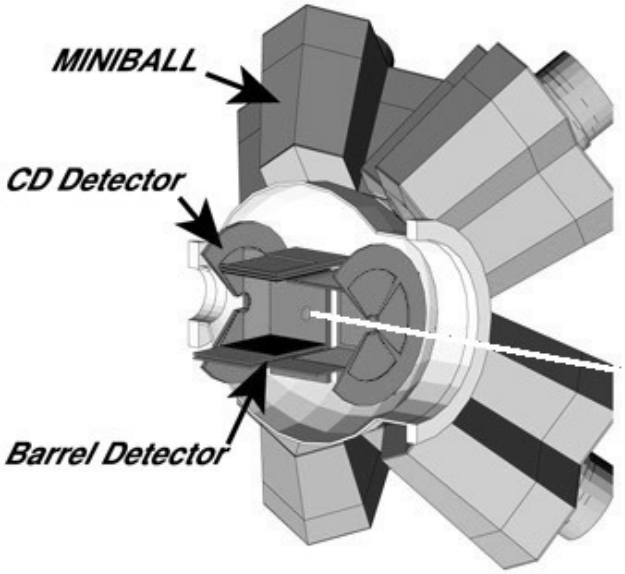

Figure 3.4: Miniball HPGe detectors surrounding the barrel-shaped T-REX particle detector setup. The T-REX detectors consist of several pairs of silicon-detector for $\Delta E - E$ analysis. The white line represents the beam impinging on the target in the middle of T-REX. From [47].

3.3.1 Particle detection with T-REX

The detection of recoil ions after Coulomb excitation is carried out with silicon detectors inside the target chamber. One of the detectors is constructed from concentric arcs of silicon and is called the CD detector, for reasons which should be clear from the photo in Fig. 3.7a. Depending on the experiment, elastic scattering may have a significantly higher cross-section than Coulomb excitation at forward scattering angles. This is especially true for light beams on heavy targets such as in this experiment, in which case the CD detector is mounted upstream from the target for detection only of backwards scattered particles. At these angles, beam ions have undergone collisions with small impact parameters which increases the influence of the Coulomb potential and thus the likelihood of Coulomb excitation. On the other hand, forward scattering is characterized by large impact parameters.

In transfer experiments performed with a heavy ion impinging on a light target, which is the typical inverse kinematics situation when using radioactive beams, the typical maximum in cross-section in the center-of-mass system will be at small angles. In the laboratory system, these angles translate to a wider distribution of scattering angles over $\theta \in [0, \pi]$. For this purpose, the T-REX detector setup [47] was constructed for detecting mainly very

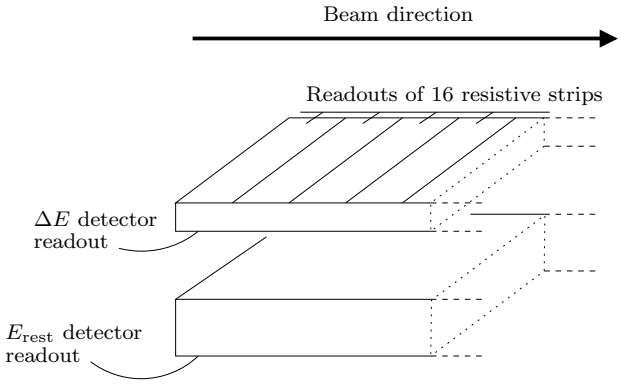

Figure 3.5: Schematic view of the side layers in the T-REX barrel detector. The ΔE and the E_{rest} layers are 150 µm and 1000 µm thick, respectively, and were designed for $\Delta E/E$ identification of light particles (p, d, t and α).

light charged ejectiles, such as protons, deuterons, tritons and α-particles. The setup consists of one CD detector and 8 flat silicon detector-pairs in a barrel configuration, as can be seen in Fig. 3.6 and Fig. 3.7b.

Each flat detector-pair in the T-REX setup consists of two silicon detectors, pictured in Fig. 3.5. The detector that faces the target is approximately 150 µm thick, and the front face is resistive and segmented perpendicularly to the beam direction into 16 strips. The segments allow estimating the deviation angle of from a reaction as $\tilde{\theta}$. Note however that this is not the true deviation angle θ for the barrel detectors. In space, a constant polar angle forms a cone for all azimuthal angles around the beam direction and the projection of such a cone on a flat detector surface is a curved line spanning several strips. The backside of the detector is read out with one signal and can be used together with the resistive strips on the front side to reconstruct the impact point along the strips. The second detector is 1000 µm thick and will stop most particles at the energies involved in Coulomb excitation experiments, thus measuring their residual energy. Together, the two layers can be used to determine the angular coordinates of the charged particles, kinematics curves and the type of particle.

The problem of elastic scattering of the beam previously discussed for the CD detector also applies to the T-REX silicon detectors. Therefore, all detectors located in the forward scattering angles were protected with 12 µm thick Mylar foil. The effects of the radiation damage due to the energy loss of the elastically scattered high-intensity stable beam were noticeable in the reduced efficiency and increased leakage currents in the silicon detectors towards the end of the experiment.

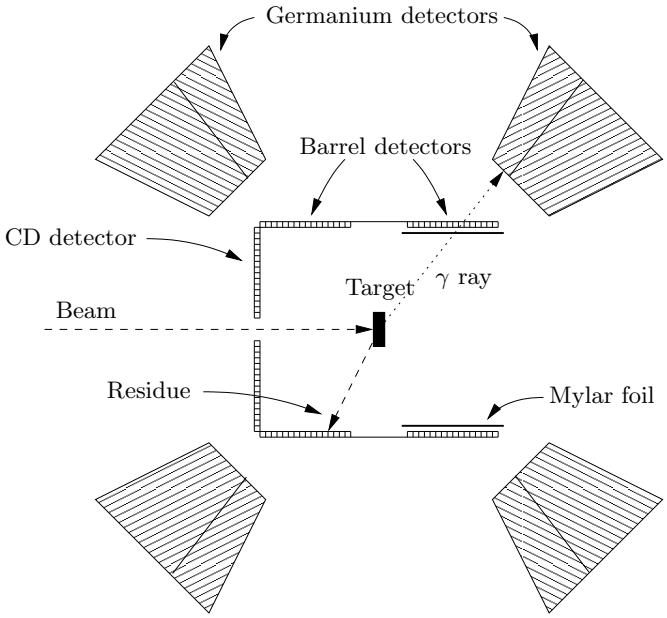

Figure 3.6: Schematic view of the Miniball and T-REX setup detector configuration used for the experiment. The front detectors were covered with 12 µm *thick Mylar foil to protect against high rates of elastically scattered* ^{21}Ne.

3.3.2 Electronics and DAQ

With the digital XIA DGF-4C (Digital Gamma Finder, 4 channels) data acquisition modules [54] at Miniball, it is possible to acquire digitized samples of signals from the HPGe detectors. The additional information for each pulse detected in a HPGe detector can be used for pulse shape analysis (PSA)[51]. By analyzing the shapes of the signals of one event, the impact point inside a crystal can be determined with an angular precision higher than the crystal segmentation. The two major disadvantages coming with this additional precision are that every γ-event allocates much more storage space (a sampled signal rather than a single energy value) and the complexity of the analysis increases manyfold. The full sampled HPGe signal shapes are normally not taken into account [55], but does indeed provide a definite improvement in the peak FWHM [47].

Barrel particle detector signals were collected with MADC32 ADC modules which perform time-stamping of incoming signals. The CD-detector signals were collected with CAEN 785 ADC modules which, due to a lack of time-stamping capability, were timed with a digital trace of the CD-detector trigger signal. All trigger signals were collected and subjected to OR gates at which point all modules were queried by the data acquisition. Data ac-

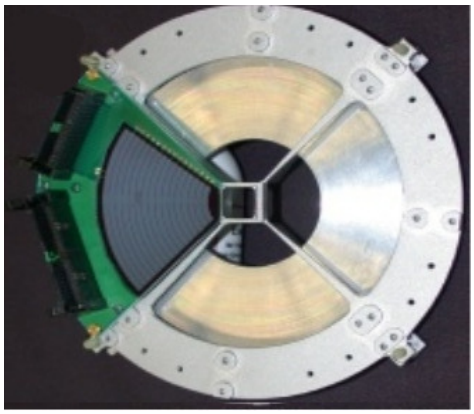

(a) Photo of the annular CD detector, mounted to detect particles scattered in backwards angles. From [47].

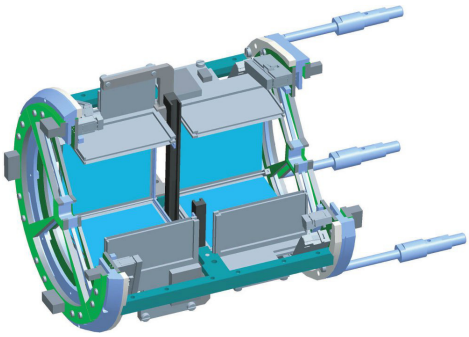

(b) Technical drawing of the T-REX chamber. Normally, one CD detector is mounted on one end of the barrel structure. From [52].

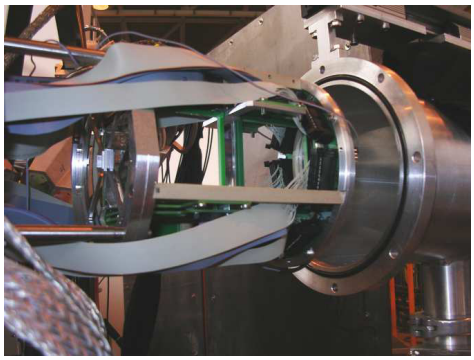

(c) The T-REX chamber installed at the target position. The beam will be delivered from the left side of the picture. From [53].

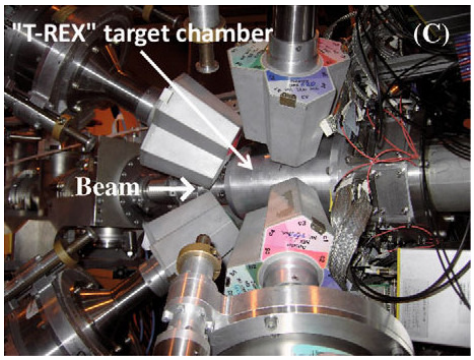

(d) Target chamber closed and surrounded by the HPGe detectors. From [47].

Figure 3.7: Close-up pictures of the T-REX particle detector setup and mounting inside Miniball.

Table 3.3: Signals transmitted by the stepper driver to the Miniball data acquisition for foil orientation status in the event data. The value is a decimal representation of the two binary signals.

Tilting angle	Turning	$-70°$	$0°$	$+70°$
Signal 1	0	1	0	1
Signal 2	0	0	1	1
Value	0	1	2	3

quisition was controlled via MARaBOU [56], based on MBS (Multi-Branch System) [57], which supports online analysis of collected raw and calibrated data. For a more detailed explanation of the Miniball data acquisition system at the time of this experiment, see [58].

3.3.3 Target chamber setup

The ^{21}Ne beam impinged on a self-supporting ^{120}Sn target foil with a thickness of 2.06 mg/cm^2. A ^{60}Ni target with a thickness of 2.0 mg/cm^2 was used first, but due to the low nuclear excitation energies of that nucleus, a large number of background events were recorded, which prompted an early switch to the ^{120}Sn target. A deuterated polyethylene foil was also installed at the target position during parts of the experiment for calibration purposes, which is treated in detail in Sec. 3.5.

The preceding experiment utilized a transfer setup suitable to our needs, including the T-REX setup with Mylar protection against abundant elastic scattering. In the early phases of the experiment, the elastic scattering in the forward T-REX detectors showed very high trigger rates that introduced severe dead time for the full acquisition system. These trigger signals were removed and the system then triggered only on γ-events and backward-scattered particles. Two signals from the stepper driver were connected to an ADC so that the orientation status of the foils was available in the event data stream, see Tab. 3.3.

3.4 Calculations of reaction properties

Ion beams with energies of a few MeV/u reach almost 10 % of the speed of light, which introduces noticeable relativistic effects that need to be taken into account. LISE++ [59] was used to calculate kinematic curves in the lab frame, for example $E(\theta)$ after ^{21}Ne has collided with ^{120}Sn which is shown in Fig. 3.8. This curve is useful for filtering the high-energy neon ions from

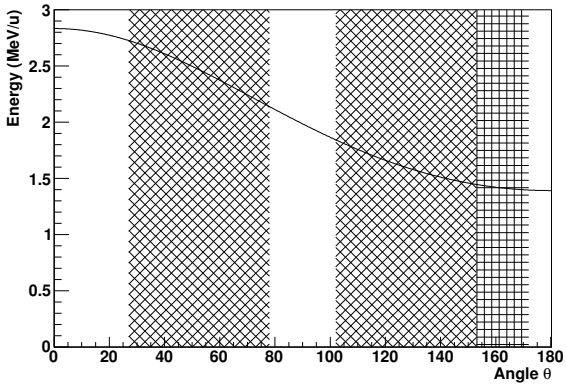

Figure 3.8: Kinematics curves for an inelastic collision between ^{21}Ne, excited to its first excited state at 351 keV*, and ^{120}Sn. The diagonal cross hatches represent the approximate coverage in the lab angle θ by the T-REX barrel detectors and the straight hatches represent the CD detector.*

other detected particles which have different relationships.

3.4.1 Coulomb excitation cross-sections

The FORTRAN program *CLX* [60], provided by the Miniball collaboration, was used to calculate the cross section $d\sigma/d\theta$ for Coulomb excitation of specific nuclear energy levels based on a nuclear transition scheme. The input parameters include beam and target nuclei and energies, nuclear levels and transitions of interest and annular particle detector geometry. Calculations for the first excited level of ^{21}Ne with the T-REX and CD detectors are presented in Fig. 3.9 with data from Tab. 3.4.

As was mentioned earlier, the barrel strips do not perfectly represent polar deviation angles for scattered particles. However, since the cross section data were to be used solely for the comparison of the three main parts of the T-REX particle detectors, the polar angle was chosen to refer to the middle of barrel strips. According to the trend of the cross sections, the total cross section for a strip is slightly overestimated for the backward barrel strips and vice versa for the forward barrel strips. The calculations show differences between the barrel detectors and the backward CD by some orders of magnitude. Therefore, since the backward CD would contribute little in terms of statistics and the three layers of silicon (annular segmented ΔE, radially segmented ΔE and E_{rest}) require a more involved analysis, it was not used in the final analysis.

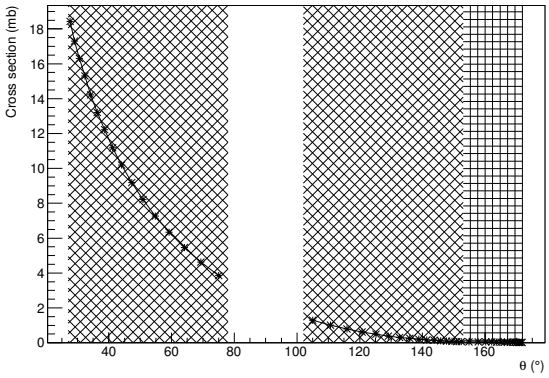

Figure 3.9: Coulomb excitation cross-sections for populating the first excited state of ^{21}Ne, leading to 351 keV *γ-decay, on a ^{120}Sn target as calculated by the CLX program. Banded regions are explained in Fig. 3.8. Data taken from Tab. 3.4.*

Table 3.4: Detection cross-sections for ^{21}Ne Coulomb excited to the first excited state hitting the middle of the strips in the barrel detectors. Note that the values are over- and underestimated for the backward and forward detectors respectively, due to the curvature of constant polar angle from the scattering reaction. For the barrel detectors, strip 0 is closest to the target, strip 15 is the furthest away, and for the CD, 0 is the outermost ring.

Strip	Forward (mb)	Backward (mb)	CD (mb)
0	3.8544	1.2913	0.0468
1	4.6234	1.0089	0.0455
2	5.4532	0.7882	0.0438
3	6.3329	0.6175	0.0429
4	7.2666	0.4860	0.0405
5	8.2139	0.3855	0.0389
6	9.1857	0.3082	0.0371
7	10.1944	0.2475	0.0346
8	11.1747	0.2028	0.0328
9	12.2267	0.1666	0.0308
10	13.2176	0.1371	0.0279
11	14.2238	0.1151	0.0258
12	15.2996	0.0972	0.0235
13	16.3151	0.0821	0.0208
14	17.3039	0.0699	0.0182
15	18.4233	0.0607	0.0155

Table 3.5: Fusion evaporation cross-sections for ^{21}Ne on ^{60}Ni and on ^{120}Sn, calculated with PACE4 in LISE++ [59]. The zero cross-sections for ^{120}Sn means cross-sections smaller than 10^{-20} mb as reported by PACE4, which is not surprising because the beam energy is very close to the safe energy.

Nucleus	Fraction	Cross section (mb)
^{78}Kr	34.8%	132
^{78}Rb	20.2%	76.8
^{75}Br	11.6%	44.2
^{79}Rb	6.40%	24.4
^{76}Kr	6.29%	23.9
^{138}Nd	75.2%	0
^{139}Nd	10.9%	0
^{138}Pr	9.06%	0
^{139}Pr	2.66%	0
^{135}Ce	1.07%	0

Fusion evaporation cross-sections

Fusion evaporation cross-sections of ^{21}Ne + ^{60}Ni and ^{21}Ne + ^{120}Sn reactions were calculated using PACE4 in LISE++ [59], and are given in Tab. 3.5. The nickel target was included for comparison, and it turned out that ^{120}Sn was the considerably better target for the experiment. The data confirms that fusion evaporation should yield events of almost the same amount of statistics as Coulomb excitation in the γ-spectra with ^{60}Ni, whereas the signal to noise ratio with ^{120}Sn is much better. According to Eq. 2.45, the integrated safe energy for ^{60}Ni is 1.94 MeV/u and for ^{120}Sn 2.76 MeV/u, with the latter being close to the full beam energy of 2.85 MeV/u.

Energy losses and spread in the target

Due to the 7.12 ps half-life of the first excited state of ^{21}Ne, the position when de-excitation occurs should be anywhere inside or very close to the target. The excited nuclei therefore have kinetic energies below the beam energy of 2.85 MeV/u. The full energy range goes from 2.845 MeV/u due to losses in the tilted carbon foils down to 0.72 MeV/u when an ion is subjected to Coulomb excitation at the end of the target and thus traverses the target twice before being detected in the backward hemisphere of the setup. This uncertainty in energy for the residue particles broadened the kinematic curves significantly. It was therefore difficult to perform particle identification based on kinematics and energy.

3.5 Detector calibration

3.5.1 Energy calibration

Calibration parameters for online analysis were kept from the experiment preceding the ^{21}Ne experiment. The γ-detectors had been calibrated with stationary radioactive sources ^{152}Eu and ^{60}Co, and the particle detectors with a mixed α source consisting of four isotopes: ^{148}Gd, ^{239}Pu, ^{241}Am and ^{244}Cm with the α-energies 3.18 MeV, 5.16 MeV, 5.49 MeV and 5.81 MeV, respectively. Least squares linear fits were performed for every detector to obtain linear calibration curves. Fitting with higher order terms was tested but did not improve the calibration significantly in the energy region of interest (up to 2 MeV). To increase the final calibration statistics, strong peaks in the experimental data were also used for calibration during the offline analysis.

3.5.2 Doppler correction

The beam energies used in the experiment cause relativistic Doppler shift broadening of de-excitation γ-radiation peaks. The correct γ-energy E_0 in the emitter frame can be calculated with

$$E_0 = E_\gamma \gamma \, (1 - \beta \cos\theta), \tag{3.1}$$

where E_γ is the observed γ-energy, γ and β are the relativistic parameters of the emitter and θ is the angle between the momentum vector of the emitting nucleus and the direction of observation. The values for γ and β are estimated from the beam energy and the angle θ was determined from angular detector coordinates.

This relatively simple expression is not only used to Doppler-correct γ-spectra, but can help calibrating the experimental setup. By fixing the beam energy which relates to β and γ and using a reaction with well known kinematic curves, it is possible to extract θ from Eq. 3.1 and solve for the θ angles of the γ-detectors. This is treated in more detail next.

3.5.3 Position of the HPGe γ-detectors

As was briefly mentioned in the previous section, it is possible to estimate the polar angle θ of the Miniball γ-detectors based on data from a reaction with well known kinematics. At Miniball, the ^{22}Ne(d,p)^{23}Ne transfer reaction, with stable ^{22}Ne ions impinging on a deuterated polyethylene target, is regularly used to calibrate the exact position of the γ-detectors. This approach gives higher angular precision than reading coordinates from the

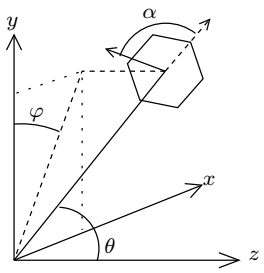

Figure 3.10: Illustration of the polar angles θ and φ that define the position of a HPGe detector cluster and the angle α that defines the cluster roll. The z axis points in the direction of the beam.

detectors armature and circumvents mechanical errors. The deviation of the beam ejectile is in the order of 5° which can be approximated with a zero deviation, and Doppler broadening is very small because of the small energy losses in the light target. The reaction ^{21}Ne(d,p)^{22}Ne was used instead of the ^{22}Ne(d,p)^{23}Ne reaction, because they have similar characteristics and allowed to leave the beam setup unchanged for this experiment. The most prominent peak of decaying ^{22}Ne was the E2-transition 1274.577(7) keV with $B(\mathrm{E2}) = 12.5(5)$ W.u..

Due to the rigid geometric relationship between segments in a detector-cluster, given rough estimates and taking into account possible geometrical symmetries, all three angular coordinates, as illustrated in Fig. 3.10, can be extracted. The three angular coordinates of a cluster were adjusted iteratively by a custom written program and the Doppler correction for a set of coordinates was used to evaluate the calibration quality to find an optimal set of angular coordinates. This optimization problem presents a complex parameter space for a single correct solution, so human intervention was required for updating parameters rather than doing so automatically.

In principle, it is possible to reconstruct the small residue angle of the outgoing ^{22}Ne by observing the proton. The deviation angles of the ejectile and residue are related, as shown in Fig. 3.11. Using this kinematics curve $\theta_{(^{22}Ne)}(\theta_p)$, the angle θ in Eq. 3.1 between the ^{22}Ne and the γ-rays can be calculated exactly. The correction is very small in this calibration, but may be of use in experiments which demand very accurate Doppler correction for larger residue deviation angles. Most counting experiments can be designed such that resolving of γ-peaks is not crucial, as is the case with this polarization measurement experiment. Other approximations in the analysis, such as point-like detectors and simplifications of energy losses in the target, may contribute further to Doppler broadening.

Results from the Doppler correction of the ^{21}Ne(d,p)^{22}Ne calibration runs

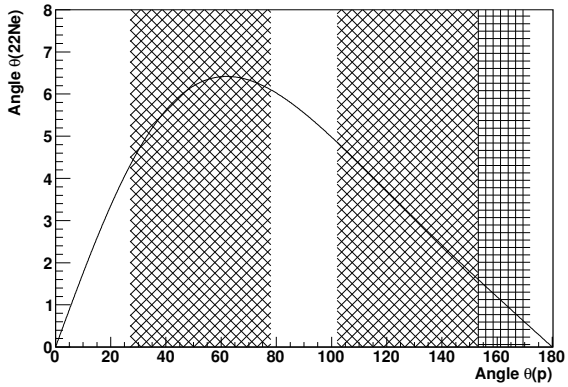

Figure 3.11: Kinematics curve between θ_p and $\theta_{^{22}\mathrm{Ne}}$ for $^{21}Ne(d,p)^{22}Ne$ reaction. Banded regions are explained in the caption of Fig. 3.8.

are presented in Fig. 3.12 for specific detectors and segments, and the sum of all detectors is presented in Fig. 3.13.

3.5.4 T-REX

Position information along the strips in the silicon detectors (see Fig. 3.14) can be obtained with

$$x = C\frac{E_{\mathrm{resistive}}}{\Delta E}, \tag{3.2}$$

where x is the position such that $x = 1$ is at the readout end and $x = 0$ is at the other end of the strip, $E_{\mathrm{resistive}}$ is the readout from the resistive layer for the strip, ΔE is the readout on the rear side of the same silicon detector slab and C is a calibration coefficient. An example of a calibration can be seen in Fig. 3.15. The small slope in the signals is due to the small inherent resistivity in the back readout of the ΔE detector and is normally accounted for by a horizontal fit with [53]

$$E_{corr} = \frac{E(x)}{a(1-x)+1} \tag{3.3}$$

$$a = \left[\frac{E(x)}{E(x=1)} - 1\right]\frac{1}{1-x}. \tag{3.4}$$

The full calibration to correct for the position dependence was not carried out due to problems with the collected data which will be covered in the discussion section.

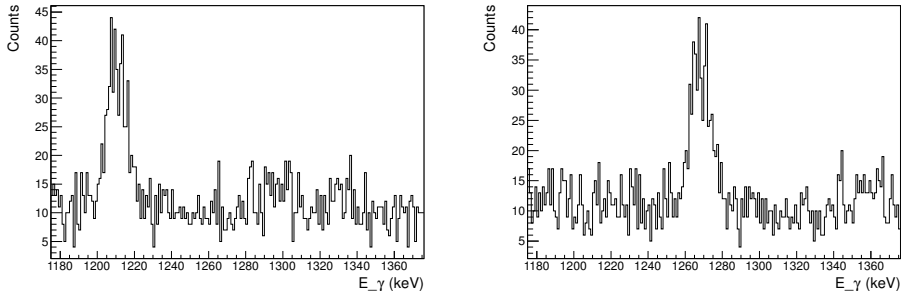

(a) Not corrected $(0, A, 0)$. *(b) Doppler corrected* $(0, A, 0)$.

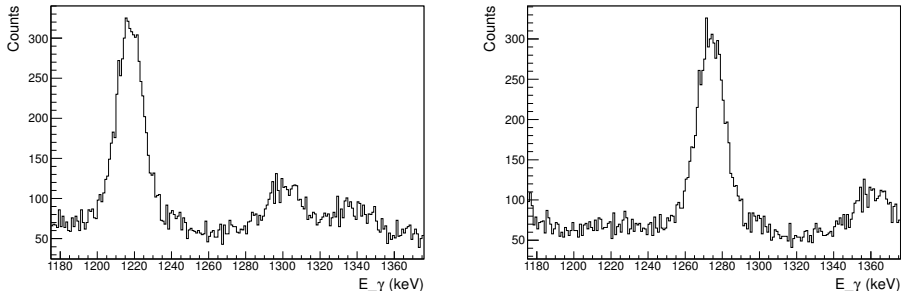

(c) Not corrected $(0, A, \text{core})$. *(d) Doppler corrected* $(0, A, \text{core})$.

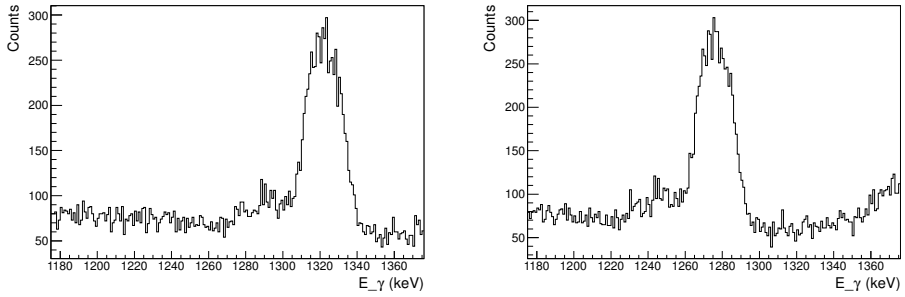

(e) Not corrected $(1, A, \text{core})$. *(f) Doppler corrected* $(1, A, \text{core})$.

Figure 3.12: Position-calibrated and Doppler-corrected γ-spectra of a germanium segment and two cores from the $^{21}Ne(d,p)^{22}Ne$ reaction runs. The parentheses notation means (cluster $\in \{0..7\}$, crystal $\in \{A, B, C\}$, segment $\in \{\text{core}, 0..5\}$). Note that clusters 0 and 1 detected γ-radiation in the backwards and forwards angles, respectively. The detector optimization aimed at centering the peak at $1275\,\text{keV}$, the most prominent peak from excited ^{22}Ne after a one-nucleon transfer. The peaks can be narrowed further if the small deviation angle of the residue ^{22}Ne is reconstructed, but these spectra are used for angular coordinate calibration of the HPGe detectors, not the energy values.

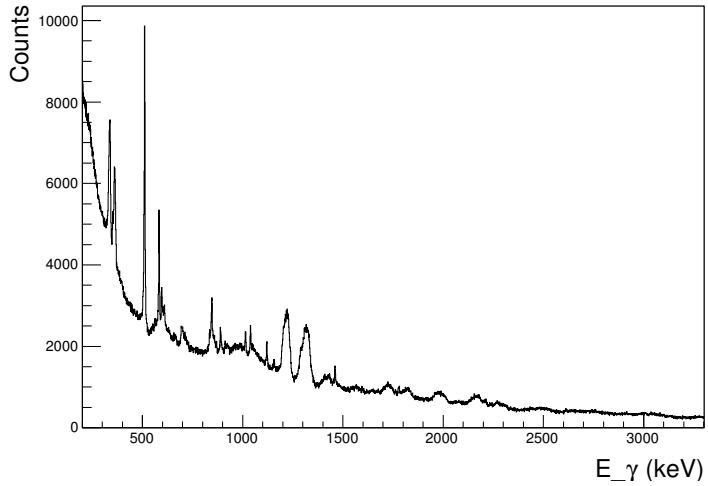

(a) Not Doppler corrected.

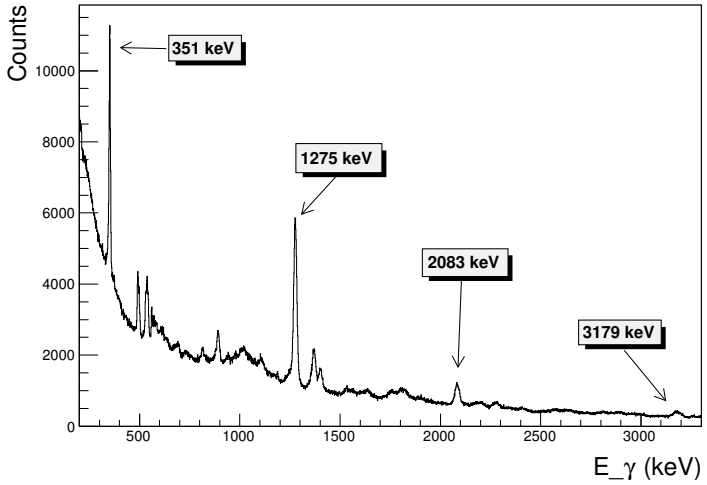

(b) Doppler corrected.

Figure 3.13: Energy calibrated γ-spectra from the $^{21}Ne(d,p)^{22}Ne$ reaction runs. Energies are taken from the germanium cores and the segments are used for the angular position. Notice that by optimizing Doppler correction for the first excited state in ^{22}Ne at 1274 keV, three other peaks are corrected; the first excited state of ^{21}Ne at 351 keV and transitions from the second and third excited states of ^{22}Ne at 2083 keV and 3179 keV. High γ-ray energies were not calibrated which may be the cause of the large width of the high energy peaks. The sharp positron electron annihilation line at 511 keV is destroyed by the Doppler correction.

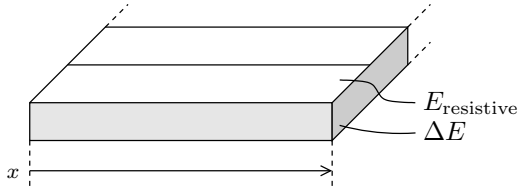

Figure 3.14: The position-dependent signal $E_{\text{resistive}}$ in the resistive strip together with the position-independent readout ΔE can be used to determine the position x of a detected charged particle according to Eq. 3.2.

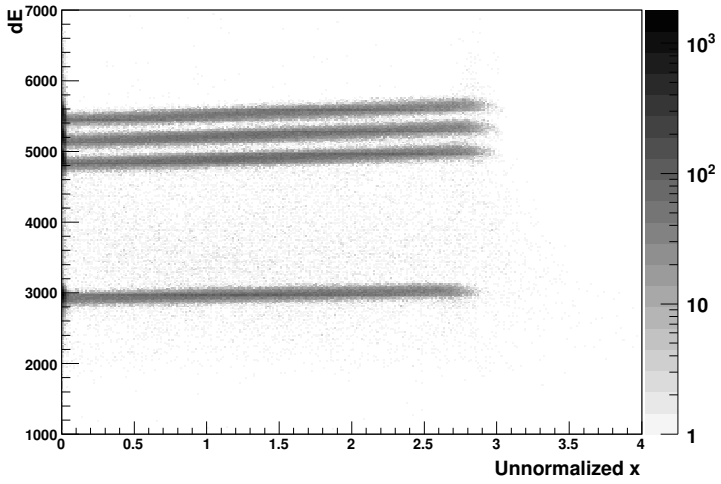

Figure 3.15: Position calibration of silicon strips with a mixed alpha source. The dependence on the detection position in the back-side ΔE-detector has not been accounted for.

3.6 Event selection

The prompt time peak gating between γ and particle observations was set to $|t_p - t_\gamma + t_{\text{off}}| < 100\,\text{ns}$, where t_p and t_γ are the time stamps for a particle and a γ-ray respectively, and $t_{\text{off}} = 150\,\text{ns}$ is a correction term due to a non-zero time-stamp offset between the modules for γ- and particle-detectors. The prompt gate was verified for both targets, ^{60}Ni and ^{120}Sn.

The gating condition on the detected γ-rays for the excited ^{21}Ne consists of keeping events with a γ-line at 350.7 keV. The effective width of the Doppler-corrected 350.7 keV γ-line was determined to be 20 keV.

Kinematics particle selection using the curve in Fig. 3.8 was difficult to perform due to energy losses in the target, which is covered in Sec. 3.7. Instead, because ^{21}Ne nuclei with energies up to 2.85 MeV/u were the most energetic particle in the reactions, a lower threshold at 6 MeV was introduced to remove random coincidences. The value was found by increasing the threshold from zero until the integral of the 350.7 keV γ-line over the signal baseline started to decrease.

3.7 Measurements

In total, after event selection, a little more than 1200 events remained. Energy calibrated γ-spectra without Doppler correction for both ^{60}Ni and ^{120}Sn targets are shown in Fig. 3.16.

Due to protective foils and large amount of elastically scattered ^{21}Ne, data from the detectors in the forward part of T-REX are not presented. The ejectiles did not pass through the ΔE detectors in the backward angles, so analysis of the thick E_{rest} detectors in the backward angles could not be performed. This prevented E vs ΔE plots for particle identification. Finally, the reaction cross-section for the angles covered by the CD detector is orders of magnitude smaller than for the angles covered by the T-REX detectors, so final analysis was not performed for this detector.

Cross-talk histograms between the strips of the resistive layer in the ΔE detectors are presented in Fig. 3.17, showing no discernible cross-talk between adjacent strips. Thus, the polar angle from strip identification should be reliable. Fig. 3.18 presents the correlation plot of ΔE against $E_{\text{resistive}}$, showing a problem of saturation for high energy particles. This hindered length-wise strip coordinate reconstruction which could have increased the precision in the kinematics calculations. Particularly Doppler correction and $\Delta E(\theta)$ particle filtering suffered from this issue.

Correlations between ΔE and deviation angle with a gate around the first

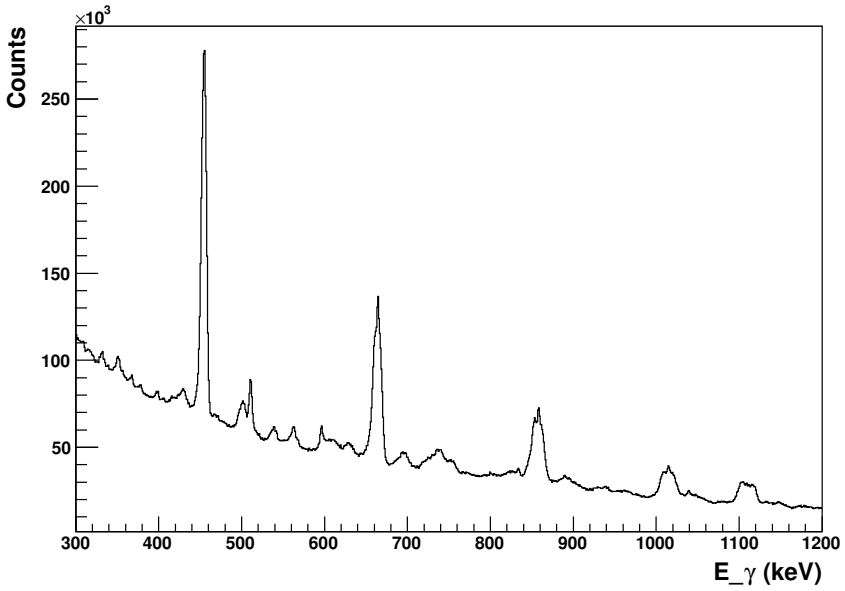

(a) ^{60}Ni target.

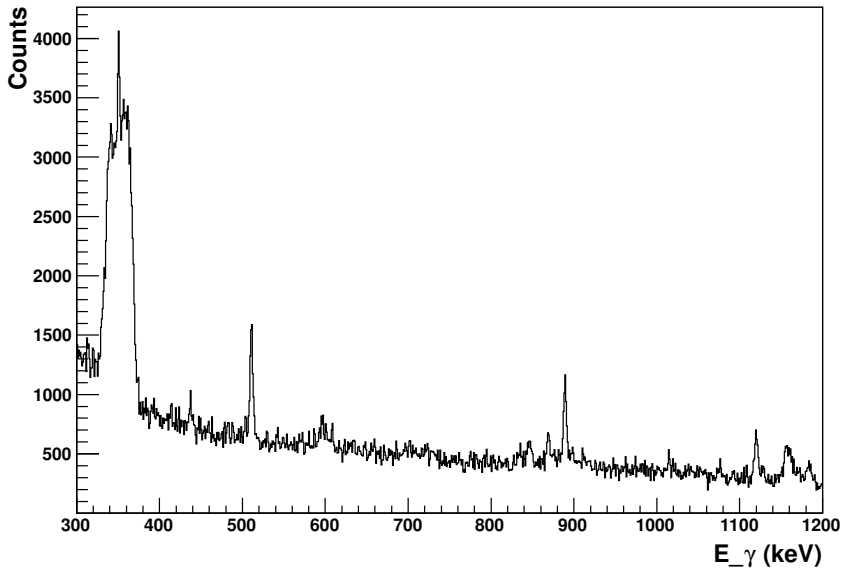

(b) ^{120}Sn target.

Figure 3.16: Energy calibrated γ-spectra from all runs with ^{21}Ne on the (a) ^{60}Ni and (b) ^{120}Sn targets. Note that the first excited state in ^{21}Ne at 351 keV vanishes among the very high background from the ^{60}Ni target.

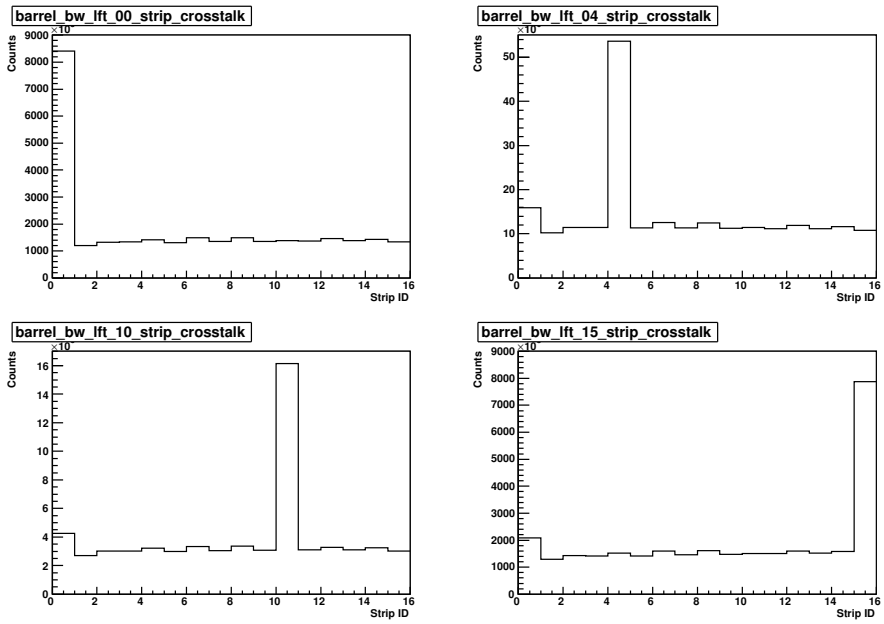

Figure 3.17: Accumulated readouts with the ^{120}Sn target from strips in the backward-left ΔE detector for events where one of strip 0, 4, 10 and 15 (0 closest to the target) was found to have the strongest signal. Cross talk would have been characterized by slopes on either side of the selected strips. The additional statistics in the first strip can be seen in all cross-talk histograms.

excited state in ^{21}Ne are shown in Fig. 3.19. Structures resembling the curves in Fig. 3.8 were expected but not present. Random coincidence events were cut with a low energy threshold of 6 MeV, as described earlier.

The first excited state of ^{21}Ne with Doppler correction based on the information from calibrated particle spectra is presented in Fig. 3.20.

3.8 Asymmetry value

Raw particle counts used in the calculations are given in Tab. 3.6. The following presentation of the results assume that counting errors are purely statistical and Poisson-distributed.

A direct application of Eq. 2.64, i.e. assuming negligible contribution from tensors with rank $k > 1$, is visualized in Fig. 3.21 with exact values and statistical errors listed in Tab. 3.7. In this case, efficiency factors have not been canceled out since comparison and identification of features in the data is more straightforward. The baseline in the data points from the oblique foil angles can be normalized with respect to the data from the perpendicular

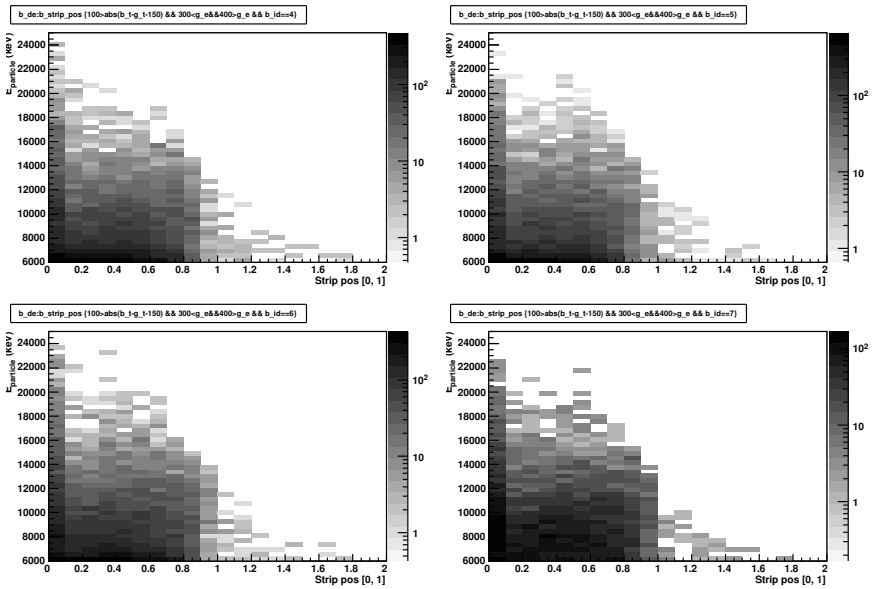

(a) ^{60}Ni target.

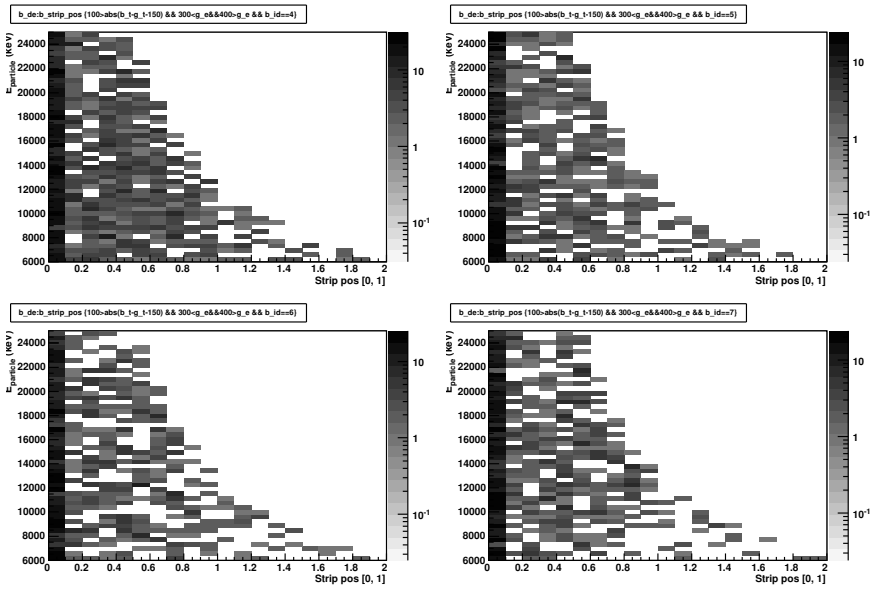

(b) ^{120}Sn target.

Figure 3.18: ΔE vs resistive layer plots to reconstruct length-wise strip position according to Eq. 3.2. Note that the $1/x$-curves that outline the data points have a slope equivalent to the maximum channel number of the ADCs at 3840, and the higher recoil energy with the ^{120}Sn target shows less structure, which indicates that the gain of the ADCs was set too high.

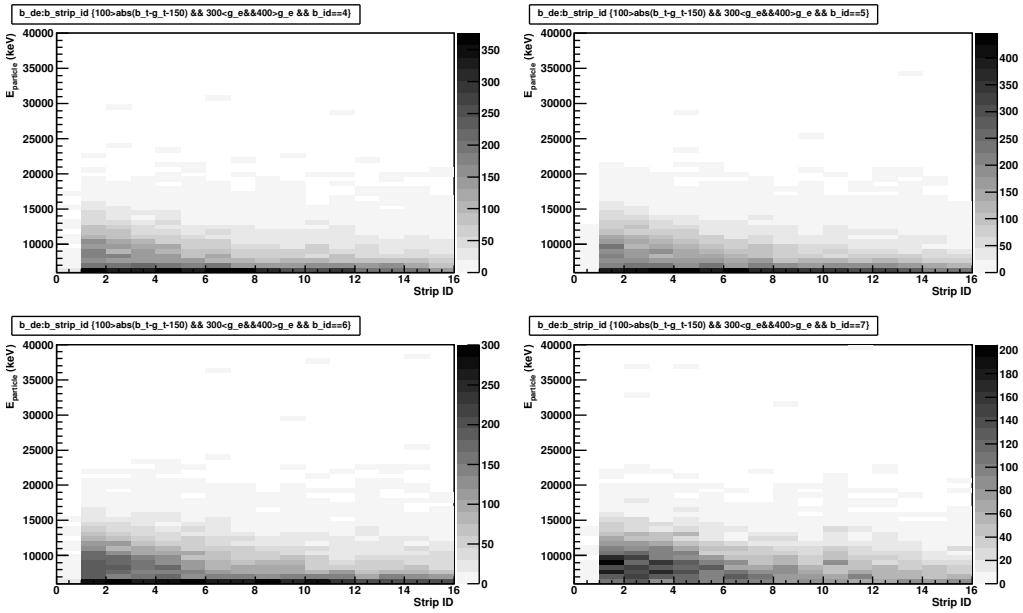

(a) ^{60}Ni target.

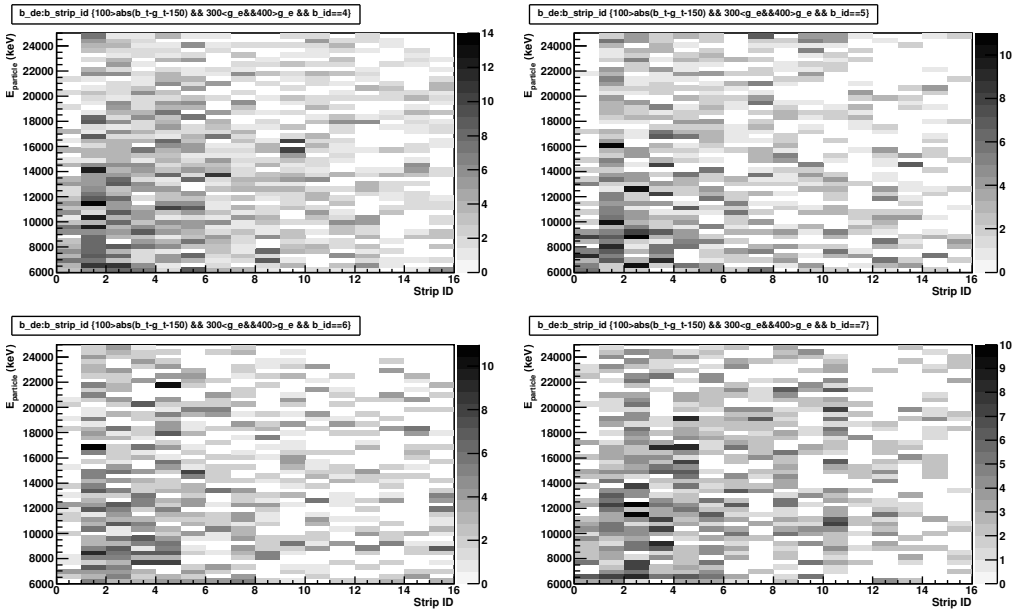

(b) ^{120}Sn target.

Figure 3.19: Backward barrel ΔE vs strip id with a γ-gate around the first excited state at 351 keV in ^{21}Ne. Particles below 6 MeV consist of random coincidences which were investigated using γ-peak integrals. Compare to the kinematics curves in Fig. 3.8 (note the difference in units).

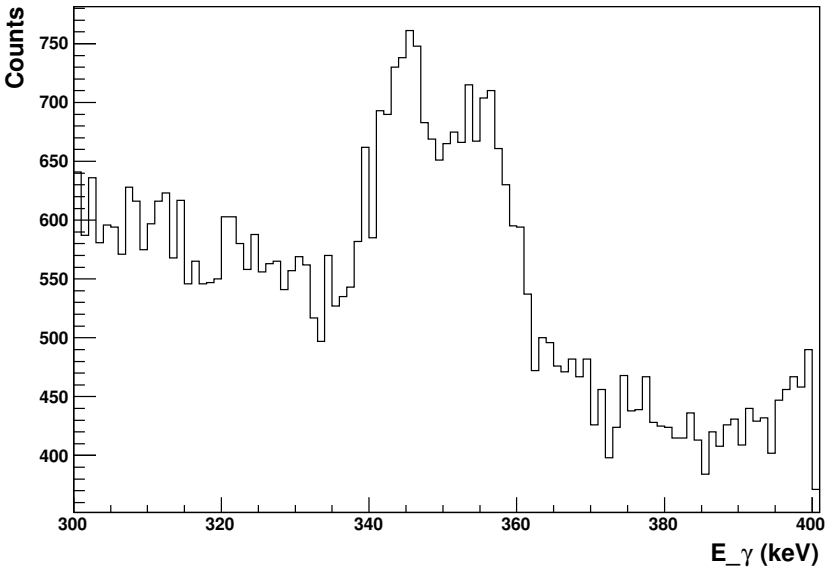

(a) ^{60}Ni target.

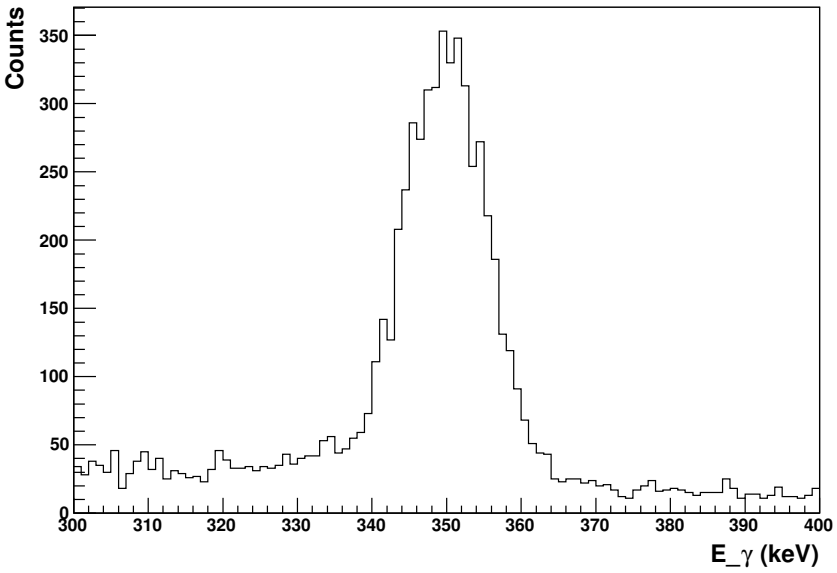

(b) ^{120}Sn target.

Figure 3.20: Doppler-corrected first excited state of ^{21}Ne on the (a) ^{60}Ni and (b) ^{120}Sn targets. Notice the small signal-to-noise ratio with the ^{60}Ni target compared to ^{120}Sn, which prompted for a switch of targets early during the experiment.

Table 3.6: Raw integrated event counts after event selection.

Detector	$\alpha = -70°$	$\alpha = +70°$	$\alpha = 0°$
Left	854	764	153
Up	562	598	101
Right	540	517	96
Down	572	486	82

foil angle, which is presented in Fig. 3.22 with exact values in Tab. 3.8.

The double ratio asymmetry, from Eq. 2.35 and Eq. 2.37, and statistical errors are presented in Fig. 3.23 with exact values listed in Tab. 3.9. Six double ratio asymmetries were calculated, combining data with the different foil angles $\alpha = \{-70°, +70°, 0°\}$ and from left-right and up-down detector pairs.

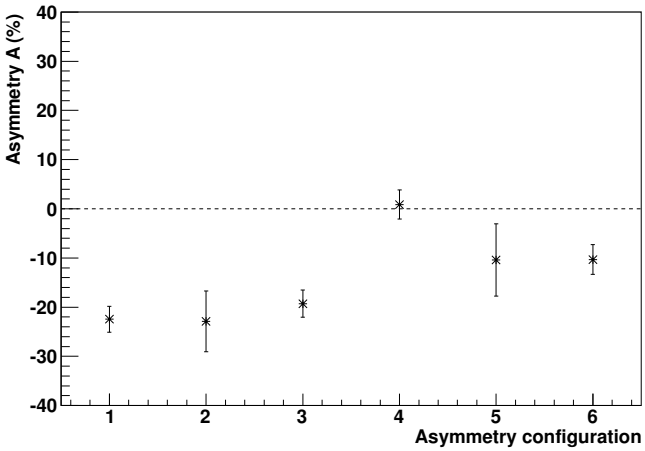

Figure 3.21: Asymmetries extracted according to Eq. 2.64 for fixed foil angles. Exact values and the asymmetry configurations given on the horizontal axis can be found in Tab. 3.7.

Table 3.7: Calculated particle asymmetry, using Eq. 2.64. L/R denotes ratio between left and right detector counts and similarly for U/D, and the angles denote the tilt angle of the foil for data in Tab. 3.6.

Configuration ID	Configuration	Asymmetry %	Error %
1	L/R −70°	−22.5	2.6
2	L/R 0°	−22.9	6.2
3	L/R +70°	−19.3	2.7
4	U/D −70°	0.9	3.0
5	U/D 0°	−10.4	7.4
6	U/D +70°	−10.3	3.0

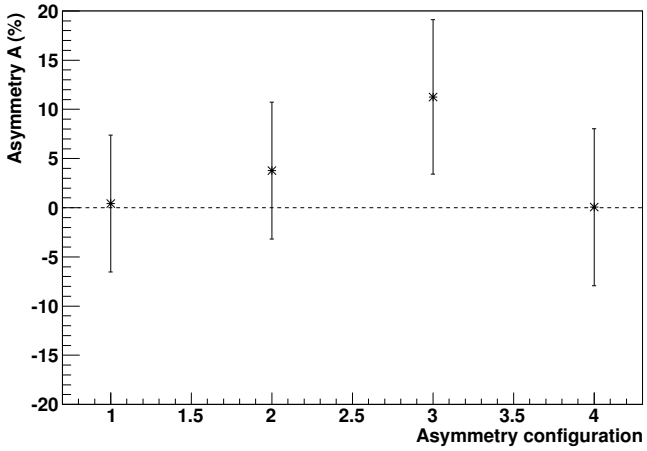

Figure 3.22: Normalized asymmetry based on asymmetry with the foil angle $\alpha = 0°$. Exact values and the asymmetry configurations on the horizontal axis can be found in Tab. 3.8.

Table 3.8: Normalized asymmetries and errors based on asymmetry from $\alpha = 0°$ for data in Tab. 3.6.

Configuration ID	Configuration	Asymmetry %	Error %
1	L/R $-70°$	0.4	6.9
2	L/R $+70°$	3.8	7.0
3	U/D $-70°$	11.3	7.9
4	U/D $+70°$	0.05	8.0

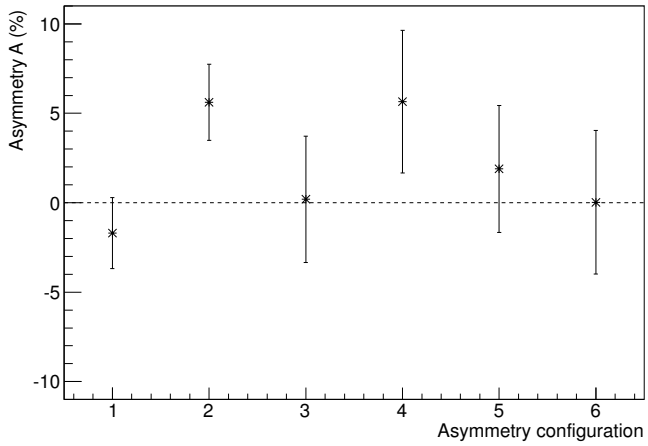

Figure 3.23: Double ratio asymmetries calculated from combinations of detector pairs and foil tilting angles. Exact values and the asymmetry configurations given on the horizontal axis can be found in Tab. 3.9.

Table 3.9: Double ratio asymmetries with permuted combinations of ratios and foil angles. The configuration ID is the x coordinate in Fig. 3.23, L/R and U/D denote the event count ratio between left/right and up/down detector pairs and the angles denote the tilt angle of the foil.

Configuration ID	Configuration	Asymmetry %	Error %
1	L/R $-70°/+70°$	-1.7	2.0
2	U/D $-70°/+70°$	5.6	2.1
3	L/R $-70°/0°$	0.2	3.5
4	U/D $-70°/0°$	5.6	4.0
5	L/R $+70°/0°$	1.9	3.6
6	U/D $+70°/0°$	0.03	4.0

3.9 Discussion of results

If the nuclear spin polarization is the major contributor to particle scattering asymmetry, the asymmetry calculated with the L/R detector pair with a foil angle $\alpha = \pm 70°$ should be non-zero and all other asymmetries should be zero. This is however not the case. In Fig. 3.23, in which the double ratio method from Eq. 2.35 with Eq. 2.37 was used, the asymmetry L/R is consistent with zero asymmetry within one σ. At the same time, the U/D asymmetry is 2.6 σ away from zero, with σ similar to the L/R asymmetry (due to comparable statistics). This means that there is clearly an instrumental asymmetry, which ideally should be taken into account and corrected for. In combination with the $\alpha = 0°$ baseline measurement, the statistical errors are too large to

draw any conclusion about measurements with individual foil angles.

The ratio from Eq. 2.64, used for Fig. 3.21, shows large baseline asymmetries. One possible reason for this is different detection efficiencies of the left and right detectors, which can be resolved by normalizing the event counts for the oblique foil angle measurements, as has been done for Fig. 3.22. With polarization, in Fig. 3.22 we expect to see an asymmetry in L/R of opposite sign for $\alpha = \pm 70°$. However, within statistical errors, the asymmetry is consistent with zero. Measurements with U/D should be close to zero and they are within 1.5 σ.

To summarize, within the statistics that were collected for this experiment, we can not conclude whether an asymmetry due to nuclear spin polarization of the scattered particles was measured or not.

3.9.1 Degree of polarization

The electron polarization p_J of ^{21}Ne in any of the charge states present after passage through each foil should be within 5 % to 20 % as reported from previous experiments [29]. With 3 foils and $p_J = 5\,\%$, Eq. 2.10 yields a nuclear polarization of $p_I \approx 3\,\%$, and with 20 foils $p_I \approx 11\,\%$.

Due to the low statistics, there was no opportunity to extract the analyzing powers, and thus also no definite conversion factor from the asymmetry to the nuclear polarization is available. An alternative approach would be to include spin polarization in the widely-used Coulomb-excitation code GOSIA [34]. The Warsaw group is presently trying to implement this feature in the code, but the project is not yet finalized. In the meantime we tentatively say that the asymmetry can be only smaller than or equal to the underlying polarization, thus any observed particle asymmetry would at most amount to a few percent. The present result could therefore be consistent with the expected asymmetry, only the statistical uncertainties are too large. Clearly, one way to improve the result would be to decrease the statistical errors and to increase the initial nuclear polarization, possibly by a longer experimental run and by introducing more foils. However, each foil interaction causes energy loss and angular straggling of the beam, so the number of foils was kept at a moderate level for this experiment.

3.9.2 Remaining issues

We will discuss some problems with the present data, which led to lower than expected statistics and which might have caused some systematic effects. If a new experiment can be scheduled at ISOLDE, the following points should be addressed:

As demonstrated in Fig. 3.18, there was a problem with the barrel strip length-wise positioning. Above 12 MeV the resistive layer readout did not provide sufficiently high readout to compensate for the high readout of the ΔE detector. Scattering kinematics and plots show that there is a lot of statistics at higher energies that are lost with an energy cut at 12 MeV. In summary, the position information could not be used consistently for most events.

Due to the lack of position information from the barrel strips, Doppler correction could not be performed to the full extent possible with Miniball. The resulting broad peaks introduce integrated background which in turn reduces the asymmetry value. It is possible to exclude the integrated background, but the error increases. Assume that $n_i = N_i + e_i$, where n_i is the observed count rate in direction i (left or right), N_i is the count rate from events which we are interested in and e_i is the contribution from the background. If efficiency factors can be ignored, the correct asymmetry value would be

$$A = \frac{N_r - N_l}{N_r + N_l} = \frac{(n_r - e_r) - (n_l - e_l)}{(n_r - e_r) + (n_l - e_l)} = \frac{(n_r - n_l) - (e_r - e_l)}{(n_r + n_l) - (e_r + e_l)}. \tag{3.5}$$

The background sum in the denominator is the integral of background events, which is trivial to estimate. The background difference in the nominator is not as trivial, but efficiency or other proportional artifacts vanish in a double ratio expression. One possibility to make use of the cancellation of the efficiencies in the double ratio, and to extract n_l and n_r, since we know the ratio and the sum of counts, to transform measured asymmetry as

$$A' = \frac{1-\rho}{1+\rho} \approx \frac{n_r - n_l}{n_r + n_l}, \quad \rho^2 = \frac{n(\alpha, d_r)\, n(-\alpha, d_l)}{n(\alpha, d_l)\, n(-\alpha, d_r)}, \tag{3.6}$$

$$n = n_r + n_l \Rightarrow \begin{cases} n_r \approx n(A'+1)/2 \\ n_l \approx n(1-A')/2 \end{cases}, \tag{3.7}$$

$$e = e_l + e_r, \tag{3.8}$$

$$A \approx \frac{n_r - n_l}{n - e} = \frac{nA'}{n - e}, \tag{3.9}$$

where α is the absolute value of the foil tilting angle, and d_i represents the left or right detector. This will improve the asymmetry value because $n/(n-e) > 1$, but the error grows due to the assumption of zero difference in the background. At this point, the large deviations in the asymmetry are of greater concern than the magnitude of the asymmetry, so no asymmetry improvements are presented.

The measured non-zero baselines were assumed to originate from detection efficiencies. However, additional artifacts may have been introduced because of the geometrical changes with the flipping foil angle, which invalidates expressing baselines from just the detector counts and first order efficiency coefficients, assumed for the analysis of this experiment. It is possible also that a fraction of the beam hit and scattered off the foil holder. To investigate these issue, the beam profile should be measured at the position of the foils. Another source of the baseline differences could be that the beam did not hit the target in the center, in which case the angular coverages of the left and right detectors would change slightly. Looking only at the geometrical coverage, the angular coverage of the left and right barrel detectors for a Gaussian beam in the target changes by 3.5 % if the beam is moved from the center by 2 mm in the horizontal plane along the target surface, and by 6.5 % for a 4 mm displacement. As a consistency check, a point-like beam was integrated numerically from an analytical expression and a Gaussian beam was simulated with Monte Carlo, both giving similar results. If this effect is not due to scattering on the foil holder, this type of error will vanish in the double ratio. However, a full simulation of scattering would be required.

Chapter 4

^{8}Li experiment

The particle scattering approach to measure nuclear spin polarization described in Chap. 3 has much lower efficiency and is not as well-tested as using the β-NMR. In order to measure the angular distribution of β-decay, an on-line β-decaying beam had to be delivered by ISOLDE and a new β-NMR system had to be installed at REX. The NMR magnet and related equipment were donated by Wolf Dietrich Zeitz from the former Hahn-Meitner Institute in Berlin, and were assembled and modified for use at a REX beam-line. Several other important components were designed and manufactured specifically for this experiment.

The location of the β-NMR is shown in Fig. 4.1, at the 20° REX-ISOLDE beam-line beside Miniball. The long distance between the blue bending magnet and the experimental setup allowed other experiments to be mounted on the same beam-line during assembly and preparation of our experiment. A simple illustration of the experimental setup can be seen in Fig. 4.2 and a photo in Fig. 4.3.

A beam of ^{8}Li was chosen for the experiment, which had already been used successfully in several polarization experiments [8, 27, 61]. This allowed comparisons of our results from other groups, but ^{8}Li is generally a suitable nucleus for polarization experiments. It is not an extremely exotic nucleus and has good production yields. The life-time of 0.840 s is practical experimentally and is less than the spin-lattice relaxation rate in the order of a few seconds in a well selected implantation target. The daughter-nucleus ^{8}Be after the second-forbidden β^{-}-decay will immediately α-decay and therefore will not contaminate the β-particle measurements.

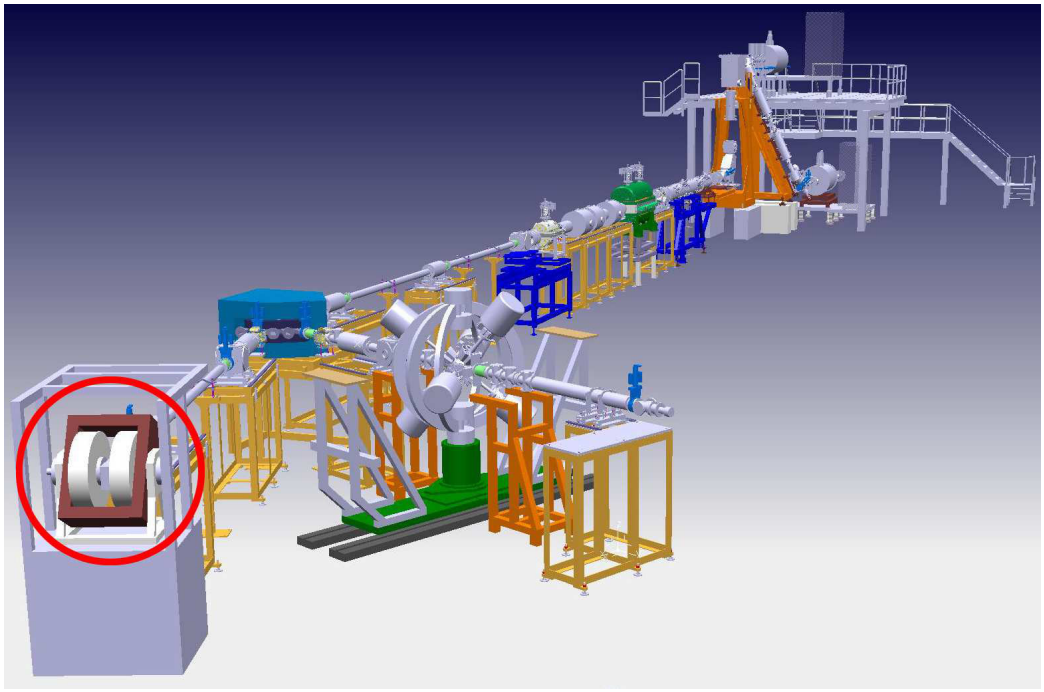

Figure 4.1: Location of the ^{8}Li experiment at the 20° beam-line at REX-ISOLDE.

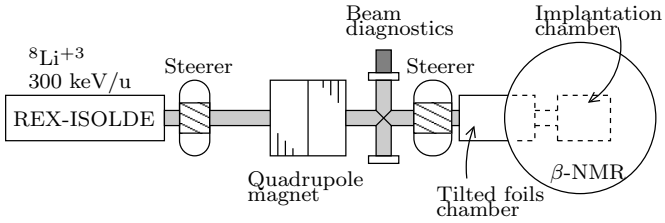

Figure 4.2: Overview of the ^{8}Li setup. The drift tubes were much longer in the actual setup, see Fig. 4.3, which prompted for the two steerers and the quadrupole magnet to be installed. The beam diagnostics cross piece contained vacuum equipment and a Faraday cup on a linear motion feed-through for current measurements before the foils chamber. The foils and implantation chamber had a manually controlled slow pumping vacuum system in the high pressure region to avoid rupturing the fragile polarizing foils.

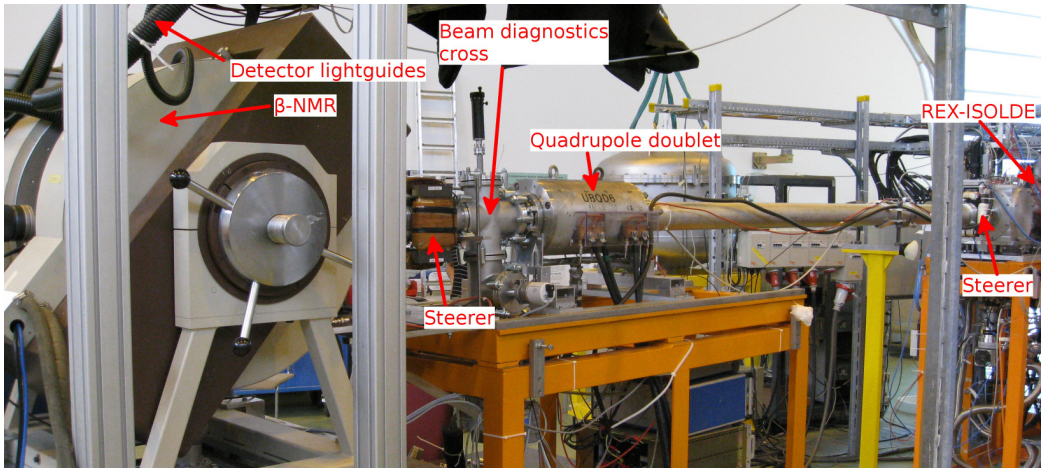

Figure 4.3: Photo of the ^{8}Li experiment. REX-ISOLDE provides the beam from the right side of the picture. The polarizing foils and implantation chambers are tightly integrated with the large β-NMR magnet, see Fig. 4.4 for a closer view.

4.1 ISOLDE and REX-ISOLDE setup

During preparatory beam tests and the actual experiment, ISOLDE received approximately 40 % of the protons from the PS Booster with an average interval of 3.3 s. The exact super-cycle setting changed on a hourly basis, but the average proton current over one super-cycle remained approximately constant. During the experiment, the proton current varied from 1.4 µA to 2.0 µA. The protons impinged on a tantalum-foil target mounted on the GPS, resulting in good yields for light beams and especially for ^{8}Li [48]. According to release curve measurements of ^{8}Li towards the end of the experiment, the mean yield was 7.18×10^{6} atom/µC, which translates to a yield from 1×10^{7} atom/s to 1.5×10^{7} atom/s.

The charge breeding in REX-EBIS was set to $q = +3$, corresponding to $A/q = 3/8 \approx 2.68$. The only significant contamination was from $^{16}O^{+6}$, which could be eliminated from the beam by carefully tuning the A/q selection magnet before the REX linac, owing to a difference in extraction energy of the $^{16}O^{6+}$ and $^{8}Li^{3+}$ out of REXEBIS.

Note that with the chosen mass-to-charge ratio, the ^{8}Li atoms were fully stripped and there would be no electrons to be spin-polarized. Thus, no nuclear spin polarization would be created either. However, the first few foils in the foil stack allowed some of the ions to pick up electrons and the remaining foils acted as polarizers. One carbon foil at 4 µg/cm^2 is enough to reach charge state equilibrium for the beam in this experiment [62]. In the final experimental configuration, a significantly thicker Mylar foil was used

to degrade the energy of the ions, which is even more effective to reach charge state equilibrium. The resulting charge state distribution was $q(+2) \approx 50\,\%$ and $q(+3) \approx 50\,\%$.

The reason charge breeding to $q = +2$ was not an option, is because $A/q = 4$ introduces large amounts of contamination from ^{12}C and ^{16}O among other stable isotopes. Large amounts of stable contamination, that may even dominate over the radioactive ions, can be ignored in certain experiments, but in this case they would increase the damage on the foils.

The REX linac was configured to deliver a beam with the energy 300 keV/u, the lowest available setting achieved by activating only the RFQ. The low energy beam has a large transverse emittance, with sensitive settings for the beam line elements, which is further complicated by the long and narrow experimental setup with many collimating sections. Therefore, additional beam focusing elements were installed between REX and the experiment: one H+V steering magnet immediately after REX, and one quadrupole doublet as well as an additional steerer pair just upstream of the foils chamber. The count rate of the beam ions entering the foil chamber was measured to 6×10^5 atom/s, leading to a transmission of approximately 5 % from the ISOLDE target.

4.2 Chambers

The experiment contained the tilted foils chamber, positioned outside the strong magnetic holding field of the β-NMR, and the implantation chamber with the target positioned in the center of the β-NMR magnet, refer to Fig. 4.4. The foil chamber was designed specifically for this experiment and was manufactured at the Weizmann Institute in Revohot, Israel. The original implantation chamber from the donated β-NMR system was kept, but it was modified, so that it included beam diagnostic tools to assure proper beam transport and to reduce background events from scattered particles and secondary electrons. A detailed description for the function and modifications of the two chambers follows below.

4.2.1 Tilted-foil chamber

The main features to be fulfilled by the chamber were a large transverse beam acceptance for up to 20 mounted foils, relatively easy access to change the foils, a smooth rotation of the foils to avoid breaking them, externally controlled reproducible flipping of the sign of the tilting angle, and a separate pumping system from the rest of the experimental setup. The final design

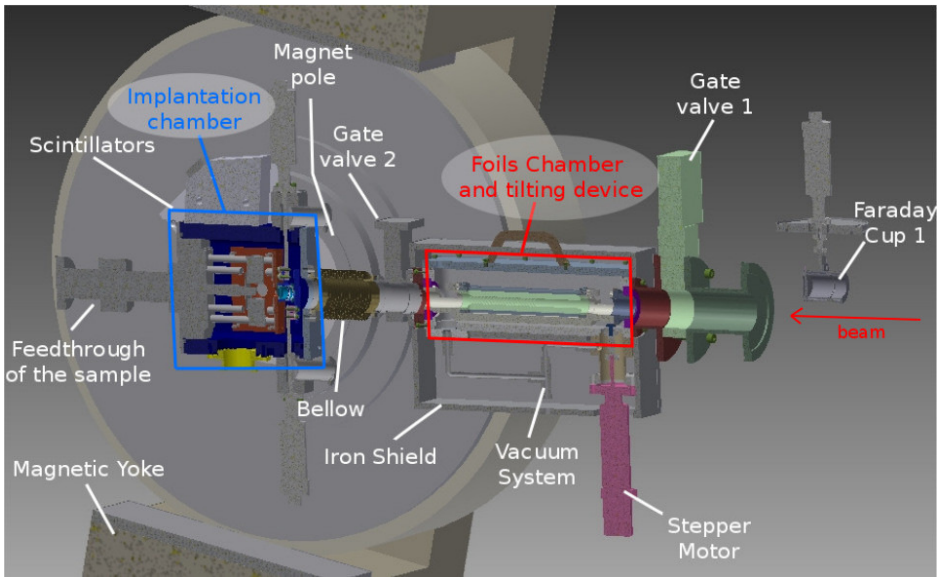

Figure 4.4: Cross section of the experimental setup from the diagnostics cross piece to the implantation chamber. A close-up of the foil chamber can be seen in Fig. 4.5, and of the implantation chamber in Fig. 4.8. The iron shield, designed to reduce the magnetic field strength from the β-NMR holding magnet was removed before the final data were recorded.

for the foil holder section can be seen in Fig. 4.5.

The foils must be tilted around their individual centers to provide a large acceptance, which is difficult to achieve with adjustable tilting angle. Therefore, the foils were rotated as a stack around the beam-line axis with fixed tilting angle. Although the absolute value of the tilting angle against the beam axis is fixed, this design allows for an arbitrary direction of the polarization vector perpendicular to the beam-line for future experiments. The foil tilting angle can be changed by replacing the foil frame holder, labeled *Tilted-Foils Holder* in Fig. 4.5, with slits at the appropriate angle. This intervention requires breaking the vacuum however.

To achieve smooth rotation of the foils, an inexpensive unipolar stepper drive kit with support for micro-stepping was selected. The torque transfer from the motor drive shaft to the holder was achieved by surface-contact between an conical aluminium drive and a rubber ring. A depiction of these mechanisms in the rotating holder can be seen in Fig. 4.6. The reproducibility could not be guaranteed with only stepper motor control with such a surface-contact arrangement however. To ensure reproducibility, a switch circuit that was closed in the two positions when the polarization vector was collinear with the β-NMR detectors was installed. A multimeter measured

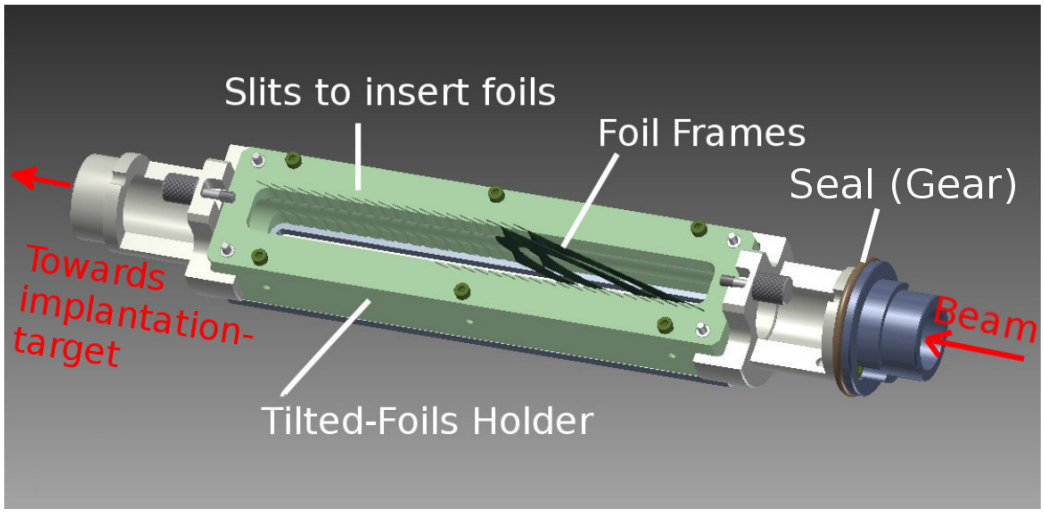

Figure 4.5: CAD drawing of the foil holder in the tilted-foil chamber. Typically, the foils are positioned as close as possible to the target to the left in the figure.

the resistance between an isolated stationary pin in the transparent acrylic glass lid and the conducting aluminium foil chamber with the rotating foil holder. When the circuit was open, the resistance was measured as out-of-range, and when closed, the resistance was approximately 40 mΩ.

The polarizing foils should be as thin as possible to reduce the effects of the foils on the beam. Energy loss and energy and angular straggling reduce beam transmission. For this experiment, we acquired self-supporting pure DLC foils with thickness 4 µg/cm^2 and a surface area of approximately 60×20 mm^2 from Technische Universität München, Germany. To improve the polarization efficiency by reducing the beam energy from 300 keV/u to 211.9(35) keV/u as was pointed out in Sec. 2.2.2, a Mylar foil with a thickness of 0.5 µm was installed before the carbon foils. This also has the positive side-effect of increasing the likelihood of electron-pickup of the fully stripped ^{8}Li before traversing the polarizing foils

Due to the thin foils, the vacuum pumping system had to extract air slowly on both sides of the foil stack in order to avoid large pressure gradients that could have ruptured the foils. Therefore, the foil section was isolated from the large volume contained in the drift tubes closest to REX-ISOLDE with a gate valve, which was especially important during the initial pumping phase close to atmospheric pressure. No parts in the implantation chamber were as fragile as the foils and the volume enveloped by both was small, so they were pumped simultaneously to 1×10^{-2} mbar in approximately one minute. A turbo pump was engaged at approximately 1×10^{-3} mbar, and

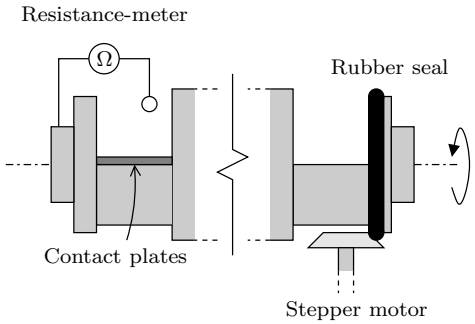

Figure 4.6: Depiction of the positioning and position feedback mechanisms at either end of the rotatable foil holder. The rubber seal on the right is connected via surface contact to the stepper motor to reduce vibrations. Such surface contacts may cause rotational slippage, so two contact plates were installed in the holder to close a circuit to a resistance-meter when the foils were directed to produce a horizontal polarization vector. Compare with Fig. 4.5.

the gate valve to the larger drift section was opened at 1×10^{-5} mbar. The final readings after one day of pumping were in the order of 10^{-7} mbar in the drift section and 10^{-6} mbar in the implantation chamber.

4.2.2 Implantation chamber

A sketch of the chamber can be seen in Fig. 4.7 and a cross-sectional view of the implantation chamber can be seen in Fig. 4.8.

The Faraday cup and beam collimators (5 mm and 8 mm) at the entrance of the chamber were connected to linear motion feed-throughs that moved vertically such that they could be finely adjusted or moved out of the beamline. Due to the effect of the horizontal holding field on the beam ions, their trajectory deviated vertically. Vertical translation of the beam diagnostic elements could therefore give an approximate estimation of the vertical beam profile.

Due to space constraints inside the chamber, the Faraday cup had to be designed and manufactured specifically this experiment. The technical drawing of a standard Faraday cup was scaled to suitable dimensions. However, the required suppression voltage until saturation of the current reading was at least 1 kV, an order of magnitude higher than 100 V which is more commonly employed. Readings were still consistent with standard Faraday cups and readout systems upstreams.

To reduce secondary scattering and implantation of decaying ions in locations other than the target, 7 mm thick copper-shielding surrounded the implantation target with collimators for the incoming beam and towards the

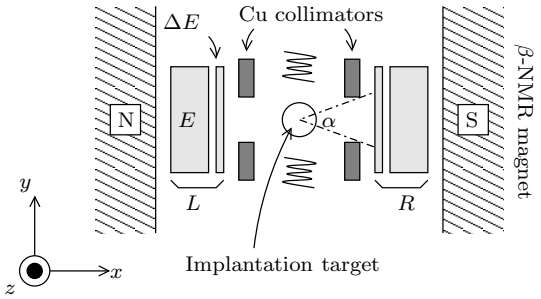

Figure 4.7: Illustration of the implantation chamber, with the opening angle $\alpha = 48.4°$. *The* ΔE *detectors had a thickness of* 3 mm *and the* E *detectors had a thickness of* 10 mm, *however no* $\Delta E/E$ *particle identification was performed within the experiment.*

two particle detectors. The opening angle to the detectors was $\alpha = 48.4°$ each, which gave a solid angle coverage of 8.8 % in total for both detectors. In the original chamber, the target was surrounded by heating wire which was removed in order to fit the copper collimators.

Each β-detector consisted of a pair of plastic scintillators, where the scintillator closest to the target had a thickness of 3 mm, followed by a scintillator with thickness 10 mm. The detectors were designed for $\Delta E - E$ particle identification, although this was not performed for this experiment due to negligible random coincidences. In order to measure the light output, the scintillators were coupled to flexible light-guides connected to XP2262 photomultiplier tubes located outside the magnetic field.

The target was fixed on a rotatable finger. During beam-tuning, the target was replaced by a copper plate which acted as an unsupressed Faraday cup measured by a pA-meter. Due to the lack of a suppressor, secondary electrons escaped the plate and the readings overestimated the actual beam current. Nevertheless, the plate provided a relative measure to determine how the beam changed during beam-tuning.

The RF was delivered by two coils on the vertical axis above and below the target, perpendicular to both the beam-line axis and the detection axis. This arrangement is necessary to destroy the polarization and to not interfere with the beam or β particles.

4.3 β-NMR elements

The holding field magnet was a water-cooled dipole electromagnetic Helmholtz coil that, according to specifications, could deliver a magnetic field with a strength of 1 T with an electrical current of 60 A. Due to the low energy of

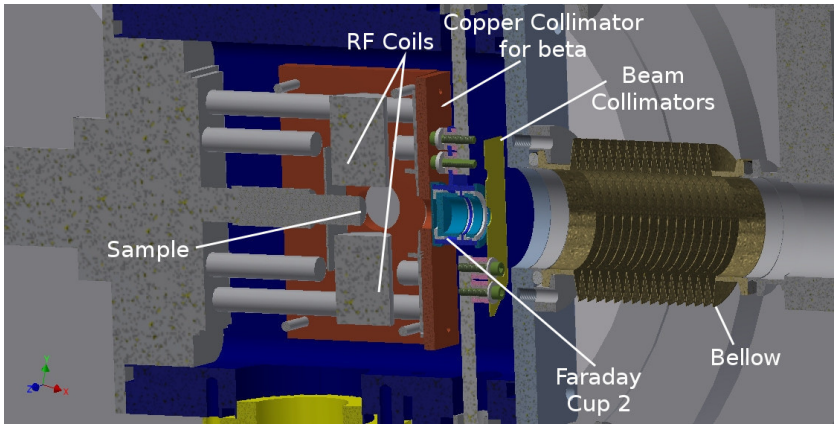

Figure 4.8: CAD drawing of the interior of the implantation chamber. The beam of polarized ^8Li entered the chamber from the right. The small Faraday cup and the collimators were attached to mechanical linear motion feed-throughs for vertical movement into and out of the beam-line. The cylinders above and below the target, connected to the back plate, were previously used for electrical heating, but served only as holders for the copper collimators in this experiment.

Table 4.1: Beam transmission from particle tracing simulation depicted in Fig. 4.9 and Fig. 4.10.

# foils	3	10	20
Transmission (%)	84.0	73.5	37.5

the beam, the magnetic field was set to 5×10^{-2} T, which was found not to cause a severe deviation of the beam trajectory and gave an appropriate field strength in the foil stack.

The magnetic field strength was measured along the beam-axis through the holding magnet with the chambers mounted. The largest magnetic field strength measured in the location of the foil stack was 5×10^{-3} T. Providing data for ^{8}Li ($A = 382$ MHz, $I^\pi = 2^+$ and $g_J = 0.826780(9)$ [63]) to Eq. 2.9 gives $B_{\text{coupl}} \approx 8.3 \times 10^{-2}$ T so the polarization transfer in the foil stack was deemed to be sufficient.

The measured field map also allowed for simulating the trajectory of a beam that had passed through a foil stack through the magnetic holding field which is presented in Fig. 4.9 and Fig. 4.10 with a 0.5 µm thick Mylar foil energy-degrader foil and 10 and 20 carbon foils, respectively. The simulated beam transmission for various numbers of foils is listed in Tab. 4.1. As can be seen, the angular straggling is of greater concern than the deviated trajectory.

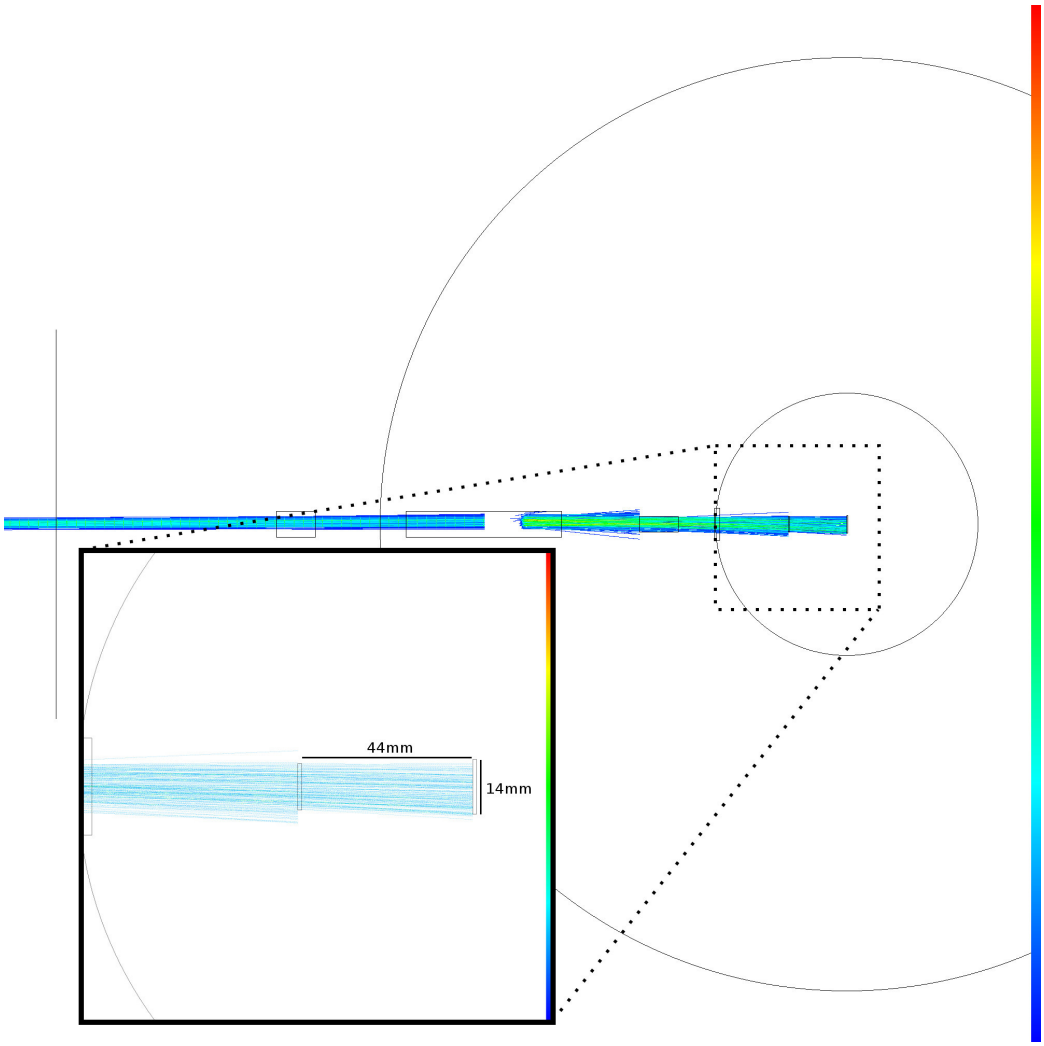

Figure 4.9: Simulation of a $^{8}Li^{2+}$ ion beam with an emittance based on REX-ISOLDE linac simulations, traversing a Mylar foil and 10 *carbon foils. The magnetic holding field is approximated with only the z-component as measured with a Hall probe. The collimators represented by the black outlines consisted of the narrowest passages in the setup. The color-map is a normalized density of particles in the beam.*

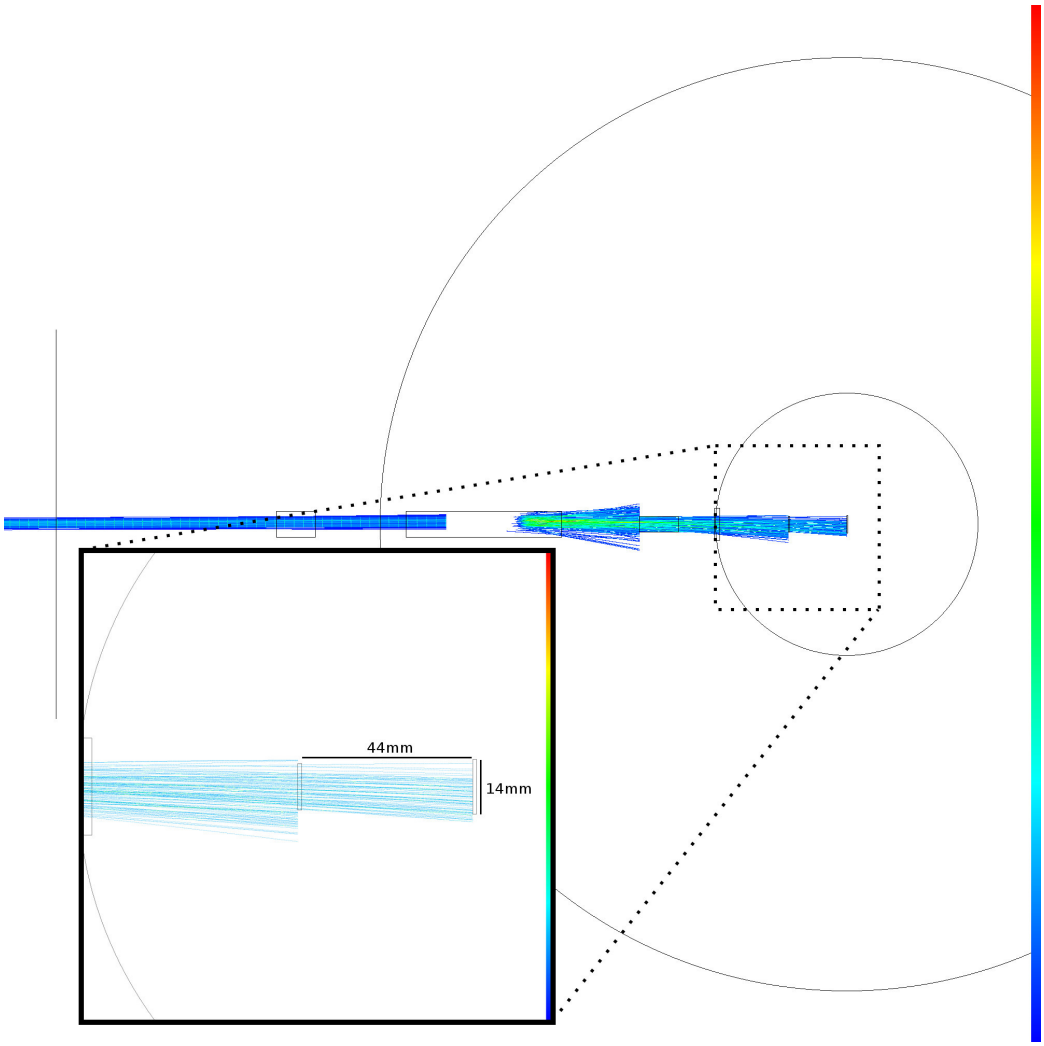

Figure 4.10: Similar plot to Fig. 4.9, but with 20 *foils.*

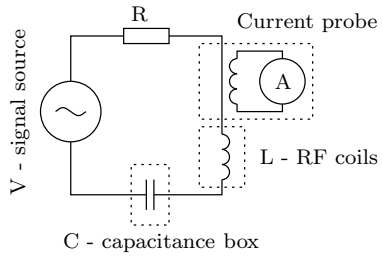

Figure 4.11: Simplified schematic of the RLC circuit to drive the β-NMR RF. The current probe was only installed during capacitance matching of the circuit.

4.3.1 RF

A schematic depiction of the RF circuit used is shown in Fig. 4.11. During the experiment, an RF signal ($\Delta f = 100\,\mathrm{kHz}$) broadly sweeping around various frequencies around the resonance at 315 kHz was injected into the circuit.

Due to the bandwidth limitation of an RLC circuit, there is a compromise between peak power at resonance and the power distribution off resonance. The RF output power was approximated with the AC current measured using a current probe read out by an oscilloscope. The capacitance was adjusted in a capacitor box and was selected to give a peak-to-peak amplitude less than 10 % over the frequency sweep. Even though configured for a non-optimal power output at resonance, the circuit was able to produce the necessary RF power to generate a peak magnetic field strength of 0.4 mT.

Since the effects of applied RF remain until radioactive decay ($\tau_{1/2} \approx 0.8\,\mathrm{s}$) or spin-lattice relaxation ($\tau_r \approx 4\,\mathrm{s}$) has lowered the nuclear spin polarization of ions implanted in the β-NMR target, data collected for 5 s after the RF configuration had changed between sweeping regions were designated *relaxation* data and were not used for the evaluation of the degree of polarization. All RF statuses were therefore:

1. RF on resonance.
2. RF off resonance by an arbitrary frequency shift.
3. No RF applied.
4. Relaxation of RF effects.

The RF frequency setting was fed as a bit-mask to four channels of the data acquisition system as constant high or low signals from a parallel port on the PC controlling the experiment, see Tab. 4.2. Triggers from the particle detectors could then directly be merged with the frequency information to

allow online analysis of the counting asymmetry for the swept frequency range.

4.3.2 Electronics and data acquisition

The photomultiplier tubes for the particle detectors provided one positive anode and negative dynode output each. The anodes were amplified and used as energy signals, and the dynodes were used for coincident timing in TACs. All data were read with a single CAEN v785 32-channel ADC. Four channels were designated for the energies of the two particle detectors pairs, two channels for the two TACs, four channels for the RF status which could allow up to $2^4 - 3 = 13$ frequency regions around the resonance, and two channels for the foil orientation status. The status data were provided via a parallel port from the PC that controlled all electronics for the experiment.

Triggering, read-out and time-stamping of the ADC and external signals, such as the target proton impact and EBIS release, was performed by a VULOM module [64] with the TRLO II system [65] at a clock rate of 100 MHz. The collected data were unpacked and presented online in an asymmetry plot, while a more detailed analysis was carried out after the experiment.

4.3.3 The rejected iron shield

Early in the project, the strong magnetic holding field of the β-NMR caused some concern due to the vertical deviation of the beam of several mm and the reduced coupling between the electronic and nuclear spins. In order to reduce the effect of the magnetic field, an iron shield surrounding the foil chamber was designed and installed, as can be seen in Fig. 4.4. During a pilot test of the setup with radioactive ^{27}Na and during the first few hours of data collection with ^{8}Li, no β asymmetry was detected. Since the iron shield reduced the magnetic field strength inside the foil chamber while the strength was unchanged outside, the magnetic field gradient was very abrupt around the exit of the iron shield. High field gradients and complicated field profiles can cause undesired behavior of magnetic moments, which destroyed any nuclear spin polarization. Therefore, the iron shield was promptly removed, with similar beam transmission before and after. There was not sufficient beam-time to investigate the exact impact of the iron shield.

4.4 Data analysis

Raw energy and timing data are presented in Fig. 4.12, based on a sub-set of all the collected data (data for approximately 1 h) for a fixed foil angle. Only the largest peak in each TAC was used for gating conditions for β-particle counts, since the total integral of the smaller peaks was at most a few percent of the integral of the single large peaks. Since the smaller peaks appeared due to reflections and did not interfere with the measurement, they were not remedied.

Energy spectra gated on the TAC peaks are presented in Fig. 4.13. Background events have been suppressed by this simple gate, and was the single final gating condition. The $E/\Delta E$-relations were plotted with the aim to find energy cuts, and are presented in Fig. 4.14. There were no clear structures in the data so energy cuts were finally not used. The lack of structures in these plots means care must be taken for implanting beams with β-decaying daughter nuclei in the β-NMR for future experiments, as it may be difficult to identify the source of β-particles.

The RF signal as it progressed throughout the experiment is presented in Fig. 4.15, with the RF configuration given by Tab. 4.2 Set 1. The clear separation with the ADC bit-mask method made the automatic analysis simple.

4.5 Measurements

The experiment was prepared for beam using ^{8}Li, since the yield was sufficient for tuning. Beam transport up to the β-NMR was also rather sensitive to changes in A/q, e.g. scaling of the beam elements was not possible. Four days of beam preparation were allocated to the experiment, during which final beam optics and holding field counter-steering were selected.

In order to study the effects of the trajectory deviation in the magnetic fields, fine control of beam steering was compared to the effect of the strong holding field in the β-NMR, with results presented in Fig. 4.16. Relatively large horizontal steering gave only minor changes with no clear trend of the measured asymmetry, whereas small vertical steering gave a significant and clear effect. The effect from vertical steering matched the effect caused by changing the magnetic holding field, as expected. The significant difference in sensitivity in the horizontal and vertical steering has not been identified.

Since the polarization vector was horizontal, the orientation of the foils should give a symmetric horizontal spread but a small asymmetric vertical spread, so a small change in baseline between the two foil directions can also

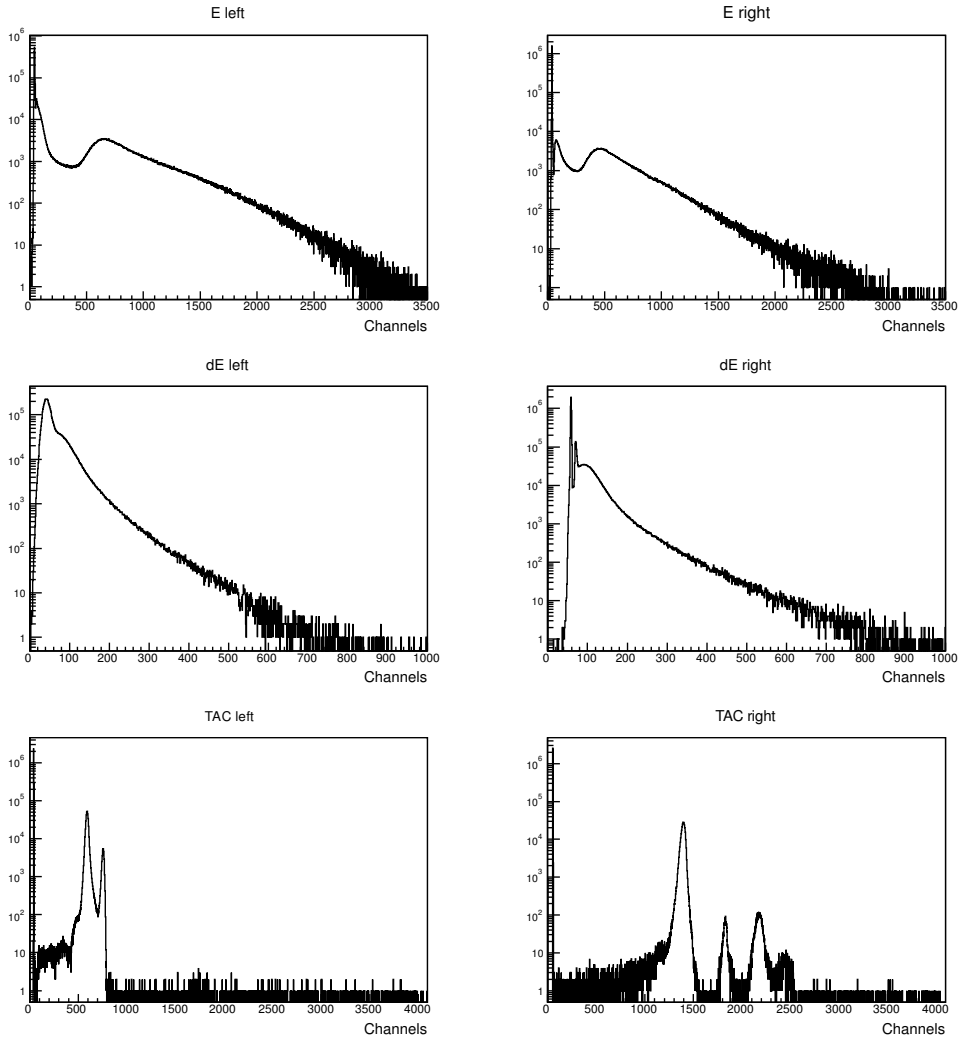

Figure 4.12: Raw ADC data collected from particle detector energies and time differences with two TACs. Compare with TAC-gated spectra in Fig. 4.13.

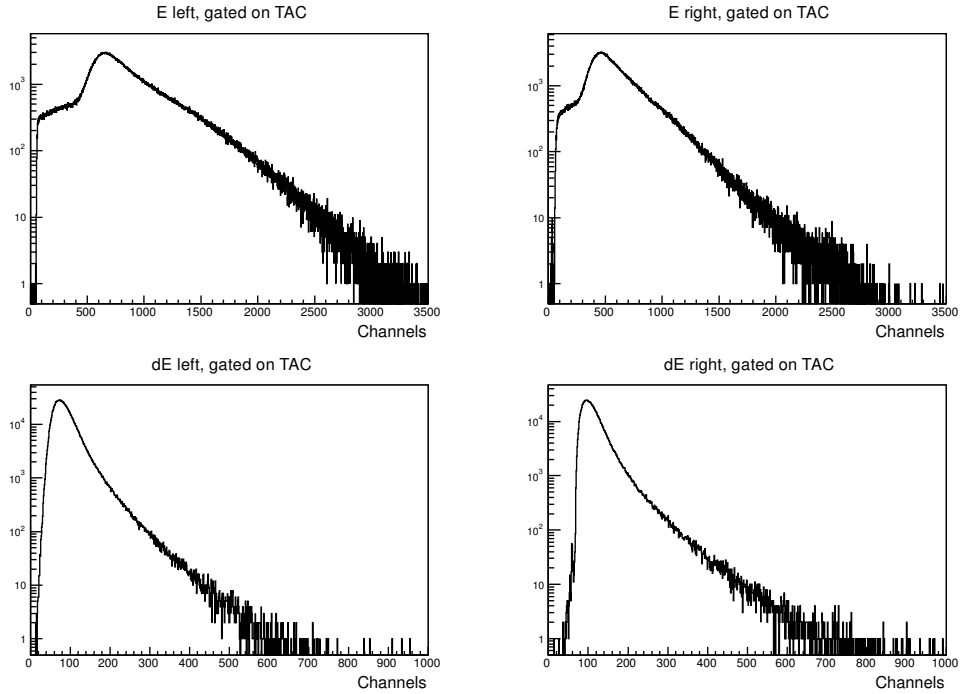

Figure 4.13: Energies gated by TAC peaks, source data are presented in Fig. 4.12.

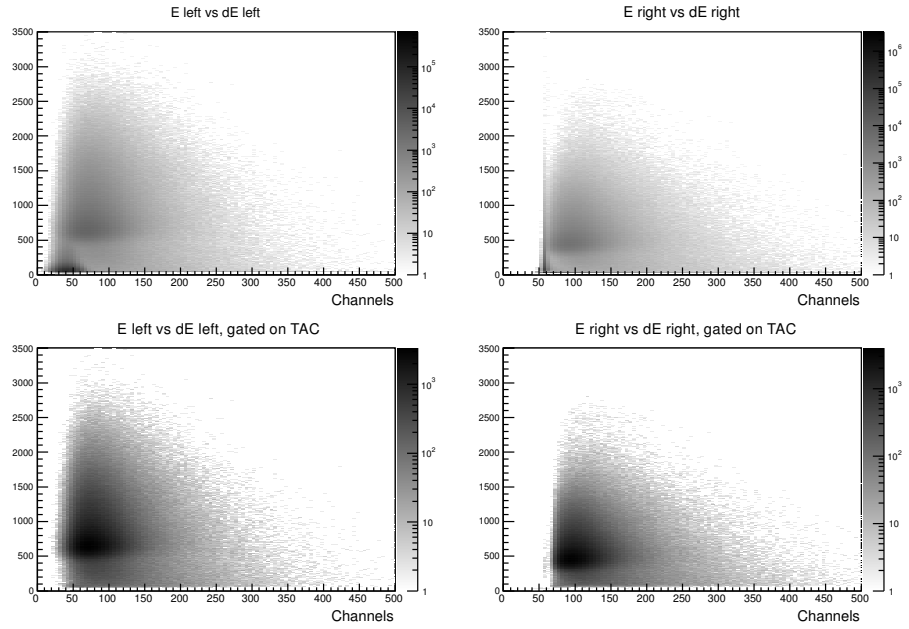

Figure 4.14: E vs ΔE plots, raw and gated. There are no distinct shapes visible that could be used for identifying background events not suppressed by gating on the TACs, so no energy cuts were performed.

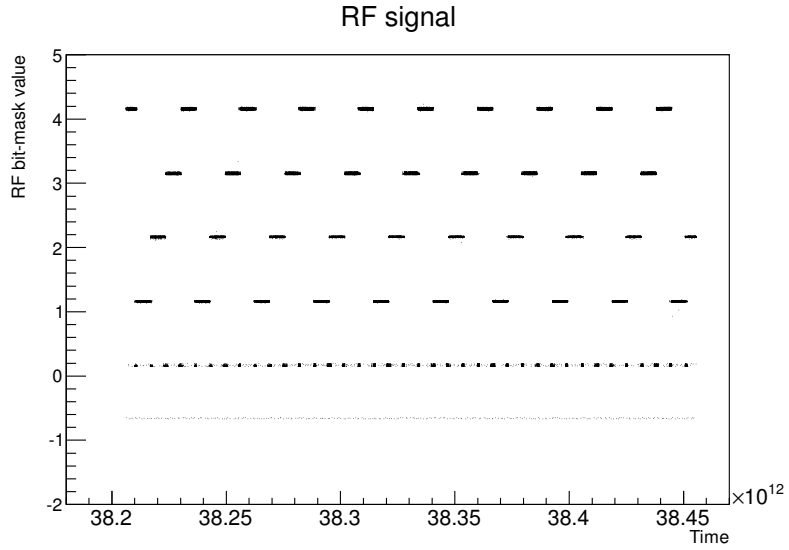

Figure 4.15: RF bit-mask value progression through the experimental run discussed in the data analysis section. The time step on the x-axis is 10 ns *and amounts to* 41 min. *See Tab. 4.2 Set 1 for the meaning of the RF values. Note that the negative data are background events.*

be expected, which is why so Eq. 2.38 is preferred to Eq. 2.37.

Before the iron shield was removed, the foils were arranged with a Mylar foil first and 4 foils, both carbon and polystyrene foils were tested. The target was a LiF *fcc* cubic crystal with good relaxation rate [66]. The target had a diameter $\varnothing = 14\,\text{mm}$ and a thickness of 1 mm.

At the time for the experimental shifts, data were collected for 24 h. Due to technical problems with the transfer line from the PS Booster to GPS, the experiment was cut short from the planned 56 h. In order to increase statistics in the reduced beam-time, the foil orientation was set manually approximately every 1 h and only one foil stack configuration and tilting angle was tested. The RF configuration was divided into two sets outlined in Tab. 4.2, and the RF configuration changed every 10 min. Also, no asymmetry was observed initially, which motivated the removal of the iron shield. To ensure results, the LiF target was replaced with Pt which had been used in other experiments despite having worse reported relaxation time, and the number of polarizing foils was increased from 4 to 10 carbon foils while the Mylar foil remained first in the stack.

The first set of data producing polarization-induced β-asymmetry was collected with the foils at $-70°$, and with one RF sweep off-resonance on either side of the resonance frequency. The second set of data was collected

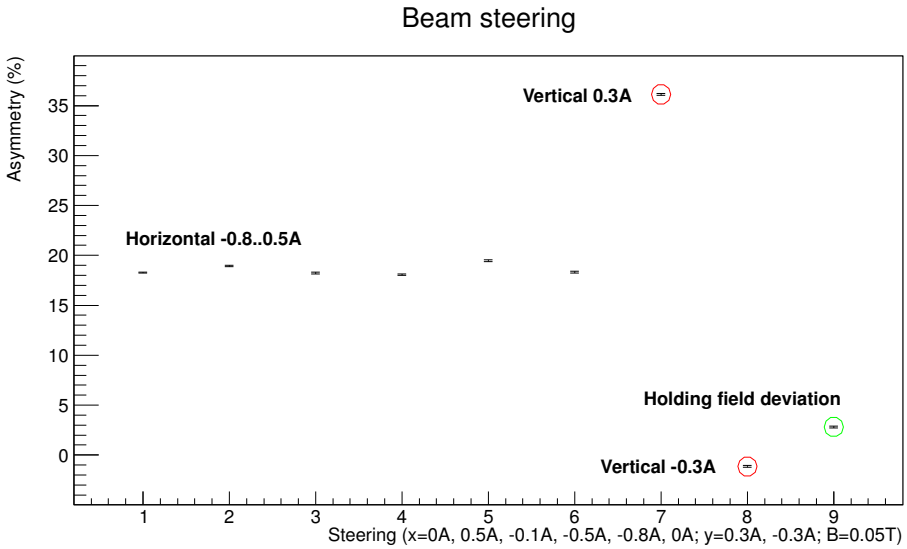

Figure 4.16: Measured counting asymmetry of the beam due to beam steering and the magnetic holding field. The effect of vertical deviation of the beam trajectory due to steering or the magnetic holding field is significant compared to the effect of horizontal deviation. The source for this phenomenon has not yet been identified definitely. Note that every sample point has very small vertical error bars.

Table 4.2: ADC bit-mask provided for the ADC. Set 1 was used during initial rough sweeps, and Set 2 were used for a finer sweep to obtain a smoother β-NMR signal.

Set 1	Set 2	ADC bit-mask
Relaxation	Relaxation	0000
0 kHz	0 kHz	0001
265 kHz	295 kHz	0010
315 kHz	305 kHz	0011
365 kHz	315 kHz	0100
-	325 kHz	0101
-	335 kHz	0110

Table 4.3: Experimental asymmetry amplitudes calculated with $\varepsilon = (R-L)/(R+L)$ from different runs in the experiment. Run 1 = set 1 RF configuration with foils oriented to $-70°$, run 2 = set 1 RF configuration with foils oriented to $+70°$ and run 3 = set 2 RF configuration with foils oriented to $+70°$. These results are plotted in Fig. 4.17.

RF (kHz)	Run 1 (%)	Run 2 (%)	Run 3 (%)
0	13.40(7)	13.30(7)	13.45(8)
265	13.50(6)	13.27(7)	-
295	-	-	13.46(8)
305	-	-	14.00(8)
315	12.68(7)	14.30(7)	14.12(8)
325	-	-	13.62(8)
335	-	-	13.52(8)
365	13.40(7)	13.41(7)	-

Table 4.4: Asymmetry magnitude with baseline removed and degree of polarization as calculated from β-asymmetries in Tab. 4.3 using Eq. 2.44 and Tab. 4.5.

	Run 1 (%)	Run 2 (%)	Run 3 (%)
Asymmetry	-0.77(8)	0.99(8)	0.52(9)
Polarization	2.9(3)	3.7(3)	2.0(3)

with the foils at $70°$ and with the same sweeping pattern. The third and last set was collected with the foils at $-70°$ but with four RF sweeps off-resonance and closer to the resonance frequency, to obtain a finer β-NMR signal.

4.5.1 Measured β-asymmetry

The measured β-asymmetry amplitudes are listed in Tab. 4.3 and have been plotted in Fig. 4.17. The nuclear spin polarization, obtained from the asymmetry amplitudes using Eq. 2.44 with values from Tab. 4.5, is listed in Tab. 4.4.

The baseline shift of approximately 13 % in the recorded data, as clearly

Table 4.5: Parameters for ^{8}Li provided for Eq. 2.42 and Eq. 2.44 to convert an asymmetry amplitude to a degree of polarization. The electron energy is the approximate mean energy of the β-particles for the relativistic parameter β.

2α	A_1	$\overline{T}_{e^-}$	$\tau_{1/2}$	τ_r
48.4°	-1/3	13.1/3 MeV	0.840 s	4.3 s [67]

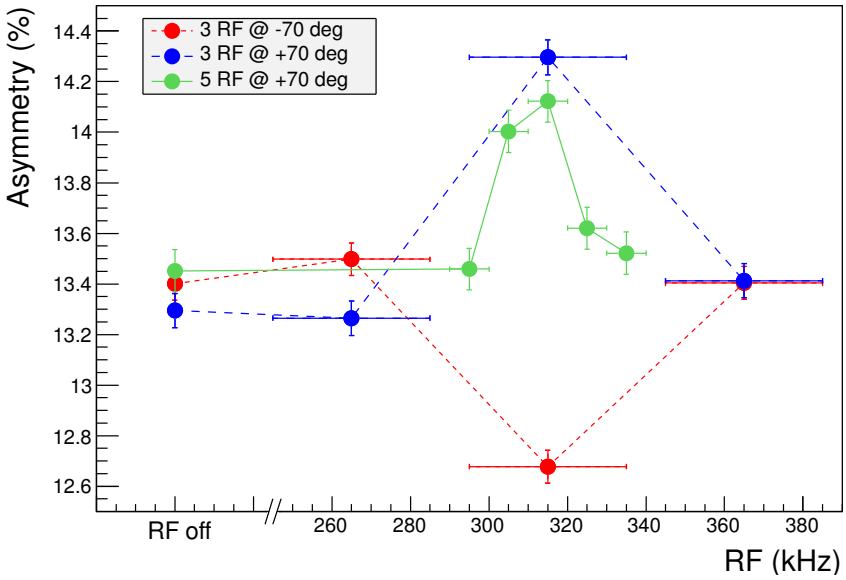

Figure 4.17: Plot of experimental asymmetries listed in Tab. 4.3. Horizontal error bars show the width of frequency sweeps, and the vertical error bars show the statistical errors.

seen in Fig. 4.17, is due to different efficiency coefficients for the left and right particle detectors and is an expected feature in β-NMR measurements. All sample points off resonance are within σ of each other, and the on-resonance peaks are several σ away from the baselines, so the evidence for nuclear spin polarization is clear.

For initial analysis and interpretation of β-asymmetries in the collected data, the intuitive and reliable expression used for Tab. 4.3 was preferred. When the data had been scrutinized, the final polarization values, as listed in Tab. 4.4, were calculated using Eq. 2.44 and Tab. 4.5 with raw detector counts.

4.6 Discussion of results

The maximum obtained degree of nuclear spin polarization of 3 % was within the expected limits based on results from experiments performed previously by other groups (from several percent up to 7 % [61]). There is a small difference (less than 2 σ) in the degree of polarization between the runs with $-70°$ and $+70°$ outside of the statistical error, which can be ascribed to the changed geometry and scattering dynamics in the foil stack.

There is also a clear offset in the raw β asymmetry of approximately 13 %. This shows the need to use RF to destroy the polarization in order to verify the source of the asymmetry and to extract the magnitude of the polarization.

In a similar experiment [61], ^{8}Li was polarized to a degree of up to 7.3(5)% using 15 thin polystyrene foils, each with a thickness of 4 µg/cm^2, at an incident beam energy of 141.5 keV/u with an outgoing energy of 59.6 keV/u after the foil stack. At an incident beam energy of 241.3 keV/u and with 10 polystyrene foils, which is closer to our experimental configuration, a polarization of 2.5(2)% was achieved. Let us consider the classical energy-independent model of nuclear spin polarization with multiple tilted foils from Eq. 2.10. In this case p'_J is an unknown parameter. Since a fixed number of foils were used for our experiment, only a one-point estimation can be made from our results, giving $p'_J \approx 2.6\%$. Using this result, the above formula with 15 foils would yield a nuclear spin polarization of $\sim 5.0\%$. Thus, it seems that a low beam energy is more advantageous.

4.6.1 Remaining issues

Three major modifications were performed to the setup during the experiment which produced the observed β-asymmetry. The impact of each change is not exactly known and should be addressed with future experiments. The modifications were:

- removal of the iron shield which is believed to have been the main reason,
- exchange of target from LiF to Pt, both reported to possess good spin-lattice relaxation times for implanted polarized ^{8}Li ions, and
- an increase of the number of polarizing foils from 4 to 10 carbon foils.

The iron shield was the least established part that was modified. The fringe fields and the abrupt non-adiabatic magnetic field gradient from the holding field at the exit of the shield could disturb the polarized nuclear angular momenta. Both targets have been reported to perform well with ^{8}Li, and previous experiments have been able to prove polarization with only one polarizing foil [20]. Even though the single-foil experiment utilized a beam of ^{4}He at 4.8 MeV/u, the last two modifications should have had minor impact in the measurements.

The tilted-foils technique is highly empirical and every available experimental parameter may have an influence on the results. The setup used

in this experiment allows easy systematic mapping of projectile energies by introducing varying thicknesses of Mylar foil, the number and types of foil material, and foil tilt angle. These three parameters can be used to optimize both the degree of polarization and the beam transmission. Before the tilted-foils technique can be considered concluded for ^{8}Li, these issues and also the effect of the iron shield and the target crystal need to be determined. Nevertheless, at some point a beam of ions with other properties, mainly with different nuclear spin and charge state from ^{8}Li, should be investigated, possibly even in conjunction with other physical objectives.

Chapter 5

Outlook

5.1 Magnetic moments of odd-even indium isotopes

Experiments using the tilted-foils technique at REX-ISOLDE have already been suggested, and the β-NMR setup in Chap. 4 may even be reused for experiments. One proposal to the ISOLDE experimental committee aims to measure the magnetic moments of ground and the first isomeric states of the odd-even indium isotopes ^{129,131}In ($Z = 49$) just below the doubly-magic nucleus ^{132}Sn ($Z = 50$ and $N = 82$) [68]. The magnetic moment of ^{127}In will also be measured for reference. Since the indium isotopes have a proton hole to the next closed shell and a number of neutrons in the vicinity of a closed shell, it is expected that collective nuclear effects should be rather small. Therefore, the exact behavior of the magnetic moments as a function of N, especially close to $N = 82$, could provide valuable input for current nuclear structure models.

All of the known odd-mass indium isotopes have a rather large ground state nuclear spin of $9/2^+$, and almost all of them are known to feature a $1/2^-$ isomeric state close to 300 keV. The magnetic moments of the ground state of the odd-mass $^{105-127}$In isotopes have been measured and are relatively constant, however the magnetic moment of the isomeric state varies widely as can be seen in Fig. 5.1 [69], an effect not yet reproduced by present nuclear models.

The ISOLDE yield for ^{131}In has been measured to 5×10^5 atom/µC using a uranium-carbide target and 600 MeV protons from the CERN SC (synchro-cyclotron) [48]. This is a factor 14 less in production compared to the ^{8}Li experiment at 7.18×10^6 atom/µC, which produced asymmetry error bars of 0.3 % under 3 h. This isotope has not been post-accelerated by REX-

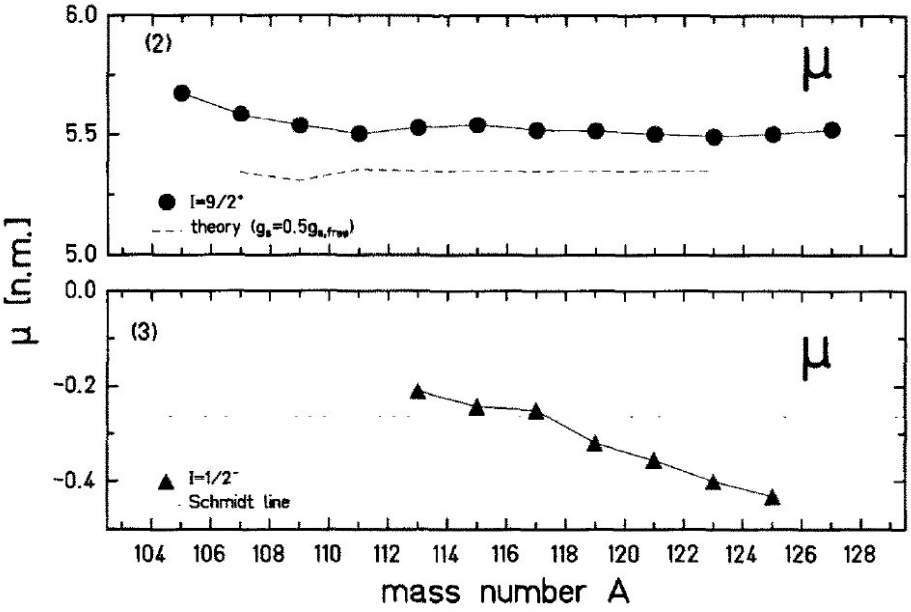

Figure 5.1: Magnetic moments of odd-even indium isotopes [69]. The top image shows the magnetic moment of the $9/2^+$ ground states, the bottom image the magnetic moments of the $1/2^-$ first isomeric state.

ISOLDE, so the exact beam transmission factor is not known. The expected beam transmission through REX should be similar to that of ^{8}Li. In any case, the experiment will be performed with the HIE-ISOLDE linac [70]. No yields have been presented for ^{129}In.

The isomeric state is purely β-decaying, thus the β-NMR is a suitable technique to measure the magnetic moments of the isotopes in question to high precision. Measuring the destruction of β-asymmetry, the g-factor can be extracted with Eq. 2.20 and Eq. 2.21. As explained in Sec. 2.2.2, the large nuclear spin $I = 9/2$ in this case can allow for large degrees of polarization with many foils. Obtaining polarization data for high-spin nuclides such as the indium isotopes can also increase the understanding of the tilted-foils technique.

5.2 Post-acceleration of polarized beams

As was mentioned in Sec. 2.2.2, the tilted foils technique favors beam energies around 100 keV/u. The in-flight nature of the tilted-foils technique and easy integration into existing beam-lines makes post-acceleration of the polarized beam to significantly higher energies possible. Good yields and

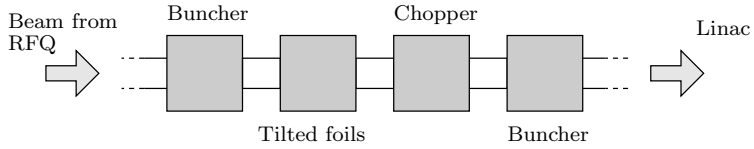

Figure 5.2: Suggested layout of the MEBT line for the HIE-ISOLDE linac to accommodate the tilted foils. The foil setup would be installed in a diagnostics box after a buncher that pre-accelerates the beam to compensate for the energy loss in the foils. Details are explained in Sec. 5.2.3.

preservation of the nuclear polarization closer to the MeV/u energy domain may provide more information in the analysis of Coulomb excitation and transfer experiments. This section will describe and summarize the work conducted to simulate the effects of ions undergoing tilted-foils polarization in the low-energy part of the linac and the subsequent post-acceleration. A large amount of input in beam characterization and the simulations through the linac beam elements were provided and performed by Matthew Alexander Fraser.

ISOLDE is currently undergoing a major upgrade with the HIE-ISOLDE project [70], which includes the design and construction of a new superconducting linac with high-acceptance focusing solenoids. All simulations were therefore performed for the new linac rather than REX. Because parts of the MEBT (Medium Energy Beam Transfer line) section [71] is still in the design stage, it is possible to consider the implementation of the tilted foils as an integral part of the linac. The current suggestion is to position the foils as illustrated in Fig. 5.2.

Some work on post-acceleration of polarized beams has been published [72]. Various beam element types with their characteristic magnetic field profiles were treated, and beams of optically pumped $^{6}Li^{3+}$ and $^{7}Li^{3+}$ were post-accelerated through various linac configurations with promising outcome. However, the polarization source and linac configuration were not identical to that of the HIE-ISOLDE linac, so a final implementation still requires further investigation.

5.2.1 Impact of magnetic fields

Any magnetic field in the linac will influence beam particles via their magnetic moments. For a detailed description of the effect of the magnetic fields typically produced by common beam elements on beam ions, refer to [72]. The simplest case is the strong dipole bending magnets used to e.g. bend the beam in sharp turns, to direct the beam to a particular experimental

setup, and for fine-tuning the beam direction. Horizontal bending, which will produce the largest dipole fields in the HIE-ISOLDE linac, operates with vertical magnetic field lines. The Larmor precession of magnetic moments in the bending magnets will thus happen around the vertical axis, so in order to keep the polarization through such fields, the polarization axis must be vertical. Horizontal field lines will be produced in vertical steering magnets, but such fields are comparatively weak.

The focusing elements in the HIE-ISOLDE linac will consist of superconducting solenoids, which utilize magnetic fields with the field lines parallel with the beam axis inside the cavity [73]. Fringe fields always exist at the entrance and exit of a solenoid. In such a solenoid magnet, a magnetic momentum will precess around the beam-line, so a nuclear spin polarization directed perpendicularly to the beam axis would be rotated. It is however possible to set a pair of solenoids with their magnetic field lines in alternating directions, or such that the accumulated rotation in all solenoids is e.g. $n \cdot 180°$, so that the direction of the polarization is vertical. A potential down-side with these restrictions is a reduced beam transmission because of possibly non-optimal focusing parameters for the solenoids.

The RF cavities produce magnetic fields which are ideally azimuthal and the acceleration occurs with longitudinal electric components. In practice however, stray transverse magnetic and electric components, which depend on the geometry of the loading arms, may exist close to the beam center where the azimuthal component vanishes. The transit time through the transverse fields in the accelerating gaps is typically very short, so the rotation around the transverse magnetic component in one gap is of the order of 0.01°.

The remainder of this section will assume a vertical polarization vector imposed by the horizontal bending magnets. Nevertheless, the treatment should be sufficiently general to allow the polarization vector to point in any direction perpendicular to the beam axis.

5.2.2 Impact of foil stack on the beam

Introducing the foils early in the linac presents some challenges due to the emittance growth in the foils. A large transverse emittance requires a large beam acceptance in the linac and increases the beam spot in experiments. A large longitudinal emittance reduces the acceleration efficiency, beam transmission, and the precision of experimental analysis that depend on the beam energy, e.g. Doppler correction and scattering kinematics. In order to reduce the emittance growth during passage through the foils, the beam should have a time and transverse focus in the foils.

The effects of the bulk matter of thin carbon and polystyrene foils on

^{8}Li were simulated with TRIM [74]. The incoming beam is point-like and has no energy spread, and TRIM produces a set of particles with outgoing energy, position and direction vectors. A variable number of both carbon and polystyrene foils with a thickness corresponding to $4\,\mu g/cm^2$, spaced with 1 mm between and with a tilt angle of 70° were simulated. The beam energy and spatial spread after the foils as a function of the number of foils are listed in Tab. 5.1 and are plotted in Fig. 5.3.

The TRIM output was applied in a custom program to a set of 9612 particles, that had been simulated through the RFQ at $A/q = 8/3$. Each particle in this set had an energy, position and direction vectors which were modified according to the TRIM data. The resulting particle set was then used for tracing through the remaining stages of the HIE-ISOLDE linac. Recall from Chap. 4 that the charge state changes from +3 to +2 for the polarized ^{8}Li ions, so the HIE-ISOLDE linac simulation needs to consider $A/q = 8/3$ before and $A/q = 8/2$ after the foils.

From the TRIM results, it seems polystyrene is the better choice with respect to the beam quality. However, this material does not conduct heat as well as pure carbon, and is therefore more sensitive to irradiation by ions. The longevity of the two types foils exposed to different beam energies and isotope masses needs to be measured.

The very small increase in energy spread and the angular straggling after the foil-stack would reduce the beam transmission through the linac and also the precision of the beam extents and energy for experimental analysis. Generally, the beam would still undergo post-acceleration but with some loss in transmission. The energy loss is of greater concern because post-acceleration will not function if the in-going beam energy to subsequent cavities is far from the fixed RFQ energy. A solution to this will be covered next.

5.2.3 Buncher compensation of energy loss

A buncher is an RF cavity with a few gaps used for reducing the temporal longitudinal extent of a bunch of ions at the cost of increased energy spread. Since the operation of a buncher is similar to that of the larger accelerating RF cavities, it can also accelerate the ions. This feature can be used to counter the energy loss in the polarizing foils already within the MEBT.

The energy loss in the foils should be compensated for before entering the foil stack. The Time Transit Factor (TTF) of the HIE-ISOLDE bunchers, plotted in Fig. 5.4, shows efficiency is increasing with increasing energy around the RFQ output energy. Only re-accelerating the beam after the foil stack would thus provide less gain in beam energy than pre-acceleration, and the number of foils that can be installed would be lower.

Table 5.1: Energetic and angular straggling of a point-like ^8Li beam with an incoming beam energy of 300.24 keV/u 20 cm *beyond the entry-point of a stack of foils as simulated by TRIM. Each foil had a thickness of* $4\,\mu g/cm^2$ *and they were angled at* 70° *against the beam line.*

Carbon foils

# foils	Energy (MeV/u)	σ_x (mm)	σ_y (mm)
1	0.291(3)	0.481	0.616
2	0.281(3)	0.925	0.896
3	0.272(3)	1.26	1.31
5	0.253(3)	1.66	1.54
10	0.205(5)	2.75	2.94
15	0.156(6)	3.82	3.59
20	0.109(7)	4.45	4.65

Polystyrene foils

# foils	Energy (MeV/u)	σ_x (mm)	σ_y (mm)
1	0.294(2)	0.183	0.162
2	0.286(3)	0.592	0.562
3	0.279(3)	0.920	0.930
5	0.265(3)	1.16	1.17
10	0.230(3)	1.70	1.65
15	0.194(4)	2.17	2.44
20	0.157(5)	2.87	3.08

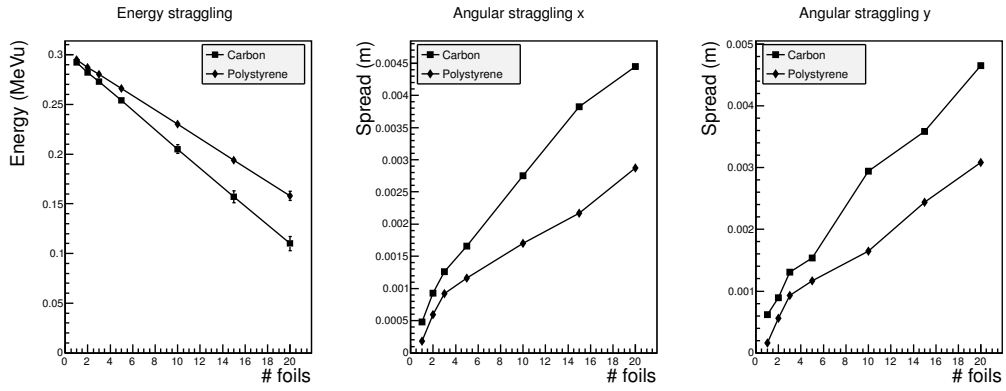

Figure 5.3: Beam energy and angular straggling after passing through carbon and polystyrene foils. Data points from Tab. 5.1.

The strength of the acceleration of a buncher is determined by the amplitude of the EM waves. The maximum acceleration voltage that can be supplied to the beam particles by the present amplifier and buncher is approximately 85 kV. If the source of this limit can be understood or new equipment is installed for HIE-ISOLDE, the bunchers may provide a higher acceleration voltage. With this limit, one buncher can compensate for the energy loss of only 2 foils with a $A/q = 8/3$ beam. Breaking the limit and supplying 100 kV to the buncher would allow having 3 PS foils installed.

Two important aspects of the actual polarization need to be taken into account when matching with the MEBT elements, namely the energy-dependence of the foil interaction and the nuclear spin of a chosen isotope. Tilted-foils polarization typically prefers beam energies lower than 300 keV/u, so pre-accelerating in a buncher will reduce the efficiency of the polarizer. A large nuclear spin may require at least 10 foils to reach polarization saturation, according to Eq. 2.10 and Fig. 2.12, which cannot be compensated for by one buncher. To fully appreciate all these effects to optimize the attained polarization, it would be necessary to look at the energy dependency of the foil interaction, the energy loss and the size of the nuclear spin. Little is currently known about the energy dependence of the foil polarization around the fixed RFQ output energy of 300 keV/u, although data for a stack of foils with beam energies up to 240 keV/u have been published [61].

Nevertheless, the beam bunches should be in a time focus when entering the IHS, the following beam element in the linac. Since the foil-stack should also be the location of a time focus, a two-buncher design is planned for the MEBT as is shown in Fig. 5.2. The first buncher would provide bunching and pre-acceleration for the foil-stack and the second buncher would prepare the beam for the remaining linac.

5.2.4 Simulation results

The typical normalized tranversal emittance of the beam that can be expected after the RFQ at $A/q = 8/3$ is

$$\varepsilon_x^* = 0.110 \text{ mm mrad}, \tag{5.1}$$

$$\varepsilon_y^* = 0.109 \text{ mm mrad}, \tag{5.2}$$

and the normalized emittance of the beam after various foil-stack configurations are listed in Tab. 5.2 and are plotted in Fig. 5.5. The emittances and beam transmission for various linac configurations with 3 PS foils and without any foils are listed in Tab. 5.3. Even with non-optimized settings for the linac, the beam transmission was at least 80 %. Detailed optimization of

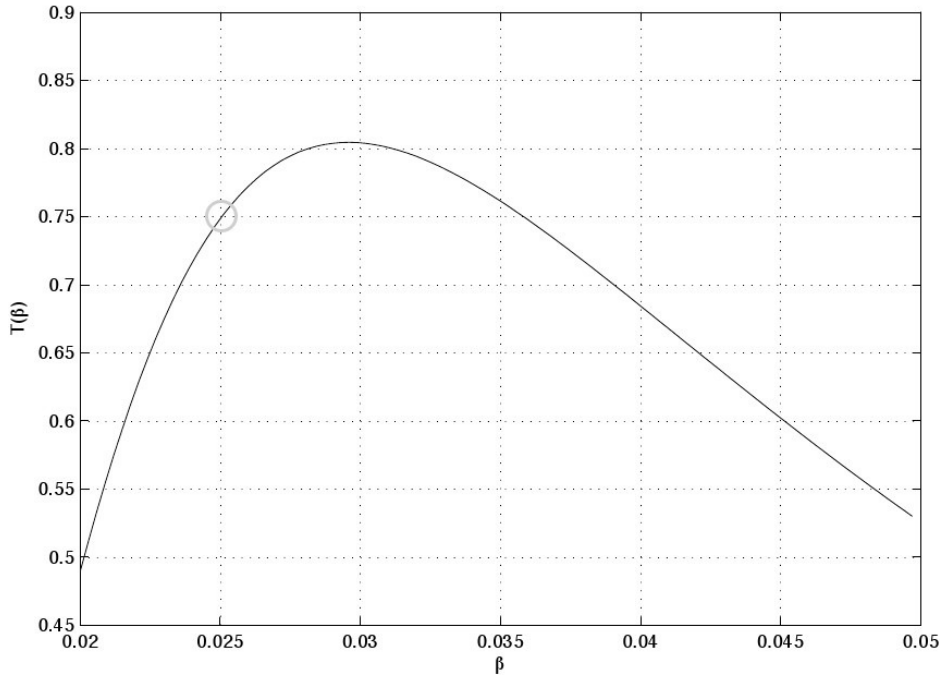

Figure 5.4: Time Transfer Factor (TTF) in the HIE-ISOLDE bunchers as a function of relativistic beam speed $\beta = v/c$. A beam energy of $300\,\mathrm{keV/u}$ *yields* $\beta = 0.025$ *which has been marked in the figure. The energy losses in the foils must be compensated for by pre-acceleration by a buncher, since acceleration after the foils has reduced efficiency.*

Table 5.2: Normalized emittances calculated from a set of particles after the RFQ and with angular straggling results from TRIM. Compare with Eq. 5.1 and Eq. 5.2.

Carbon foils

# foils	1	2	3	5	10	15	20
ε_x^* mm mrad	0.165	0.272	0.325	0.399	0.694	0.969	1.296
ε_y^* mm mrad	0.164	0.214	0.264	0.320	0.633	0.788	1.147

Polystyrene foils

# foils	1	2	3	5	10	15	20
ε_x^* mm mrad	0.120	0.182	0.208	0.301	0.447	0.575	0.796
ε_y^* mm mrad	0.113	0.155	0.176	0.242	0.343	0.492	0.748

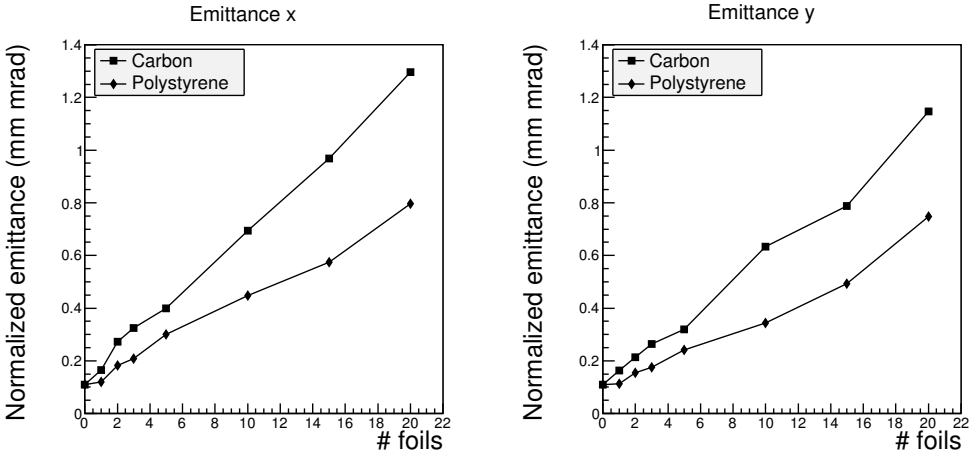

Figure 5.5: Normalized emittances from Tab. 5.2 as a function of the number of foils. The first data-points at zero foils is the emittance after the RFQ.

all elements then could perhaps not only give better beam transmission, but also allow installing more than 3 polarizing foils. In any case, the transverse emittance would only reduce the beam transmission through the linac, the greater issue at hand remains the energy loss which could completely cut the beam in the linac.

Table 5.3: Beam transmission and normalized emittances calculated at the end of the HIE-ISOLDE linac with 3 *PS foils simulated in the MEBT line. The* Nominal *configuration refers to a simulation without polarizing foils with acceleration and solenoid beam elements optimized for* $A/q = 4.5$*, but with the focusing quadrupole magnets in the low-energy section scaled to match* $A/q = 4$*.*

Configuration	5.716 MeV/u	11.241 MeV/u	Nominal
Transmission	86.9 %	86.0 %	100 %
ε_x^* mm mrad	0.177	0.141	0.085
ε_y^* mm mrad	0.149	0.161	0.083

Chapter 6

Summary

The first experimental evaluation of nuclear spin polarization with tilted foils has been performed at REX-ISOLDE. Coulomb excitation with particle scattering and β-NMR were used as polarization monitors. A degree of polarization of $P = 3.7(3)\%$ was measured with the β-NMR setup.

The angular distribution of scattered ^{21}Ne was measured with the Miniball γ-spectrometer and the T-REX barrel detector chamber. In order to tag the events, the γ-radiation following Coulomb excitation of the ^{21}Ne was recorded. The current results show a measured asymmetry that is consistent with zero asymmetry according to a statistical analysis, although better statistics may demonstrate an asymmetry of around one percent, depending on the beam energy.

This was the first Coulomb excitation experiment with the T-REX detector setup, so optimal settings were not known. Particle spectra with the two targets ^{60}Ni and ^{120}Sn target showed no clear structures expected from reaction kinematics, probably due to the strong energy spread in the reaction target affecting the recoiling ions. However, with the lower threshold of 6 MeV for the particle energy, a large quantity of detector noise and background events could be removed in the related γ-spectra. The length-wise coordinates in the resistive strips in the T-REX detectors could not be reconstructed due to saturated energy readouts, which reduced the efficiency of the Doppler correction and broadened the particle kinematics spectra. The latter required rather conservative gates for events. Total collected statistics were low due to the low cross-section of Coulomb excitation, even with the higher than normal beam current for the T-REX setup. Thus, the best way of improvement would be with more beam time or with higher detection efficiency. The beam energy was not ideal for the tilted-foils technique which, according to work by other groups, seems to be most effective at energies in the vicinity of 100 keV/u. However, this must be taken into consideration

together with the fact that the Coulomb excitation cross-section decreases rapidly with lower velocities.

Currently, the analysis cannot prevent a large amount of background events from being included in the calculation of the asymmetry value, due to the wide γ-energy and particle gates. This increases the signal-to-noise ratio for a reduced asymmetry value, but it does not destroy the value.

Before attempting a potential future scattering experiment, the above mentioned issues must be addressed. It would be interesting to look at an experiment designed specifically to evaluate the barrel detector response for medium or heavy nuclei from scattering reactions. Clear kinematics curves in the $E(\theta)$ plots and better strip length-wise position information would improve event selection, but also verify the data collected in the experiment. A thin target reduces the residue particle energy uncertainty, but also reduce the Coulomb excitation cross section. Finally, the beam interaction with the foil holder should be investigated to rule out systematic errors due to geometric changes in the setup when changing the foil tilting angle.

Next, the β-NMR experiment, designed and assembled specifically for this project, was performed with a 300 keV/u energy ^{8}Li beam. A clear NMR-signal of up to 0.99(8) % β-asymmetry was observed when using an energy-degrading Mylar foil and 10 DLC foils, equivalent to a degree of nuclear spin polarization of at least 3.7(3) %. This result and the accompanying statistical error bar was obtained in only 2 h, although more data were collected for a few other experimental configurations, which gave similar degrees of polarization. This result is comparable to previous experiments by other groups.

There is however still room for improvement and additional testing of the setup. Certain effects on the asymmetry are not yet well understood, such as the sensitivity to vertical beam trajectory deviation. Other compelling tests would be to vary the number of foils, foil tilting angle and testing several foil materials. Once the ^{8}Li case is well understood and reproducible, other isotopes or maybe even experiments outside polarization evaluation would be in place.

The promising results have spurred the planning for an experiment proposing to measure the magnetic moments of some neutron-rich odd-even indium isotopes with polarized nuclear spin and measured with the present β-NMR. Not only would this be the first time the magnetic moments of these isotopes are measured, but the many varying nuclear features of the isotopes may give further insight into the tilted-foils technique. Furthermore, in order to go beyond the β-NMR technique, post-acceleration of the beam to energies suitable for reaction experiments have been evaluated for the HIE-ISOLDE linac. Parts of the MEBT matching line between the low-energy and high-energy sections of the linac, which is an ideal location for the foils, is currently

under the design stage and the possibilities and constraints have been investigated, but is still a work in progress. The major issue is the energy loss in the foils which would make post-acceleration impossible. The emittance growth is also a problem, but it would only reduce the beam transmission.

The future of the tilted-foils technique at ISOLDE looks promising, with a proposed experiment to measure g-factors of indium isotopes that can be accomplished with an available setup, but also with work conducted to expand the beam-energy regime for other types of experiments.

Nomenclature

ADC Analog-to-Digital Converter, transforms an analog pulse to a digital value, typically by finding the peak of the analog signal.

DAQ Data AcQuisition.

DIP Dual In-line Package, a standard type of container for electronics components.

DLC Diamond-Like Carbon.

EPR Electron paramagnetic resonance, a technique for finding unpaired electrons in a sample in an external magnetic field and subject to an RF field.

FEBIAD Forced Electron Beam Induced Arc Discharge, a type of plasma-based ion source in use at ISOLDE.

FMR Ferromagnetic resonance, a technique for investigating the magnetization of a sample in an external magnetic field subject to an RF field.

HPGe High Purity Germanium.

ISOLDE Experimental facility at CERN capable of producing a wide range of radioactive isotopes in many energy domains.

Linac Linear accelerator.

MARaBOU MBS And ROOT Based Online/Offline Utility.

MBS Multi Branch System used for several experiments at ISOLDE.

MEBT Medium Energy Beam Transfer line, matching section from the RFQ to the subsequent beam accelerating elements.

Miniball γ-spectrometer after the REX-ISOLDE linac aimed at Coulomb excitation and transfer experiments.

NMR Nuclear Magnetic Resonance, a series of techniques which probe the interaction between particles and artificially created magnetic fields.

PSA Pulse-Shape Analysis.

REX-ISOLDE Radioactive beam EXperiment at ISOLDE, cooler, charge breeder and linac capable of delivering beams with $2.5 < A/q < 4.2$ and $0.3\,\mathrm{MeV/u} < E_{beam} < 3\,\mathrm{MeV/u}$.

RILIS Resonance Ionization Laser Ion Source, a type of laser-stimulated ion source in use at ISOLDE.

ROOT OO-oriented high performance data analysis framework developed at CERN aimed originally at particle and nuclear experiments.

SC CERN Synchro-Cyclotron, 600 MeV proton accelerator.

T-REX Particle detector setup for transfer experiments with Miniball.

TTF Time Transit Factor, describes the acceleration-efficiency in an accelerating gap due to the time-varying RF field: $\Delta W \propto T_{TTF}$.

Acknowledgments

I would like to express my gratitude to the following people who guided me through three years of physics at ISOLDE in a foreign country, and one final year at Chalmers, in approximately chronological order:

Mats Lindroos, for having brought to my attention the possibility of working as a Ph.D. at ISOLDE,

Thomas Nilsson, for recommending my application and supporting the idea of me going,

Fredrik Wenander, for introducing me to the project on a hot summer's day in his office, teaching me all the tricks of the technical trade, for showing what hard work really means, and for all the moral support,

Georgi Georgiev, for driving the project and for knowing so much,

Wolf-Dietrich Zeitz, for donating the β-NMR equipment and for his knowledge in the subject and physics in general,

Alexander Herlert and Yorick Blumenfeld, for helping out with the occasional physics or administative complication,

Christophe Sotty, for being a great companion Ph.D. at the experiments, his dedication and passion to his work, trying to keep me awake on late-night shifts, and his friendship,

Magnus Eriksson, for being so eager to assist in the ^{21}Ne experiment,

Jarno Van de Walle, for sharing his great knowledge in Coulomb excitation,

Janne Pakarinen, for even more Coulomb excitation experience,

Magdalena Kowalska, for the same reasons as for Fredrik, except for being more focused on nuclear physics rather than technical things,

Kathrin Wimmer, for all the help with the analysis of the T-REX detector setup,

Alexander Gottberg and Monika Stachura, for assisting in the chamber design and for floating thin foils onto their frames,

Yoshikazu Hirayama and Nobuaki Imai, for sharing their experience with tilted foils,

Miguel Luis Lozano Benito and the rest of the ISOLDE technical team,

for all the time they put into delivering good beams to the experiments,

Jan Diriken, Nigel Warr and Michael Seidlitz, for discussions regarding Miniball,

Andreas Heinz, for helping out with the assembly of the β-NMR and for consistently checking up on my progress on writing the thesis,

Håkan Johansson, for making the DAQ run like a well-oiled machine and his cheerful demeanor as he patrolled the offices,

Matthew Alexander Fraser, for his swift work on post-acceleration,

Alexandre Charpy and Jimmy Rotureau, for being great office mates,

my family (who should really come first chronologically...), for believing in my abilities and helping out when real life got tough,

my friends, for showing that other side to life that I always forget about,

and everybody else that I have crossed paths with.

Bibliography

[1] C Kittel. "On the Theory of Ferromagnetic Resonance Absorption". *Phys. Rev.* 73 (Jan. 1948), pp. 155–161.

[2] M Che and E Giamello. "Electron Paramagnetic Resonance". *Stud. Surf. Sci. Cat.* 57 (1990), B265–B332.

[3] A Abragam. *The Principles of Nuclear Magnetism*. Oxford University Press, USA, 1996.

[4] K S Krane. *Introductory Nuclear Physics*. 3rd. Wiley, 1987.

[5] H J Andrä. "Zero-field quantum beats subsequent to beam-foil excitation". *Phys. Rev. Lett.* 25 (Aug. 1970), pp. 325–327.

[6] H Kopfermann. *Nuclear Moments*. Academic Press Inc., 1958.

[7] T R Carver. "Optical Pumping". *Sci.* 141 (Aug. 1963), pp. 599–608.

[8] C D P Levy et al. "Polarized Radioactive Beam at ISAC". *Nucl. Instr. Meth. Phys. Res. B* 204 (2003), pp. 689–693.

[9] M Keim et al. "Measurement of the electric quadrupole moments of $^{26-29}$Na". *Eur. Phys. J. A* 8 (2000), pp. 31–40.

[10] M Kowalska. "Ground state properties of neutron-rich Mg isotopes - the "island of inversion" studied with laser and β-NMR spectroscopy". PhD thesis. der Johannes Gutenberg-Universität Mainz, Fachbereich Physik, Mathematik und Informatik, 2006.

[11] M Kowalska. "Nuclear ground-state spins and magnetic moments of ^{27}Mg, ^{29}Mg, and ^{31}Mg". *Phys. Rev. C* 77 (2008), p. 034307.

[12] J Murata et al. "Test of Time Reversal Symmetry using Polarized 8Li at TRIUMF-ISAC". *J. Phys. Conf. Ser.* 312 (2011), p. 102011.

[13] W D Brewer. "Recent developments in low-temperature nuclear orientation". *Rep. Prog. Phys.* 53 (Dec. 1990), pp. 483–548.

[14] C S Wu. "Experimental Test of Parity Convesrvation in Beta Decay". *Phys. Rev.* 105 (1957), pp. 1413–1415.

[15] T D Lee and C N Yang. "Question of Parity Convervation in Weak Interactions". *Phys. Rev.* 104 (Oct. 1956), pp. 254–258.

[16] R Eder et al. "NICOLE: New On-Line Orientation Facility at ISOLDE/CERN". *Hyp. Int.* 60 (1990), pp. 83–90.

[17] J Rikovska and N J Stone. "Beta-NMR/ON on-line at the ISOLDE facility, ISOLDE - recent magnetic moment studies near double magic ^{68}Ni". *Hyp. Int.* 129 (2000), pp. 131–140.

[18] H Okuno et al. "Polarization in projectile fragmentation and g-factor measurements for neutron-rich nuclei". *Hyp. Int.* 78 (1993), pp. 97–103.

[19] K Asahi et al. "New aspect of intermediate energy heavy ion reactions. Large spin polarization of fragments". *Phys. Lett. B* 251 (Nov. 1990), pp. 488–492.

[20] H G Berry and M Hass. "Beam-foil spectroscopy". *Ann. Rev. Nucl. Part. Sci.* 32 (1982), pp. 1–34.

[21] U Fano and J H Macek. "Impact Excitation and Polarization of the Emitted light". *Rev. Mod. Phys.* 45 (Oct. 1973), pp. 553–573.

[22] D G Ellis. "Density-operator description of foil-excited atomic beams: Zero-field quantum beats in L-S coupling without cascades". *Opt. Soc. Am.* 63 (1973), pp. 1232–1235.

[23] H J Andrä et al. "Electronic Interaction of Fast Ions with Surfaces". *Nucl. Inst. Meth. Phys. Res. B* 9 (1985), pp. 572–585.

[24] H Winter and H J Andrä. "Hyperfine Interaction Using Grazing Beams". *Hyp. Int.* 24-26 (1985), pp. 277–299.

[25] H Schröder and E Kupfer. "Model for the Production of Circular Polarization via Beam-Foil Interaction". *Z. Phys. A* 279 (1976), pp. 13–16.

[26] J Burgdörfer, H Gabriel, and H Schröder. "Theory of Optical Polarization Due to Electron Capture from Localized Target States by Fast Ions". *Z. Phys. A* 295 (1980), pp. 7–16.

[27] S Momota et al. "Mechanism of Polarization Production by Means of the Tilted-Foil Technique Studied Using Beta-Radioactive Nuclei". *Hyp. Int.* 142 (2002), pp. 513–548.

[28] G Goldring and Y Niv. "Nuclear Polarization Generated in Multi Tilted-Foil Arrays". *Hyp. Int.* 21 (1985), pp. 209–218.

[29] H G Berry et al. "Orientation and Alignment of Atoms by Beam Foil Interaction". *Phys. Lett. A* 50 (Nov. 1974), pp. 59–60.

[30] J Bendahán et al. “Heavy Ion Beam Polarization Produced by the Multi-Tilted-Foil Interaction”. *Z. Phys. A* 331 (1988), pp. 343–346.

[31] E Matthias et al. “Theory of Nuclear Magnetic Resonance Detected by Nuclear Radiations”. *Phys. Rev. A* 4 (Oct. 1971), pp. 1626–1658.

[32] L M Chirovski et al. “Directional Distributions of Beta-Rays Emitted from Polarized 60Co Nuclei”. *Phys. Lett.* 94B (July 1980), pp. 127–130.

[33] K Alder and A Winther. *Electromagnetic Excitation - Theory of Coulomb Excitation with Heavy Ions*. North Holland Publishing company, 1975.

[34] D Cline et al. *GOSIA User Manual for Simulation and Analysis of Coulomb Excitation Experiments*. May 2012. URL: `http://www.pas.rochester.edu/~cline/Gosia/Gosia%5C_Manual%5C_20120510.pdf`.

[35] M Simonius. “Theory of polarization measurements. Observables, amplitudes and summetries”. *Lect. Not. Phys.* 30 (1974), pp. 38–87.

[36] P Zupranski et al. “Polarization Monitors for Polarized Heavy Ion Beams”. *Nucl. Instr. Meth.* 167 (1979), pp. 193–200.

[37] E Kugler. “The ISOLDE facility”. *Hyp. Int.* 129 (2000), pp. 23–42.

[38] *The ISOLDE factility*. Mar. 2013. URL: `http://isolde.web.cern.ch/`.

[39] P Van Duppen and K Riisager. “Physics with REX-ISOLDE: from experiment to facility”. *Jour. Phys. G* 38 (Jan. 2011), p. 024005.

[40] M Georges. *TE-EPC-LPC in LHC*. 2013. URL: `http://te-epc-lpc.web.cern.ch/te-epc-lpc/machines/lhc/general.stm`.

[41] T Bjørnstad et al. “Methods for Production of Intense Beams of Unstable Nuclei: New Developments at ISOLDE”. *Phys. Scr.* 34 (July 1986), pp. 578–590.

[42] L Penescu et al. “Arc Discharge Ion Source Development at CERN ISOLDE”. *U.P.B. Sci. Bull. A* 72 (2010).

[43] L Penescu et al. “Numerical Simulations of Space Charge Effects and Plasma Dynamics for FEBIAD Ion Sources”. *Nucl. Instr. Meth. Phys. Res. B* 266 (2008), pp. 4415–4419.

[44] F Wenander. “Charge Breeding of Radioactive Ions With EBIS and EBIT”. *J. Instr.* 5 (Oct. 2010), p. C10004.

[45] F Ames et al. “Cooling of radioactive ions with the Penning trap REX-TRAP”. *Nucl. Inst. Meth. Phys. Res. A* 538 (2005), pp. 17–32.

[46] D Habs et al. “The REX-ISOLDE project”. *Hyp. Int.* 129(1-4) (2000), pp. 43–66.

[47] N Warr et al. "The Miniball spectrometer". *Eur. Phys. J. A* 49 (2013), p. 40.

[48] *Access to the Yield information*. Apr. 2013. URL: https://oraweb.cern.ch/pls/isolde/query_tgt.

[49] *Chart of Nuclides*. Apr. 2013. URL: http://www.nndc.bnl.gov/chart/chartNuc.jsp.

[50] M Eriksson. *Installation of Mobile Tilted Foils Holder at REX-ISOLDE*. Tech. rep. CERN-BE-Note-2010-004. Geneva: CERN, Jan. 2010.

[51] T Kröll et al. "Analysis of Simulated and Measured Pulse Shapes of Closed-Ended HPGe detectors". *Nucl. Instr. Meth. Phys. A* 371 (Mar. 1996), pp. 489–496.

[52] K Wimmer et al. *Study of the onset of deformation and shape coexistence in ^{46}Ar via the inverse kinematics (t,p) reaction*. Tech. rep. CERN-INTC-2009-034.INTC-P-270. Geneva: CERN, Oct. 2009.

[53] K Wimmer. "Discovery of the shape coexisting 0^+ state in ^{32}Mg". PhD thesis. Technische Universität München, Physik-Department E12, 2010.

[54] *XIA DGF-4C*. Apr. 2013. URL: http://xia.com/DGF-4C_Download.html.

[55] N Warr and M Seidlitz. personal communication. 2010.

[56] *MARaBOU*. Mar. 2013. URL: http://www.bl.physik.uni-muenchen.de/marabou/htmldoc/.

[57] *Welcome to MBS*. Oct. 2010. URL: http://www-win.gsi.de/daq/.

[58] *Miniball electronics at May 2009*. May 2009. URL: http://www.ikp.uni-koeln.de/~warr/doc/electronics%5C_May2009.pdf.

[59] O B Tarasov and D Bazin. "LISE++: Radioactive Beam Production with In-Flight Separators". *Nucl. Instr. Meth. Phys. Res. B* 19-20 (Oct. 2008), pp. 4657–4664.

[60] H Ower. PhD thesis. Universität Frankfurt, 1980.

[61] Y Hirayama et al. "Tilted-foil technique for producing a spin-polarized radioactive isotope beam". *Eur. Phys. J. A* 48 (2012), pp. 54–63.

[62] M Toulemonde. "Irradiation by Swift Heavy Ions: Influence of the Non-Equilibrium Projectile Charge State for Near Surface Experiments". *Nucl. Instr. Meth. Phys. Res. B* 150 (2006), pp. 263–268.

[63] P Raghavan. "Table of Nuclear Moments". *At. Dat. Nucl. Dat. Tab.* 42 (1989), pp. 189–291.

[64] *VULOM4b*. Apr. 2013. URL: https://www.gsi.de/work/organisation/wissenschaftlich_technologische_abteilungen/experiment_elektronik/digitalelektronik/digitalelektronik/module/vme/vulom/vulom4b.htm.

[65] H T Johansson et al. *TRLO II - flexible FPGA trigger control*. Tech. rep. PHN-IS-EE-03. GSI, 2010, p. 231.

[66] T L Shaw and N J Stone. "Nuclear Spin-Lattice Relaxation Attenuation Coefficients for Use in On-Line Nuclear Orientation Experiments". *At. Dat. Nucl. Dat. Tabl.* 42 (1989), pp. 339–363.

[67] O Ofer et al. "Beta-NMR study of isolated 8Li+ in the enhanced paramgnet platinum". *Phys. Rev. B* 86 (2012), p. 064419.

[68] G Georgiev et al. *Nuclear moment studies in the odd-mass In isotopes up to N=82 using the Tilted Foils technique*. Tech. rep. CERN-INTC-2012-059.INTC-P-360. Geneva: CERN, Oct. 2012.

[69] J Eberz et al. "Spins, Moments and Mean Square Charge radii of 104-127In Determined by Laser Spectroscopy". *Nucl. Phys. A* 464 (Mar. 1987), pp. 9–28.

[70] *Status of the HIE-ISOLDE Project at CERN*. Proceedings of HIAT. Chicago, IL, USA, 2012.

[71] M A Fraser et al. "Design Study for 10 MHz Beam Frequency of Post-Accelerated RIBs at HIE-ISOLDE". *IPAC 2013 Conference Edition*. (Shanghai, China). Ed. by Z Dai and C Petit-Jean-Genaz. APS, June 2013, pp. 3933–3935. ISBN: 978-3-95450-122-9.

[72] E G Myers et al. "Transport of Polarized Ions Through a Tandem-Superconducting-Linac Heavy-Ion Accelerator". *Nucl. Instr. Meth. Phys. Res. A* 334 (1993), pp. 271–282.

[73] V Kumar. "Understanding the Forcusing of Charged Particle Beams in a Solenoid Magnetic Field". *Am. J. Phys.* 77 (2009), pp. 737–741.

[74] J F Ziegler. "SRIM-2003". *Nucl. Instr. Meth. Phys. Res. B* 219-220 (2004), pp. 1027–1036.